

The microstructural investigation of continuous-wave laser irradiated silicon rich silicon oxide

Dissertation

zur Erlangung des mathematisch-naturwissenschaftlichen

Doktorgrades

”Doctor rerum naturalium”

der Georg-August-Universität Göttingen

-

im Promotionsprogramm PROPHYS

der Georg-August-University School of Science (GAUSS)

vorgelegt von

Nan Wang

aus der Volksrepublik China

Göttingen, 2017

Mitglieder des Betreuungsausschusses:

Prof. Dr. Michael Seibt	IV. Physikalisches Institut, Georg-August-Universität Göttingen
Prof. Dr. Cynthia A. Volkert	Institut für Materialphysik, Georg-August-Universität Göttingen

Mitglieder der Prüfungskommission:

Referent:	Prof. Dr. Michael Seibt IV. Physikalisches Institut, Georg-August-Universität Göttingen
Korreferent:	Prof. Dr. Cynthia A. Volkert Institut für Materialphysik, Georg-August-Universität Göttingen

Weitere Mitglieder der Prüfungskommission:

Prof. Dr. Konrad Samwer	I. Physikalisches Institut, Georg-August-Universität Göttingen
Prof. Dr. Reiner Kirchheim	Institut für Materialphysik, Georg-August-Universität Göttingen
Prof. Dr. Angela Rizzi	IV. Physikalisches Institut, Georg-August-Universität Göttingen
Dr. Jürgen Ihlemann	Laser-Laboratorium Göttingen e.V.

Tag der mündlichen Prüfung: 19.12.2017

Contents

1	Introduction	1
1.1	Scientific background	1
1.1.1	Direct/indirect bandgap	1
1.1.2	Quantum confinement and other luminescence mechanisms	3
1.1.3	Silicon rich silicon oxide	6
1.1.4	Light solid interactions	10
1.1.5	Characterization methods overview	12
1.2	The main development in micro-structure investigation	16
1.2.1	Thermally annealed SRSO	16
1.2.2	Laser annealed SRSO	20
1.3	The contribution of our work in micro-structure investigation . . .	24
1.3.1	Damage-free laser irradiation and spatially controlled microstructure	25
1.3.2	The formation of porous region	25
1.3.3	The nanoscopic phase separation	26
2	Generation of silicon nanocrystals by damage free CW laser annealing of substrate-bound SiO_x films	27
2.1	Introduction	28
2.2	Experimental	29
2.3	Results	30
2.4	Discussion	36
2.5	Conclusion	41
2.6	Acknowledgements	41
3	Microstructural analysis of the modifications in substrate-bound silicon-rich silicon oxide induced by continuous wave laser irradiation	43
3.1	Introduction	44
3.2	Materials system and Experimental	45

3.3	Results and Discussion	46
3.3.1	Damage-Free CW Laser Irradiation	46
3.3.2	Surface Topography and Layer Thickness	46
3.3.3	Microstructure of Damaged Region	49
3.4	Summary and Conclusion	50
3.5	Acknowledgment	51
4	Formation of porous silicon oxide from substrate-bound silicon rich silicon oxide layers by continuous-wave laser irradiation	55
4.1	Introduction	56
4.2	Experiment	57
4.3	Results	58
4.3.1	Structural properties of the porous silicon oxide	59
4.3.2	Chemical composition of porous silicon oxide	62
4.3.3	Quantitative EDX study on porous part	62
4.4	Discussion	64
4.5	Conclusion and Outlook	66
5	The nanoscopic Si–SiO₂ phase separation in silicon rich silicon oxide by continuous wave laser annealing: a quantitative approach	73
5.1	Introduction	74
5.2	Experimental details	76
5.3	The description of model and simulation	79
5.4	Results	81
5.4.1	HRTEM investigation for nc-Si particle and its surrounding materials	81
5.4.2	EELS spectrum imaging of nc-Si particles and their amorphous matrix	82
5.4.3	HCDF and particle analysis	84
5.4.4	The comparison between EDX experiment and simulation	87
5.5	Discussion	89
5.6	Conclusion and Outlook	90
6	General discussion and Summary	93
	Bibliography	96
	Curriculum Vitae	117

Own publications	119
Author Contributions	121
Acknowledgements	123

1 Introduction

1.1 Scientific background

1.1.1 Direct/indirect bandgap

Light emitting diodes (LED) usually employ direct band-gap III–V semiconductors (ie. GaAs) coupled on silicon substrate. However, the lattice mismatch, the difference in thermal expansion between GaAs and Si stimulates Si diffusion into the upper layer as impurities, which lowers the efficiency of LED devices. To overcome this problem, several methods like superlattice structure design and buffer layer injection have been employed. Actually, all these additional industrial arts increase the cost of manufacture processing. Thus, to avoid the heterogeneity of materials systems mentioned above, silicon based materials instead of GaAs can be a good choice. Unfortunately, unlike GaAs, light emission can not be obtained in bulk crystalline silicon at room temperature due to its extremely low internal quantum efficiency (IQE), where IQE is defined as the ratio of the number of collected photons to the number of electron-hole pairs excited by incident photons or an applied electric field. The strong contrast in IQE between GaAs and Si stems from their different energy band structures. Band structures describe energy of an electron as a function of its momentum in solids. And band structures rely on a number of factors like crystal structure, bond–bond dissociation energy and chemical composition. Thus, direct experimental measurement of band structure is mainly through angle-resolved photoemission spectroscopy and actually it can be calculated empirically. For instance, based on pseudopotential method [1], the band structures of Si (a) and GaAs (b) in the first Brillouin zone is presented in Fig. 1.1, respectively. The valence band structure of Si and GaAs is similar and in general there is a maximum energy value at the Brillouin zone center(ie. $k=0$): in silicon it appears at Γ point in the band Γ_{25} in Fig. 1.1 (a); small difference in

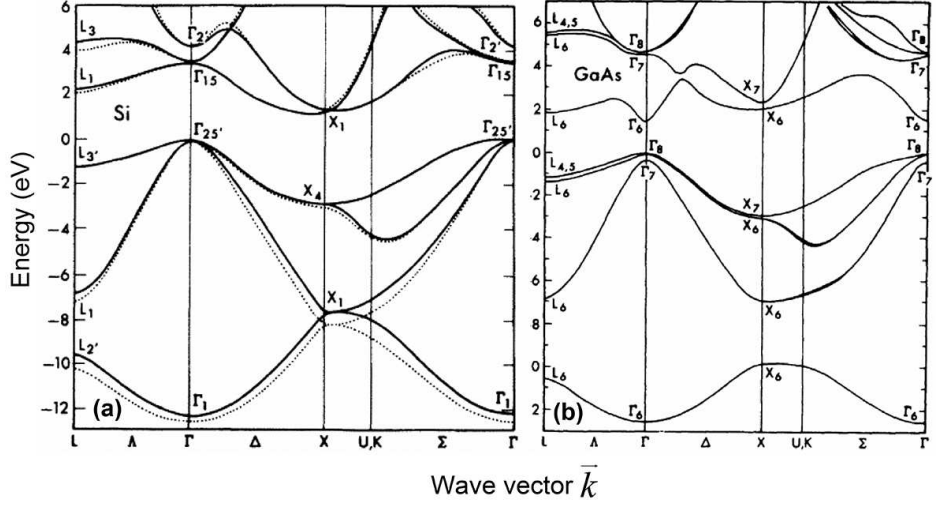


Figure 1.1: Energy band structures of Si(a) and GaAs(b) calculated based on one pseudopotential method [1]. Here we can see in Si (a) the top of valence band in Si is at Γ point while the bottom of conduction band is close to X point. Thus, optical transitions of electron through band-gap needs the third particle due to momentum conservation. In GaAs (b) both the top of valence band and the bottom of conduction band locate at Γ point, where optical transitions are direct.

GaAs is that Γ_{25} is degenerated into two sub-bands Γ_7 and Γ_8 due to the spin-orbit interaction. The minimum energy value in conduction band of GaAs is at Γ point in the band Γ_6 , and it is defined as direct band gap semiconductor. While in Si there is a shift of momentum close to X point (not Γ point) for the minimum value, and it is defined as indirect band gap semiconductor. Optical transitions in semiconductors follow both energy and momentum conservation. In a direct semiconductor, radiative electron hole recombination easily occurs. The electron in the conduction band state drops into the valence band state spontaneously. In the meanwhile, a photon with energy that equals to the band gap is generated. However, in an indirect semiconductor, radiative recombination needs the further process (the assistance of the third particle like phonon) based on momentum conservation. Part of the electron momentum that equals to the momentum deviation of X and Γ point is transferred to the phonon and after that the recombination occurs. This kind of three body interaction in Si is very inefficient in contrast to the direct transition in GaAs [2][3] and this is the dominated reason that the IQE of Si is much lower than that of the latter one.

1.1.2 Quantum confinement and other luminescence mechanisms

In order to improve the low IQE in silicon light emission, a lot of significant efforts have been undertaken. The tendency of these efforts is construction of low dimensional silicon structures to increase the overlap of wave function of electron and hole. The room temperature luminescence in low dimensional silicon system was firstly detected in porous silicon [4][5] by L. T. Canham in 1990. In this work, electrochemical etching process is employed to generate cavities in Si wafer in variety of reaction time and visible luminescence spectrum from silicon immersed in hydrofluoric acid (HF) in 1h, 2h and 6h are displayed in Fig. 1.2. The size of cavity depends on many parameters. For example, the longer the reaction time the smaller the scale of the rest low dimensional Si structures. The blue shift can be observed when the size of porous silicon structures is reduced. Similar results on luminescence in porous silicon are also reported by other researchers [6, 7]. To understand this visible luminescence and the blue shift phenomenon, the concept of quantum confinement (QC) is introduced. The word confinement means that the electron is confined in a real space whose size is comparable with the free exciton Bohr radius (the distance in an electron-hole pair, 4.3 nm in bulk silicon [8]) in semiconductor. According to Heisenberg's uncertainty principle, if a particle is confined in a box (its position is determined more precisely), its momentum is determined less precisely. Consideration of the carriers (electron and hole) in Si, if a carrier is confined in a low dimensional Si structure, its wave-function in the momentum space is extended. Once the wave-function of electron in conduction band overlaps with the wave-function of hole in valence band, direct optical transitions occur. Thus, the luminescence in low dimensional silicon system can be observed. Quantum, the other word in QC, leads to the energy levels discrete and widens the band gap of semiconductors [9, 10]. Consequently, the blue shift of luminescence can be observed when the size of low dimensional nanostructures is reduced. It should be noted that the intensive contrast in PL intensity presented in Fig. 1.2 can not be simply explained by QC and this can be the main driving force for researchers to explore other potential light emission mechanisms. And it should be noticed that the QC model avoid to involve in specific radiative recombination center for luminescence emission, which attract researchers' focus on PL mechanism exploration. As an example, for PS after the QC model, the other 5 proposed models [11] are listed as follows: hydrogenated amorphous silicon (a-Si:H) model, surface hydrides model (SiH_x), defect model [12][13], siloxene model

[14] and surface states model [15].

Except for PS, RT PL can also be observed in other low dimensional silicon structures like Si/SiO₂ superlattices, silicon nanocrystals, silicon quantum wells, wires and dots. In contrast to PS, these structures perform thermal stability and show great potentials in applications. For example, controllable Si/SiO₂ superlattices, which enjoy uniform Si structures, perform RT PL according to literature [16]. The wavelength of emitted light can be tuned by Si layer thickness according to the QC. Actually, it is quite interesting that the PL spectra in Si/SiO₂ superlattices can be separated into two categories based on experimental and theoretical studies: a).there is a PL peak at 1.65 eV and its position is almost independent of Si layer thickness, but the intensity of this peak increase with decreasing Si layer thickness [17][18]; b).the shift of PL peak position depends on the thickness of Si layer [16][19]. The spectra of type b can be explained by QC while the spectra of type a stems from oxygen defect recombination centers at the Si/SiO₂ interface. Thus, the optical properties of Si/SiO₂ superlattice depend not only on the Si layer thickness, but also on the properties of Si/SiO₂ interface. Actually, the fabrication of Si/SiO₂ superlattice usually requires molecular beam epitaxy to accurately control the size of structures, and it may be not economical.

Another interesting approach to obtain RT PL in Si/SiO₂ system is Si nanocrystals (nc-Si) embedded in SiO₂ and its production is economical and practical. In this material system, photon-generated carriers only exist in Si nanocrystals due to the large band gap of SRSO/SiO₂ (8 eV for SiO₂; the band gap of SRSO depends sensitively on the content of oxygen, but it is still out of range for PL excited energy) although SiO₂ has a direct band gap. However, the radiative recombination centers of these carriers for light emission are still on the debate.

In general, the origin of light emission can be separated into three types: (a) the usual QC effect; (b) defects in nanocrystals; (c) the interfacial region between Si and SiO₂. Details in these mechanisms are discussed as follows.

Similar to PS materials, the direct evidence of QC effect is that PL peak energy depends on the size of nc-Si particle. And it has been investigated by several researchers theoretically and experimentally. The dependence of PL peak energy with the diameter of nc-Si particles from some of previous experimental data [20, 21, 22, 23] is plotted in Fig. 1.3. Theoretical studies on this relation have employed

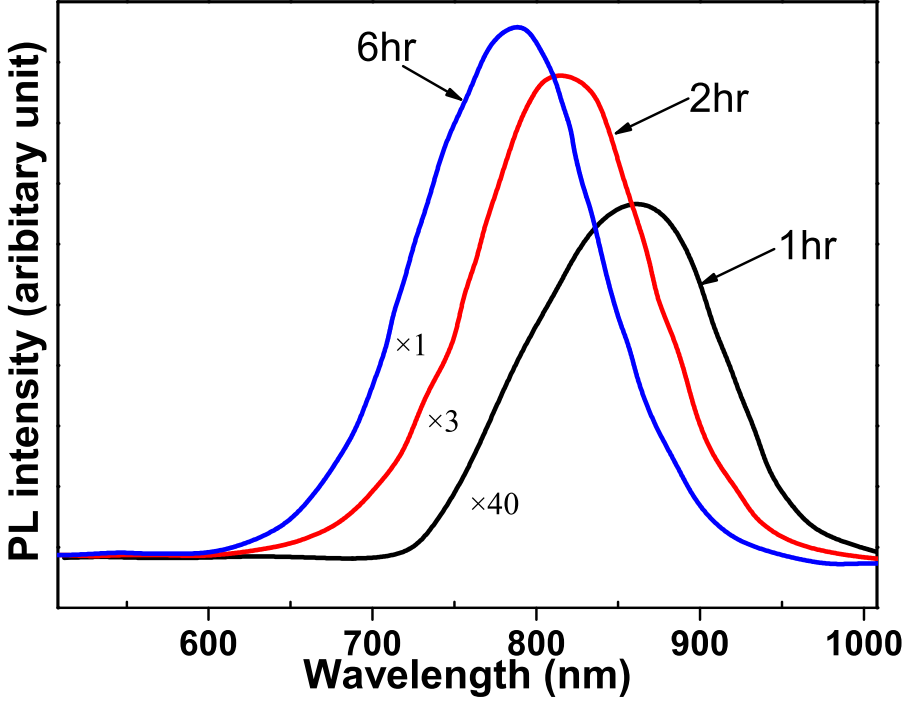


Figure 1.2: Room temperature photoluminescence(PL) spectrum in porous silicon fabricated by electrochemical etching process in 1h, 2h and 6h. When reaction time increases, the blue shift of spectra can be observed and the PL integrated intensity is reduced sharply. This data is reproduced from the results [4] by L. T. Canham.

the effective mass approximation [24], the third nearest-neighbor tight binding [9], the pseudopotential method [25] to calculate the emission energy. Here the PL peak energy that follows a $d^{-1.39}$ law [9] calculated by from C. Delerue et al., where d is the diameter of nc-Si particle, is also plotted in Fig. 1.3. Both experimental and theoretical results show the tendency of blue shift with reducing diameter. Quantitative agreement between them is still an open question and further theoretical investigations are needed.

However, the QC effect show difficulties in understanding the difference of PL intensity in some research reports [26][27]. The efficiency of PL yield is very sensitive to the surface states of nc-Si particle which works as the non-radiative recombination centers to quench PL. It has been reported that this can be improved by O or

H passivation. In addition, QC effect can not explain the strong PL [27] from a-Si cluster generated from SRSO sample and the highly luminescent a-Si is proposed to have spatial carrier confinement effect [28, 29].

Defect-related PL mechanism has been investigated by several groups [30, 31, 32, 33] and it is still arguable till now. The radiative recombination centers at the interfacial region between Si and SiO₂ [34, 35, 36, 37] is another interesting approach to understand PL emission. In essence, these two mechanism stem from the experimental observation on the second PL peak at low energy scale except for the PL peak at high energy dominated by QC effect. The shape and position of the second peak keep unchanged and only the intensity depends on external treatment like annealing or passivation. Although a lot of significant efforts have been underwent to understand the light emission mechanism, a model explaining all the luminescent properties in such material system is still lacking because the luminescence sensitively depends on the structure. This indicates the importance of finding the correlation between the optical properties and structural properties.

1.1.3 Silicon rich silicon oxide

The main strategy of obtaining nc-Si particle can be separated into two types: a) the growth of nc-Si from gas phase; b) the formation of nc-Si from an amorphous matrix [8][2]. Recently nc-Si particles precipitated in silicon rich silicon oxide (SiO_x, 0<x<2), which also performs RT PL, have drawn researchers' more attention. In this section, we will give a short review on structures and properties of this precursor. Silicon rich silicon oxide (SRSO), which is sub-stoichiometric silica, has supersaturated Si in solid solution. The investigations on the structure and properties of SRSO have been reviewed by N. Tomozeiu [38]. Early studies on SRSO structure is based on continuous random network models [39, 40, 41, 42, 43, 44, 45] which widely applied to amorphous Si and SiO₂, a modified random network model called Si—(Si_{4-x}O_x) tetrahedral configuration [46] is introduced to be corresponding to the chemical composition of SRSO. However, the structure based on this network model is not thermodynamically stable, and it is proposed to have a disproportionation of a-Si and SiO₂-like clusters [47].

In experiment, TEM investigation and atom probe tomography have provided ev-

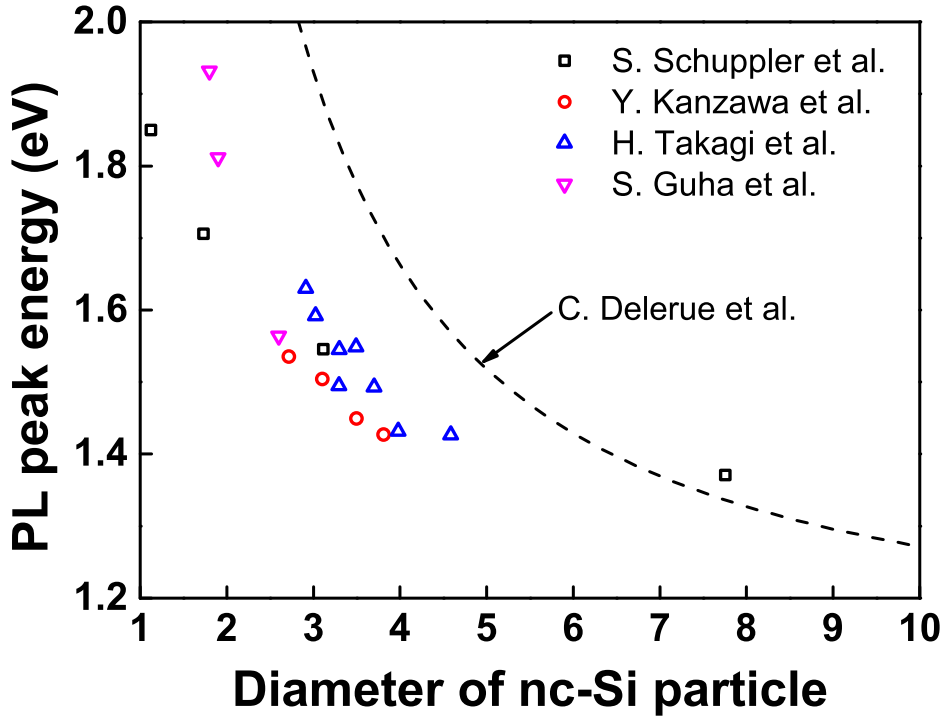


Figure 1.3: The dependence of PL peak energy with the size of nc-Si particle from several experimental results [20, 21, 22, 23] and theoretical calculations [9]. The blue shift with reducing size is clear seen. The discrepancy between experiment and theory is still unsolved.

idence of a-Si clusters in SRSO [48][49]. In a recent study, an advanced nanobeam electron diffraction called Angstrom-beam electron diffraction [50, 51, 52] with much finer spatial resolution presents the atomic-scale disproportionation in SRSO [53]. All these significant efforts have shown that the SRSO can not regarded as a simple mixture of Si and SiO₂, alternatively, there is a interfacial mixture between them. Actually, it should be noted that structure of amorphous solids is quite sensitive to preparation methods and it is also related to the history of formation. Thus, this long standing problem in amorphous solids need to be explored in future.

Similar to properties of all solids, the optical properties of SRSO are usually characterized by parameters like refractive index, absorption index and band gap, where we will not undergo much details. The refractive index decreases and the band

gap increases when the oxygen content in SRSO rises [54]. The dependence of the band gap with the absorption coefficient in amorphous semiconductor is usually described by the Tauc formula [55] and the Cody formula [56]. However, the definition of these two models neglects the reflectivity in amorphous semiconductors. After that, a well developed model called OJL model [57] has been introduced to describe the variation of density of state with optical properties in a much closer way.

Similar to amorphous semiconductors like a-Si or a-Ge, the electrical properties of SRSO at low temperature can be explained by the variable range hopping model (VRH) [58, 59]. Thanks to van Hapert and the systematic investigation [60] on the electronic transport mechanism of SRSO can be found in his PhD thesis. It is interesting that the current-voltage curves in SRSO show a non-Ohmic behavior and the electrical properties depend on the oxygen content of SRSO. For example, the high conductivity accompanies with the low oxygen content. These features can be explained by the carrier's path to the dangling bonds [38]. Once one electron enters into the dangling bonds, it has no contribution to the electrical current. In addition, the dangling bonds can be also employed to understand dielectric relaxation in SRSO, and it has been shown that SRSO materials have a great potential to be anodes for Li-ion batteries [61, 62, 63, 64, 48].

The investigation of the optical and electrical properties of SRSO is shortly reviewed below. It is well known that these properties in crystalline solids are mainly determined by energy band structure. In amorphous solids, band structures can not be calculated since the loss of periodic lattices. However, they can be described by a density of states, which also can be employed to explain these properties. For instance, in amorphous semiconductors, conduction band is replaced by lowest unoccupied molecular orbital (LUMO) and highest occupied molecular orbital (HOMO) equals to valence band. Based on the Mott-Davis model [65], except for the delocalized/extended states which also exist in crystalline semiconductors, there are localized states in amorphous semiconductors as shown in Fig. 1.4. Due to the loss of periodic lattice, the wave function of carrier is not the type of Bloch wave but extends in the whole wave vector space, which are the delocalized states ($E > E_c$ and $E < E_v$). Two type of localized states exist in amorphous semiconductors. Firstly, in Fig. 1.4 we can see that the edge of conduction/valence band does not end at E_c . Instead, it performs an exponential decrease to band gap, which are called as tail states. These tail states stem from deviations of bond length

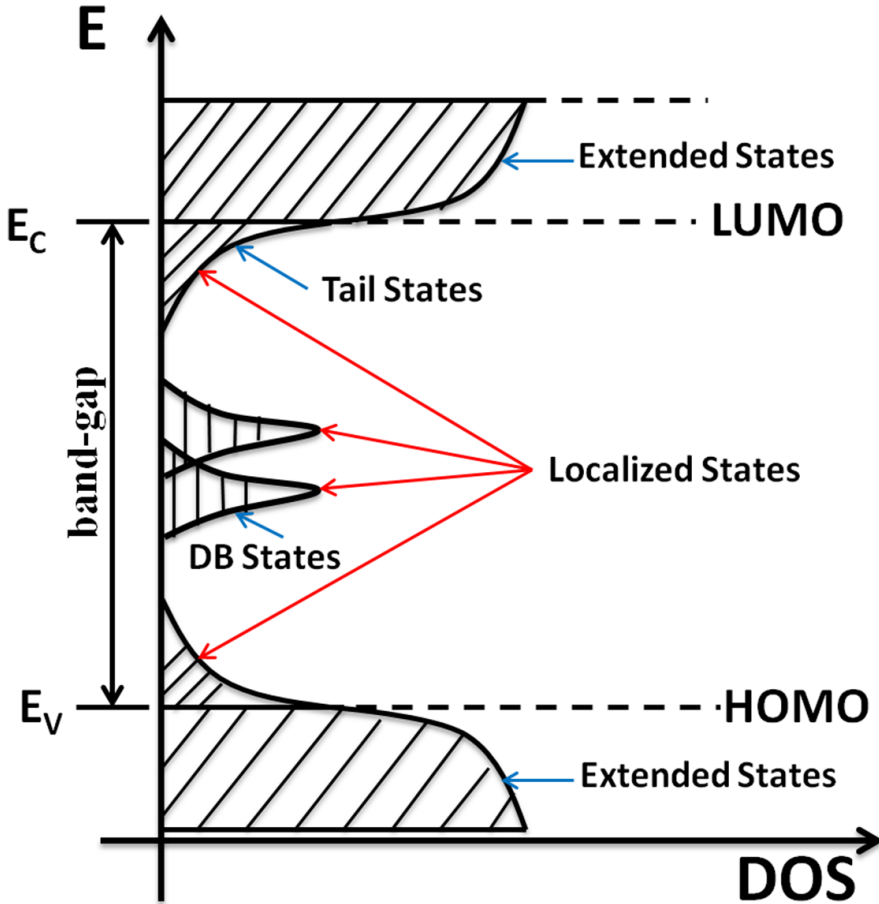


Figure 1.4: Mott-Davis model for density of states (DOS) in disordered materials [65]. Instead of conduction band and valence band in crystalline semiconductors, the lowest unoccupied molecular orbital (LUMO) and the highest occupied molecular orbital (HOMO) are introduced to describe the behavior of carriers in disordered semiconductors. The states can be separated into two types: the extended/delocalized states and the localized states. The localized states include the tail states due to the deviation of bond length and bond angle with that in crystalline lattice and the dangling bond (DB) states due to the integrity of covalent bond. The edge of tail states decrease exponentially into the band gap and the DB states locate near the mid gap.

and bond angle in the near neighboring atom coordination. Secondly, defects like dangling bonds (DB) induced in synthesis process of amorphous materials form

the localized DB states near the mid band gap. Electrons can be trapped by DB and the reducing density of DB states can be achieved by passivation of hydrogen or oxygen.

1.1.4 Light solid interactions

The Si nanocrystals precipitation from SRSO samples can be achieved by several methods like furnace annealing and laser annealing (LA). In contrast to furnace annealing, heat flow on samples through LA can be controlled temporally and spatially to form new features. In this section, we will introduce some basic knowledge of LA (light solid interaction) especially in heating amorphous semiconductors.

The motivation of LA employment is to change properties of disordered semiconductors. The deposition of disordered solids occurs under non-equilibrium condition, which means that atomic configuration does not achieve the equilibrium position that corresponds to the minimum value of total free energy. These unbalanced configurations can be moved to another position by a subsequent thermal process with proper temperature and time, which drastically changes properties of solids. The LA with controllable irradiation time may provide a good way to investigate the kinetics of configurations to solve several controversial problems in materials science like the process of crystallization and nano-particles growth.

Light solid interactions depend on a number of factors. For solids, optical properties like absorption, transmission and reflection are significant to estimate the utilization rate of laser light. Except for irradiation time, laser intensity and wavelength are another two important factors in understanding light solid interactions. One typical example of the influence of laser intensity and irradiation time is the Staebler–Wronski effect [66, 67] (SWE) that widely exists in a-Si and the authors found that an apparent decrease in both photo- and dark-conductivity when a-Si is irradiated for long time. The reason of this effect is still on debate and a simplified way to understand it is that metastable defects like dangling bonds (DB) in a-Si are generated during irradiation and electrical properties can be recovered by proper annealing process. Similarly, the SWE is also observed in SRSO samples [68] and the electrical properties can be restored again by subsequent annealing. In contrast to a-Si, the only difference is that the SWE in SRSO samples has a slower response to the laser irradiation and it can be explained that DB related

defects in SRSO is more stable due to higher Si-O bond dissociation energy in comparison to Si-H or Si-Si one in a-Si. In addition, we can expect that the SWE can be helpful in understanding the PL quenching phenomenon in laser irradiated SRSO.

Except for reversible change in SRSO like SWE mentioned above, the other type of change is irreversible like laser ablation. A recent review [69] describes studies on the laser induced ablation and damage in SiO₂ in theory and experiment, and several related mechanisms based on different irradiation time are proposed. In the case of long pulse or continuous wave laser irradiation, the main light solid interaction mechanism is considered as intrinsic absorption and thermal diffusion model can be employed to explain the formation of typical crater morphology. The investigations on laser ablation in SRSO focuses on exploring the shrinkage of SRSO layer thickness or ablation thickness induced by continuous wave(CW) [70] or pulsed laser [71] and the threshold laser intensity of ablation-free can be obtained with extrapolation. In our recent study [72], we measured the surface profile of CW laser annealed SRSO with both AFM and TEM to explore the reason of surface modification.

Temperature distribution in samples during laser irradiation can not be simply evaluated. Actually there are two methods mentioned in literatures to estimate the local temperature. One method is based on the Stokes and anti—Stokes peak integrated intensity in Raman spectra, which has been applied to Si samples [73]. The formula is written:

$$\frac{I_S}{I_{AS}} = \exp\left(\frac{\hbar\omega}{k_B T}\right) \quad (1.1)$$

where I_S and I_{AS} represent the intensity of Stokes and anti-Stokes peak, respectively; ω is the frequency of Raman shift peak; k_B is the Boltzmann constant; T is the temporal average temperature of sample during laser illumination. Eq. (1.3) has been used to predict the average temperature of nc-Si particles in the irradiated SRSO samples by L. Khriachtchev [74]. As this measurement is usually proceed after SRSO samples are irradiated and the accurate way can be the employment of the same laser intensity to obtain the Raman spectra. In this case, it should assume that the second irradiation for Raman measurement induces no structural change like the growth of nc-Si particles and crystallization of irradiated SRSO samples. The drawback of this method is that it is only applies to estimate the temperature in crystalline sample and in case of irradiated SRSO sample the deposited energy does not load only on the nc-Si but the SRSO/SiO₂. Thus, the

contribution to local temperature from silicon oxide matrix during heating is neglected. The other method to predict the laser thermal effects is through optical absorption of samples and this idea comes from the formation of dome-shaped surface in fused silica after laser irradiation [75, 76, 77, 78, 79]. Following the work by T. Shiu et al. [80] and C. Lin et al. [70], the absorbed energy per unit volume per unit time from a Gaussian laser beam is written:

$$\dot{g}(r, z) = \alpha(1 - R) \times \frac{2P}{\pi\omega^2} \times \exp\left(\frac{-2r^2}{\omega^2}\right) \times \exp(-\alpha z) \quad (1.2)$$

where α , R are the absorption coefficient and the reflectivity of samples; P is the laser power and $\frac{2P}{\pi\omega^2}$ equals to laser intensity with a unit of W/cm^2 ; ω is the width that the intensity falls to $1/e^2$ of axial intensity; r and z are the radial direction and the depth from the sample surface. Thus, the local temperature $T(r, z)$ can be written:

$$T(r, z) = \frac{\dot{g}(r, z)\tau}{\rho C_p} = \frac{\alpha(1 - R)}{\rho C_p} \times \frac{2P}{\pi\omega^2} \times \tau \times \exp\left(\frac{-2r^2}{\omega^2}\right) \times \exp(-\alpha z) \quad (1.3)$$

where τ is the irradiation time; ρ and C_p are the density and the specific heat of samples respectively. When z equals to zero, which is corresponding to the sample surface temperature, we have

$$T(r)_{surface} = \frac{\alpha(1 - R)}{\rho C_p} \times \frac{2P}{\pi\omega^2} \times \tau \times \exp\left(\frac{-2r^2}{\omega^2}\right) \quad (1.4)$$

And the surface temperature has a Gaussian distribution in radial direction. However, the limitation of this method is apparent. The structural change during laser irradiation alters optical properties of SRSO samples. For instance, the shrinkage of optical band gap [81] when nc-Si particles are once generated and the optical absorption will have a strong increase, which can lead to a rise of local temperature. Thus, this method may be only available to estimate the initial local temperature during laser irradiation.

1.1.5 Characterization methods overview

Since optical properties, in principle, strongly depend on structure, an approach to fully understand the microstructure evolution of SRSO before and after annealing, laser irradiation or other treatments is mandatory. Actually, all the structures

involved in PL properties can be classified into amorphous and crystalline solids. The amorphous part confirmed by the TEM related methods until now contains SRSO, a-Si, SiO₂ while the crystalline part only has Si nanocrystals. The structure of amorphous solids is usually studied by X-ray and neutron diffraction to obtain the radial distribution function and the pair distribution function can be derived. The comparison between experiments and calculations provides refinement of atomic models. However, involving in structure of nano-scale amorphous solids, the X-ray and neutron diffraction is inappropriate due to low scattered signal and bad spatial resolution in nanovolumes. TEM has performed great advantages of detecting amorphous solids in nanovolumes because of high scattering cross section and detailed discussion can be seen in a recent review by D. Cockayne [82]. Although the spatial resolution of TEM can reach the atomic scale, the long-standing problem in the field of amorphous solids is still the unclear disordered structure. It is interesting that concerning of amorphous semiconductors, the structural characterization can be extended to spectroscopic methods like Raman and Fourier-transform infrared spectroscopy (FTIR) which reflect vibration of molecules and interatomic bonds. In addition, the composition of disordered semiconductor can be explored by XPS through valence state of atoms.

Method	Function	Spatial resolution	Examples
XPS	chemical composition; bonding environment	20 μm	SiO ₂ (103.4 eV) Si (99 eV)
Micro-Raman	vibration of phonon	1 μm	c-Si (521 cm^{-1}) a-Si (480 cm^{-1})
FTIR	vibration of Si-O bond	5 μm	stretching(1073 cm^{-1}), rocking(780 cm^{-1}), bending(450 cm^{-1}) modes for SiO ₂
Micro-PL	PL peak and intensity	1 μm	light emission mechanism
DFTEM	nc-Si immersed in amorphous background	1 nm	size distribution of particles
HRTEM	lattice imaging of nc-Si	0.24 nm	nc-Si embedded in amorphous matrix
EFTEM	chemical mapping of microstructure	0.24 nm	nc-Si embedded in amorphous matrix; a-Si nanocluster
EELS	chemical environment of atoms	1 nm	Si and SiO ₂ plasmon peak
EDX	chemical composition	1 nm	chemical mapping local composition

Table 1.1: The comparison of different characterization methods in annealed or irradiated SRSO samples.

Since the silicon processing technology has been developed very well in the last 60 years, the PL yield of low dimensional silicon system stimulate the coupling of sil-

icon electronics and photonics (Integrated silicon photonics). To fabricate Si light emitting device on a single silicon-based chip, laser irradiation with beam spot at micron or submicron scale is required. Therefore, the characterization methods with spatial resolution of micrometer and nanometer are proper to explore the microstructure of laser irradiated volume. Table 1.1 lists a variety of characterization methods and their features. XPS provides the information of chemical composition and bonding environment. Since the valence state of Si atom in pure Si and SiO₂ is different, the corresponding Si 2p peaks can be used to undergo the components analysis. For instance, XPS analysis has been applied in the structural evolution of thermally annealed SRSO samples [83]. However, XPS is only sensitive to the surface of sample which may limit the application of XPS analysis in depth of samples. Moreover, the spatial resolution of XPS is about 20 μm shown in table 1.1 which can not be employed to detect the internal microstructure of irradiated SRSO samples with small beam spot(10 μm). In other words, in this case the XPS only provides the average structural information. Similar condition can be seen in FIIR with a finer spatial resolution of 5 μm . The typical studies on the decomposition of SRSO and the related phase separation [84] with FTIR has been reported in literatures. Although FTIR is successfully used in a recent report concerning macroscopic phase separation [85] in SRSO driven by CW laser irradiation, the spatial limitation still exists. PL and Raman spectral with much finer spatial resolution of 1 μm can show well-spatially resolved optical and structural properties of laser irradiated samples. The most interesting approach can be the in-situ PL and Raman measurements can be simultaneously performed during laser irradiation [86].

To characterize the micro-structure of such small irradiated area, TEM can be the most powerful tool due to its ultra high resolution. Table 1.1 also lists several main TEM based methods: there are DFTEM, HRTEM and EFTEM for imaging while the spectroscopic technology includes EELS and EDX. DFTEM with a spatial resolution of 1 nm has been employed to image the Si nanocrystals embedded in SiO₂ [87][88]. The bright contrast in DFTEM image originate from the electron diffraction by the atomic plane of nc-Si particles, which couples with incident electron beam by Bragg condition, and the dark contrast as the background represents the amorphous silicon oxide matrix. As the DFTEM can be worked at a low magnification, it provides mesoscopic scale structural information of samples. In special case of irradiated sample at the micro scale, we have employed hollow cone dark field imaging (high contrast imaging compared to DFTEM) to display the internal

microstructure of irradiated SRSO sample in a macroscopic way [89]. Thus, the size distribution of particles in the whole sample can be estimated in a statistical way. However, the drawback of DFTEM is that part of nanoparticles are invisible due to the strict Bragg condition. Because the angle of incident electron beam is usually fixed and a portion of particles may not couple with this angle.

HRTEM with atomic level resolution provides more detailed information of one single nanoparticle and its environment. For a typical field emission gun TEM operated at 200KV, the spatial resolution of HRTEM is about 0.19 nm as presented in Table 1.1. Whereas in experiment HRTEM has been confirmed to show difficulties in distinguishing very tiny nc-Si particles (less than 1.2 nm) from silicon oxide matrix [90][88]. This invisible effect may stem from the thickness of sample and the mismatch of these particles with the Bragg condition. The simulation on imaging of random oriented nanoparticles [91] has indicated that the Bragg rule for HRTEM can be relaxed if the thickness of sample is very thin and this increases the possibility of detecting these tiny particles.

EFTEM is one imaging method based on EELS (mentioned in the next paragraph). In contrast to HRTEM, EFTEM can provide a chemical mapping with the same spatial resolution of HRTEM. Thus, with this method, it is possible to distinguish the tiny nc-Si particles or the potentially existing a-Si cluster from amorphous matrix. A good example of EFTEM application can be found in F. Iacona et al.'s study on structural evolution of annealed SRSO sample with temperature [92]. The energy window of Si (centered at about 17eV) plasmon peak at low energy loss region (0-50 eV) are selected to do the chemical mapping of Si and they give the conclusion that there are three regimes involved in the decomposition of SRSO when the temperature increases from 900 to 1100 °C: a).the starting of phase separation; b).the existence of a-Si cluster; c).the crystallization of a-Si cluster.

The spectroscopic methods like EELS and EDX usually require the electron beam to work in STEM mode. Thus, the spatial resolution of these methods is mainly determined by the probe size of electron beam. In principle, the size of electron beam can be focused to a minimum of 1.22λ following the Abbe diffraction limit where λ is the wavelength of electron (For 200kV, $\lambda=2.51\text{pm}$). Actually, the probe size is much larger than the 1.22λ due to different factors like spherical aberration and aperture size. Moreover, the reducing probe size often accompanies with high scattering angle which can induce the convolution of the collected data. Thus,

the probe size and scattering angle should reach a compromise and the size of quasi-parallel incident electron beam in the best condition is about 1nm. Both EDX and EELS can provide the chemical mapping, local composition analysis and TEM sample thickness measurement.

1.2 The main development in micro-structure investigation

The fabrication of nc-Si particle from SRSO samples has been achieved by several methods like thermal annealing [93, 94, 95], ion bombardment [96] and laser irradiation. In principle, these treatments can be considered as energy deposition processes on samples. It has been mentioned that PL mechanism especially light emission center in treated SRSO samples is still an open question. Thus, the exploration of related microstructures should be another valuable approach to properties. In this section, we will introduce the main development in microstructural study of thermally annealed and laser irradiated SRSO samples.

1.2.1 Thermally annealed SRSO

Microstructural study of thermally annealed SRSO samples, in general, can be divided into two types: in variation of annealing temperature and time evolution.

Early work on micro-structure of SRSO samples in variation of temperature was based on FTIR technique, because it is a direct and fast way of characterization. At the beginning, some basic knowledge in FTIR will be introduced as follows. Theoretical and experimental studies in FTIR spectrum of SRSO or SiO₂ [97, 98, 99] have indicated that three vibrational modes exist for motion of O atoms, and they are Si–O rocking, bending and stretching modes. It should be noted that IR absorption peak position and the shape of the peak strongly depend on the mixing of Si and O atoms. Regularly the Si–O stretching mode with intensive signal is employed to discuss the structure of SRSO in the literatures, because O atom is usually coupled by two Si atoms and motion of O atom reflects two Si–O vibrations (ie. Si–O–Si bridge) [38]. For thermally grown SiO₂, it has been

evidenced [100, 101, 102] that the peak position of Si–O stretching mode is near 1073 cm^{-1} . The shift of this peak position in SiO_x towards 1073 cm^{-1} when x value increases has been reported by several researchers [38, 103]. One of the

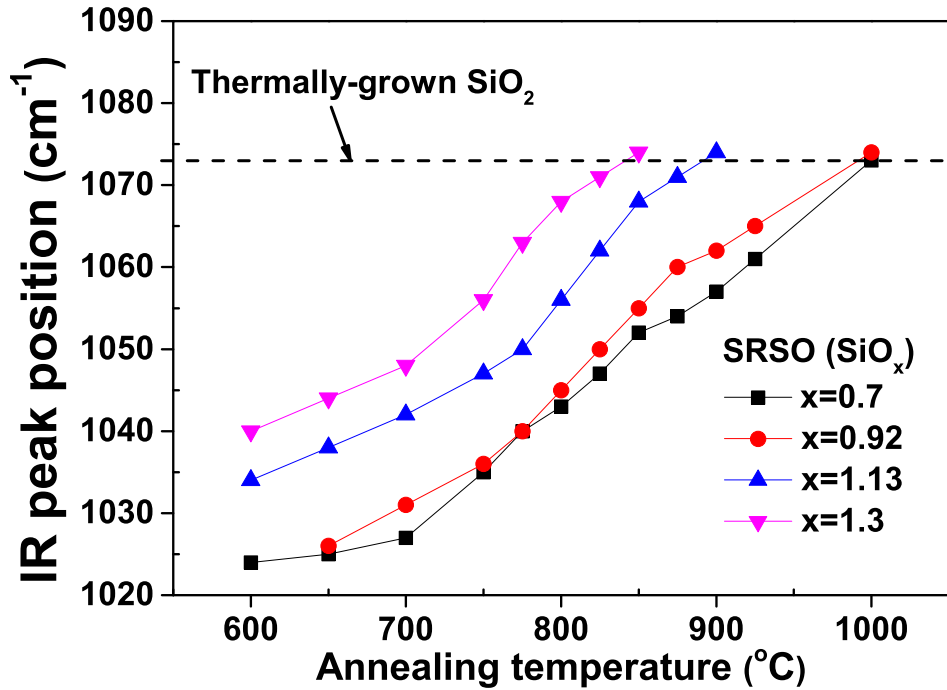
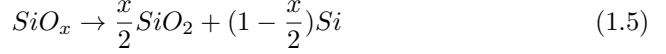


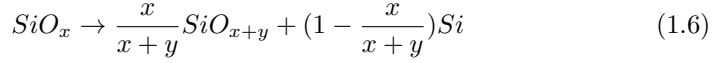
Figure 1.5: The IR peak position of Si–O stretching modes in SiO_2 samples with different oxygen content in variations of annealing temperatures. The annealing time at each given temperatures is fixed as 6 mins. It is clearly seen that the shift of peak position towards that in $\text{SiO}_2(1073\text{ cm}^{-1})$ when the temperature increases. At higher annealing temperature (ie. $850\text{ }^\circ\text{C}$ for $\text{SiO}_{1.3}$ sample), a single SiO_2 phase may be formed. These data points are reproduced from the results [84] from B. J. Hinds and co-workers.

most meaningful results concerning of temperature evolution is the variation of Si–O stretching mode in the stepwise annealing process [84] as presented in Fig. 1.5. The resident time at each given temperature is 6 mins. It can be seen that all samples with different oxygen content (x value) enjoy the tendency that the peak position of Si–O stretching motion shifts towards 1073 cm^{-1} when annealing temperatures increases. Similar tendency can be seen when the oxygen content of pristine SRSO samples increases mentioned above. However, the average oxygen content in samples is unchanged during thermal process. Thus, it implies that the oxygen rich region is formed in SRSO during annealing process. In addition, at

high temperature like 850 °C for SiO_{1.3} sample, the peak position is as same as that in SiO₂, which may indicate that a single SiO₂ phase is precipitated from SRSO with higher deposition energy. And the existence of Si nanocrystals in this sample has been confirmed by HRTEM investigations. Considering this, the phase separation in SiO_x can be written:



Eq. (1.5) describes that SRSO is decomposed into two thermodynamically stable phases Si and SiO₂. Actually, Eq. (1.5) can be written in a general way like:



Eq. (1.6) implies that there are some intermediate states like oxygen-rich silicon suboxide in SRSO decomposition.

To reflect the kinetics in Eq. (1.5) and Eq. (1.6), the investigation on microstructural evolution with time is mandatory. Concerning of this, reaction extent that describes the stage of SRSO decomposition reaction is introduced [84]. It should be noted that oxygen content in SRSO is a linear function of stretching peak position [104][99], therefore, reaction extent α can be written as a function of vibrational frequency [84]:

$$\alpha = (\nu_m - \nu_i) / (\nu_f - \nu_i) \quad (1.7)$$

where ν_m is the frequency of Si—O stretching modes in annealed sample; ν_i is the frequency of Si—O stretching modes in pristine SRSO samples, which represents the initial stage in decomposition reaction; ν_f is the frequency of Si—O stretching modes in SiO₂ samples, which implies the final state in reaction. Thus, α equals to 0 for pristine SRSO samples and equals to 1 for SiO₂. The results reflects the extent in time evolution [84] provided by B. J. Hinds is presented in Fig. 1.6. It is interesting that in the extent increases very fast in the initial five seconds (rapid thermal annealing) and after that has a slow rise until it tends to be a constant in prolonged annealing time. As Si nanocrystals can not be observed after lower temperature annealing process ($T_{\text{annealing}} \leq 800$ °C), however, they are visible after higher temperature annealing process ($T_{\text{annealing}} \geq 900$ °C), the authors regarded that initially SRSO is decomposed into a-Si and SiO₂ in a short time and after that the SiO₂ wrapping a-Si as shell is the diffusion barrier to protect the nucleation of

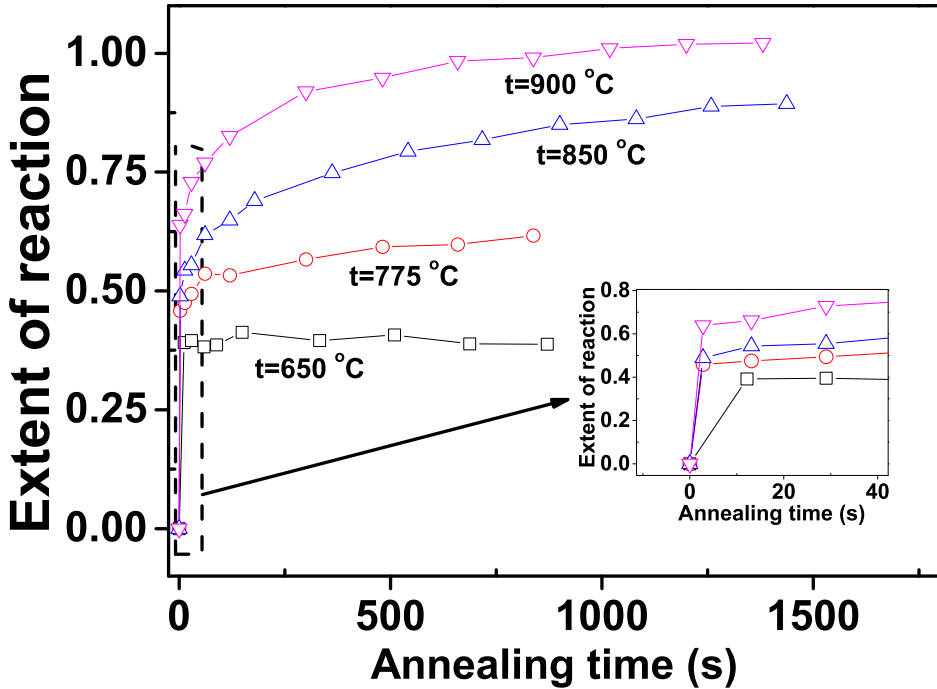


Figure 1.6: The variations of reaction extent of as $\text{SiO}_{0.93}$ sample at different annealing temperatures with time evolution. The growth rate of extent is very rapid in initial short thermal process (5–10s) clearly presented at inset and after that this rate is reduced. These data points are reproduced from the results [84] from B. J. Hinds and co-workers.

a-Si and the growth of SiO_2 volume. Samples annealed at higher T ($T_{\text{annealing}} \geq 900$ °C) with the formation of nc-Si particles implies that this barrier can be overcome by higher diffusion length of atoms. In relation to this kinetics process, further studies based on 1D and 3D Avrami-Erofe'ev model [105, 106, 107] have been approached [84]. The point of view in this work is that the initial formation of a-Si can be regarded as phase growth at the 1D dimensionality while the nucleation of a-Si to Si nanocrystal and further growth of nc-Si particles may be considered as the 3D phase growth.

Except for FTIR, other spectroscopic methods like Raman and XPS are also usually employed to detect the decomposition process of SRSO. Raman spectra characterizes the vibrational properties of phonons in materials and the position, intensity width, shape of Raman shift peak represented a-Si, c-Si and nc-Si can be obtained to know structural information. XPS can provide O 1s peak and Si 2p

peak, and the energy of Si 2p peak is 103.3 eV for SiO₂ and 99.7 eV for Si respectively [108]. With these peaks, the chemical composition of sampled can be known.

Although all the spectroscopic methods mentioned above provide a lot of useful structural information about the decomposition of SRSO, the limitation of them is spatial resolution which has been mentioned in section 1.1.5. For example, even the advanced setup laser-assisted Raman microscope still has a spatial resolution of 1 μm , which can not give the microstructural properties at nanoscale. In other words, these methods provide the average structural information [109] which do not strongly reflect the phase separation like the formation of Si nanocluster and further growth.

To characterize the microscopic phase separation in SRSO, several techniques based on TEM with the very high spatial resolution (subnanometer to nanometer) like EELS, EFTEM, EDX, hollow-cone dark field TEM imaging (HCDF) and HRTEM are introduced, which also have been discussed in section 1.1.5. One typical EFTEM investigation on structural evolution of luminescent Si nanoclusters in thermally annealed SRSO samples has been reported by F. Iacona and co-workers [92]. In this study, the evidence of a-Si nanoclusters formed at lower annealing temperature and the formation of nc-Si particles at higher one have been clearly provided. In addition, the related particle growth kinetics is also discussed. However, The kinetics of particle growth in SRSO is still controversial due to the missing of in-situ direct observation. Early work have indicated that atomic self-diffusion process dominates growth procedure and the diffusion of Si atoms is towards the nucleation sites [110]. And in some subsequent study, the size of particles in experiment is larger than the expected one based on self-diffusion procedure [92][88]. Therefore, Ostwald ripening effect [111][112] is considered to assist particle growth.

1.2.2 Laser annealed SRSO

Laser annealing is another interesting method to induce phase separation in SRSO samples. In contrast to thermal annealing, laser annealing has several unique advantages. Firstly, thermal load on samples can be controlled temporally and spatially to form new structures. For instance, the applications in recrystallization of

a-Si and the surface amorphization of Si have simplified the silicon-based semiconductor technology. In particular, if the substrate is insulator with weak thermal conductivity, normal thermal treatment for samples usually requires longer periods, however, laser annealing is less-time consuming and it can only heat the surface or top thin films not substrate with accurate adjustment. Another advantage is that this localized thermal treatment will not damage nearby materials that couples well with Si integrated circuit technology. Last but not least, surface layers' dimension or scale can be modified and Si nanocluster generation from SRSO is a typical example of reducing scale.

Laser annealing of SRSO has employed pulsed excimer lasers [113, 114, 115, 71], ultrashort pulse lasers [116] and continuous wave lasers [74][85]. It should be noted that high local temperature is required to induce phase separation of SRSO into Si and SiO₂. Concerning of this, pulsed laser irradiation can give rise to strong thermal effects in samples. For example, Si surface melting by pulsed laser annealing and its related mechanism have been studied by M. O. Thompson et al. [117]. Another example is laser ablation of SRSO [71]. To avoid laser induced damage that can quench the PL yield, continuous waver laser annealing with intermediate thermal effect, which has ability of inducing phase separation in SRSO samples, is also usually employed by researchers. No matter the employment of pulsed laser or CW laser, in some literatures it has been indicated that the formation of nc-Si particles in SRSO requires at least 20 ms by laser annealing and this time scale is insufficient to the occurrence of self-diffusion process that dominates the nc-Si particle formation in thermally annealed SRSO samples. Therefore, the microstructural study of laser annealed SRSO samples with time evolution can reflect the related kinetics. For instance, one interesting work [118] is the evolution of nanocrystalline fraction extracted from Raman results with annealing time as presented in Fig. 1.7. As two Raman shift peaks in laser annealed samples are observed: the sharp one represented the nc-Si at 521 cm⁻¹ and the broad one indicated the formation of a-Si at 480 cm⁻¹, the fraction can be estimated based on integrated intensity of these two peaks. The average size of nc-Si (R) is evaluated through the position and width of nc-Si Raman shift peak [119], which stems from phonon confinement model [120]. All these curves in Fig. 1.7 indicate that R keeps unchanged when annealing time increases. This can be considered that the formation of nc-Si particles only consumes the a-Si components in SRSO [119] and once nc-Si is formed, the particle growth is not very apparent with prolonged time. The possible reason is that local temperature through absorption of laser beam is not

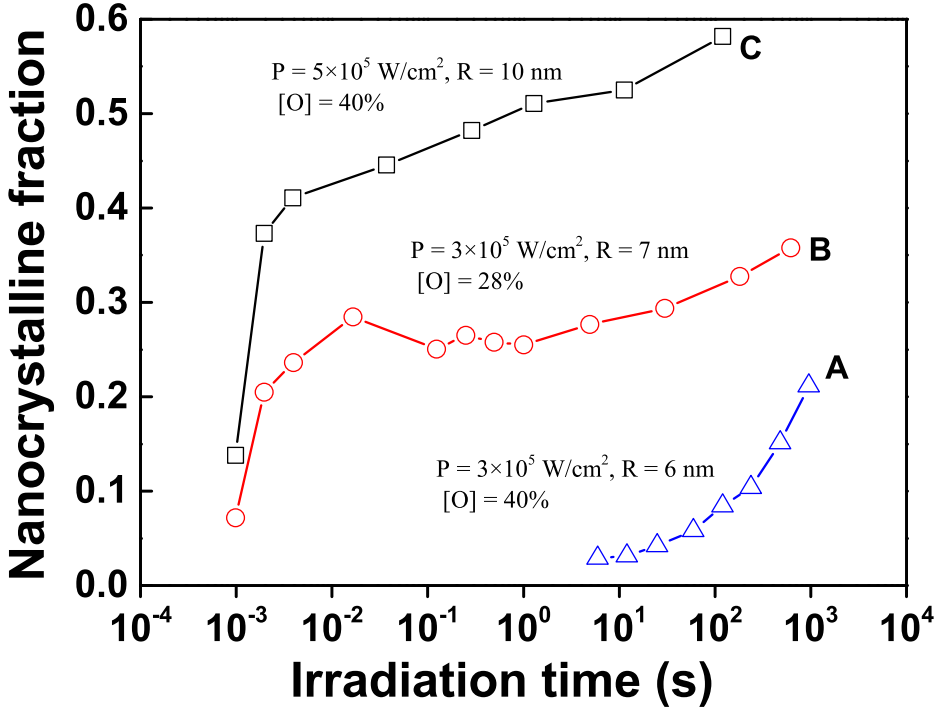


Figure 1.7: Time evolution of the nano-crystalline fraction in SRSO with different oxygen content by CW laser irradiation. The unchanged average size R with increasing illumination time implies that the formation of nc-Si particles accompanies with the consumption of a-Si and there is no apparent growth once nanocrystals is formed with prolonged irradiation. These data points are reproduced from the results [118] from M. C. Rossi and co-workers.

high enough to assist the diffusion of Si to overcome the barrier (SiO_2 shell or rich oxygen region in SRSO). This can also be evidenced by the comparison between A and C curves. The higher laser power generates the larger nc-Si particles for the same pristine SRSO samples. In addition, the comparison between A and B curve indicates that the R also depends on the oxygen content of sample.

On the other hand, it has been mentioned above that CW laser irradiation with intermediate thermal effect have a great potential to induce the completed Si and SiO_2 phase separation in SRSO samples [121][74]. And the free-standing SRSO films or Si/ SiO_2 superlattices are usually needed to avoid the thermal flow into the substrate [122].

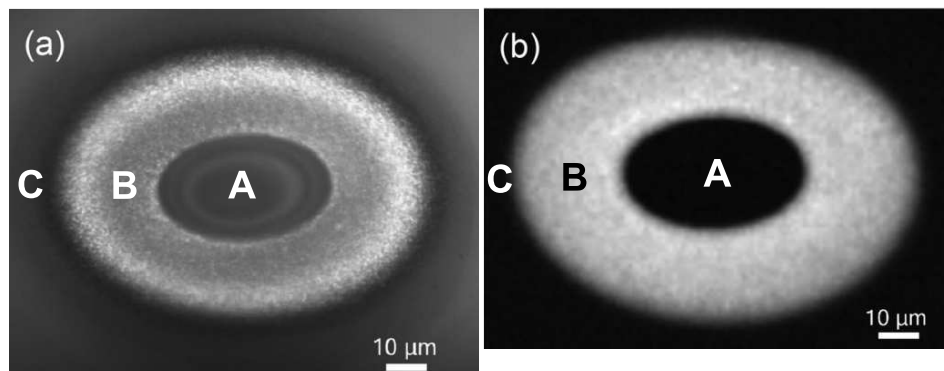


Figure 1.8: (a) Optical microscope image and (b) Raman map of irradiated spot in SRSO by CW laser irradiation [85]. Three visible inhomogeneous regions (the center (A), the ring (B) and the outer of the ring (C)) can be observed. A strong signal of *c*-Si from region B indicates the occurrence of crystallization in SRSO.

Recently, L. Khriachtchev et al. employed CW laser irradiation to induce a macroscopic Si–SiO₂ phase separation [85] in free standing SRSO films. The authors used several methods, which include micro-PL, micro-Raman spectra, EELS and EFTEM with fine spatial resolution, to analyze optical and structural properties of annealed samples. Fig. 1.8(a) presents the optical image of annealed area and it is clearly observed that the variation in optical properties can divide the samples into three inhomogeneous regions: the center (A), the ring (B) and the outer of the ring (C). Accordingly, the Raman map with filtered band from 510 to 540 cm⁻¹ (crystalline Si) is presented in Fig. 1.8(b). The B region shows strong Raman signal that means the Si crystallization occurs. To characterize the properties with fine spatial resolution, the authors measured micro-PL, micro-Raman spectra, transmission and the results are depicted in Fig. 1.9. The micro-Raman cross section corresponding to the Raman map in Fig. 1.8(a). It is interesting that the PL intensity in the region A and B is very weak but strong in region C. This can be understood through EELS and EFTEM studies [85]. The weak PL in region A is due to the formation of pure SiO₂ and the weak PL in region B is considered as the degradation of QC effect because the average diameter of nc-Si is too large (100 nm). The mean size of nc-Si in region C is about 23 nm, which is regarded to be responsible to the appearance of PL. The transmission in region C is similar to the annealed SRSO sample at 1100 °C [123] while the low transmission in region B may be due to the absorption of nc-Si particles and Rayleigh scattering. In addition, the macroscopic Si–SiO₂ phase separation was explained as the thermodiffusion of

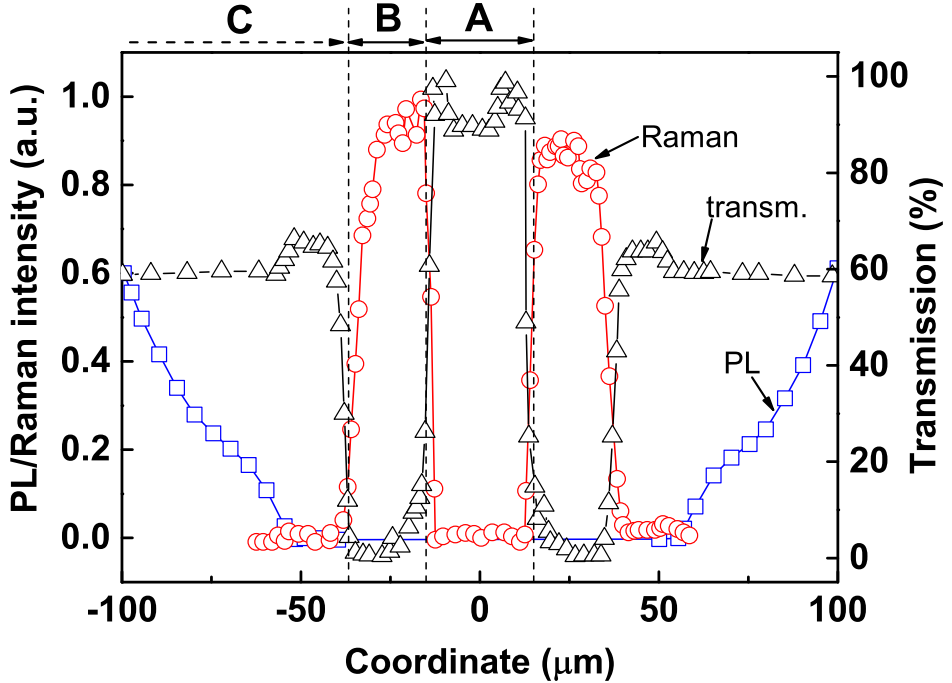


Figure 1.9: (Raman, PL and transmission of the laser-annealed area. The Raman signal is consisted with that in Fig. 1.8(b). The PL intensity in region A and B is quite weak while a intensive PL can be observed in region C where is not the irradiated spot area but the irradiation affected area. In contrast to region A and C, the transmission in region B is quite low due to the absorption and scattering of large nc-Si particles. These data points are reproduced from the results [85] from L. Khriachtchev et al..

Si clusters driven by temperature gradient [124, 125] by authors.

1.3 The contribution of our work in micro-structure investigation

In this thesis, we mainly employed CW laser irradiation with a beam spot of approximately 6 micrometers to heat fused silica bounded SRSO samples. The optical properties of samples are characterized by a PL microscope, which provides the intensity distribution of luminescence. The profile of samples' surface and the

related roughness are measured by atomic force microscopy (AFM). Preliminary microstructural analysis in samples is performed by micro-Raman method. TEM, the most powerful tool in microstructural investigation with ultra high spatial resolution, and its derivative methods like HCDF, HRTEM, EELS, EFTEM, EDX and tomography are used to give the systematic structural investigation of CW laser irradiated SRSO samples. In this section, I will introduce the main contributions in this thesis and state their significance.

1.3.1 Damage-free laser irradiation and spatially controlled microstructure

It has been mentioned that substrate bound SRSO samples are difficult to achieve high local temperature to induce phase separation by laser irradiation due to heat flow into the substrate. And this is the reason that free-standing SRSO samples are preferred. The chapter 2 states that the formation of nc-Si particles is practical in fused silica bounded samples. The accurate control of laser intensity lead to optically smooth surface without any deterioration.

The combination of spatially resolved PL intensity and miro-Raman results initially indicates that amorphous silicon formed in SRSO at the edge of laser heated area is responsible for the strong PL while the PL in the centered area is not expected to be strong where nc-Si particles are formed. The spatially resolved microstructure in laser irradiated or affected area is firstly shown by HCDF techniques.

The sense of this work is that proper parameters in CW laser annealing can give rise to the generation of Si-nanocrystals even in substrate bound films and without influencing the optically smooth surface. And parameter optimization is quite useful for fabricating devices like Si based lasers.

1.3.2 The formation of porous region

The work in chapter 2 has preliminarily reported that high laser intensity leads to the formation of porous region at the top surface of samples, which may quench the

PL yield. EDX mapping and TEM tomography in chapter 3 evidence that these structures have porous character and are chemically close to SiO_2 . The systematic investigation of these porous silicon oxide is discussed in chapter 4. Based on several evidences from TEM related characterization for these structures, a model that describe the porous formation is proposed. Quantitative EDX study for porous is also discussed in chapter 4 and the potential kinetics has been suggested.

This investigation is expected to enrich the understanding of structural evolution in CW laser irradiated SRSO samples as this kind of porous silicon oxide is rarely reported in literature. It is interesting that the porous region is chemically close to SiO_2 , which may provide a novel way of phase transitions in SRSO to a stable state except for the decomposition into Si and SiO_2 . In addition, it is known that usually the fabrication of porous silicon oxide is through chemical etching methods and laser irradiation with accurate microstructure control is expected to produce homogeneous features.

1.3.3 The nanoscopic phase separation

Since the Si- SiO_2 macroscopic phase separation reported in CW laser irradiated free-standing SRSO samples can not be evidenced by our materials system, we focus on the nanoscopic phase separation (ie. the formation of nc-Si and SiO_2 shell). Such a shell is difficult to be directly observed due to several reasons like quite small difference with amorphous matrix (ie. SRSO). In this work shown in chapter 5, we mainly employ EDX and EELS for local composition analysis of nc-Si region. Our results mainly indicate that Si- SiO_2 nanoscopic phase separation occurs in our materials system after CW laser irradiation.

This work opens one window that EDX analysis with simulation can be a new way to characterize the phase separation in irradiated SRSO samples. And it is expected that much finer structure models will be proposed to give more comprehensive knowledge in related kinetics process in future.

2 Generation of silicon nanocrystals by damage free CW laser annealing of substrate-bound SiO_x films

T. Fricke-Begemann,¹ N. Wang,² P. Peretzki,² M. Seibt,² J. Ihlemann¹

¹Laser-Laboratorium Göttingen, Hans-Adolf-Krebs-Weg 1, 37077 Göttingen, Germany

²IV. Physikalisches Institut, Universität Göttingen, Friedrich-Hund-Platz 1, 37077 Göttingen, Germany

<https://doi.org/10.1063/1.4931670>

Silicon nanocrystals have been generated by laser induced phase separation in SiO_x films. A continuous wave laser emitting at 405 nm is focused to a 6 μm diameter spot on 530 nm thick SiO_x films deposited on fused silica substrates. Irradiation of lines is accomplished by focus scanning. The samples are investigated by AFM, TEM, Raman spectroscopy and photoluminescence measurements. At a laser power of 35 mW corresponding to an irradiance of about $1.2 \times 10^5 \text{ W/cm}^2$ the formation of Si-nanocrystals in the film without any deterioration of the surface is observed. At higher laser power the central irradiated region is oxidized to SiO₂ and exhibits some porous character, while the surface remains optically smooth, and nanocrystals are observed beside and beneath this oxidized region. Amorphous Si-nanoclusters are formed at lower laser power and around the lines written at high power.

2.1 Introduction

Silicon nanocrystals are of interest as integrated light emitters in silicon based photonics [126][127]. They are mainly fabricated by high temperature annealing of substoichiometric SiO_x , also known as silicon-rich silicon oxide, leading to a phase separation into Si and SiO_2 [128]. The initial SiO_x films can be prepared by a number of thin film deposition technologies including thermal evaporation, e-beam evaporation [128], chemical vapor deposition [87], and pulsed laser deposition [129]. Another technique, leading to SiO_x films with slightly different properties, is the implantation of Si ions into SiO_2 films or silica glass [130]. At annealing temperatures below 900 °C mainly amorphous Si clusters are formed, at higher temperatures nanocrystals with diameters up to 10 nm are observed [131]. For the fabrication of size controlled nanocrystals a superlattice approach starting with a stack of alternating layers of SiO_x and SiO_2 has been developed [132]. Strong visible to infrared photoluminescence of clusters and nanocrystals is attributed to quantum confinement and defect states at the boundary between nanocrystal and surrounding matrix [133][134][32].

Laser annealing instead of furnace annealing offers the possibility to generate nanocrystals locally controlled. Furthermore the thermal load of the substrate can be reduced enabling processes that do not allow high temperatures. Laser annealing has been performed using pulsed excimer lasers [86][113][71][114], ultra-short pulse lasers [115] and CW lasers in the visible [116] and IR [135] spectral region. After laser annealing in inert gas luminescent clusters and nanocrystals have been found, after annealing in air complete oxidation of the material to SiO_2 is observed [136]. The main problem of the laser annealing process is the collateral damage of the films ruling out this process for device fabrication up to now [113][137].

To obtain the high temperatures required for substantial nanocrystal formation, laser annealing at 488 nm has been performed on free standing multilayer films [68][85]. In this case the heat dissipation to the substrate can be avoided and temperatures up to 1600 °C can be reached leading to the formation of nanocrystals and amorphous silica material. In addition to this microscopic phase separation a macroscopic phase separation is assumed: Si-nanoclusters formed in the center of the laser beam move to outer regions by thermodiffusion due to the laser generated temperature gradient [138][139]. In this paper we show that appropriate laser

parameters can lead to the formation of Si-nanocrystals even in substrate bound films and without influencing the optically smooth surface. Such conditions are necessary for fabricating devices like wave guides for photonic applications.

2.2 Experimental

For the experiments shown here, the SiO_x films are deposited on 2 mm thick fused silica substrates by ion beam sputtering (IBS), conducted by a commercial coating supplier (Laseroptik, Garbsen, Germany). The process uses silicon as a sputter target while the stoichiometry of the films is tuned via a small supply of oxygen process gas. The SiO_x films used in the present experiments exhibit a stoichiometry factor $x \approx 1$, as can be deduced from transmission and reflection spectroscopy measurement. The films with a thickness of 530 nm show a transmission of 15% at 405 nm wavelength, corresponding to an absorption coefficient $\alpha = 3.4 \times 10^4 \text{ cm}^{-1}$. The index of refraction is $n = 1.85$ at 633 nm.

For locally resolved annealing, a diode laser with continuous wave emission at 405 nm (Coherent Cube) is focused by a 10x/NA 0.25 microscope objective lens onto the SiO_x layer. The laser has a close to Gaussian beam profile with a beam parameter product $M_2\pi/\lambda \approx 1.2$. The full $1/e_2$ -width of the focus formed by the microscope objective is evaluated to 6 μm . A typical laser power of 40 mW yields an average irradiance within the focal spot of $1.4 \times 10^5 \text{ W/cm}^2$ and a central peak power of $2.8 \times 10^5 \text{ W/cm}^2$. The SiO_x samples are enclosed in a small housing that is purged with a steady flow of nitrogen in order to prevent oxidation during annealing. Irradiation is then accomplished through a 1 mm thick fused silica window. The sample position is controlled by high precision positioning stages and the irradiation of lines is accomplished by moving the samples at a specified velocity. The correct focus distance is monitored by a confocal position control using the microscope objective as the front lens.

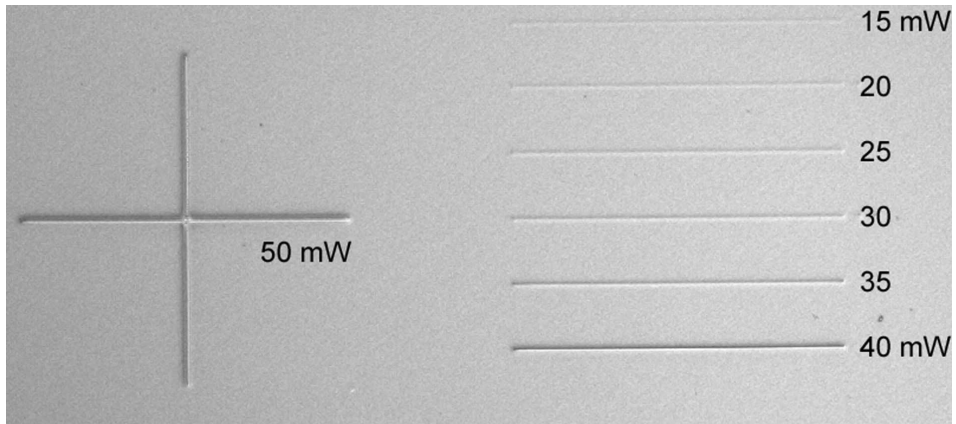
Luminescence is investigated at room temperature using a custom built epi-luminescence setup including laser excitation at 405 nm wavelength, a 40x microscope objective with numerical aperture 0.6, a scientific CCD camera and long-pass as well as band-pass emission filters. The surface area of the laser annealed lines are characterized by atomic force microscopy (AFM, Park XE150) and scanning electron

microscopy (SEM, Zeiss Evo100). Raman spectra are recorded with a confocal Raman microscope (LabRAM HR 800 UV, Horiba Jobin-Yvon) with excitation at 488 nm. The employed 100x/NA 0.9 microscope objective provides a resolution spot diameter of approximately 1 μm .

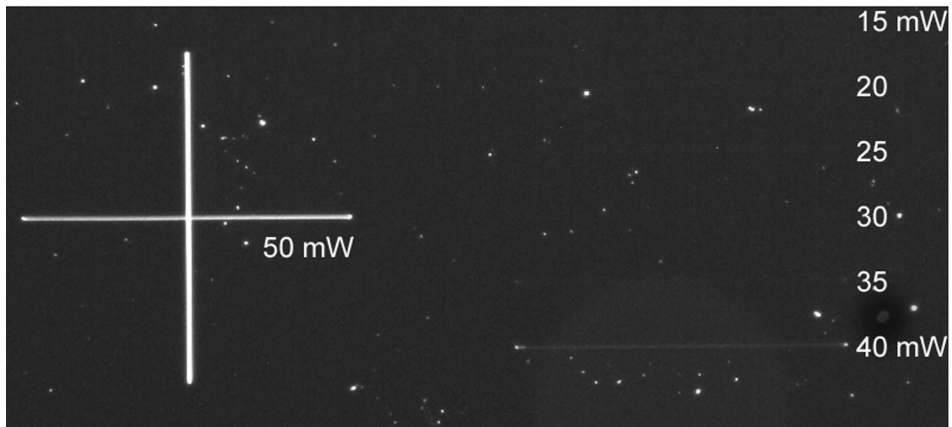
Focused ion beam (FIB, FEI Nova NanoLab 600) is employed to prepare cross-sectional TEM samples centered on the irradiated lines and oriented perpendicular to them. Prior to FIB preparation of TEM lamella, a thin Au layer (5 nm) is evaporated on the samples to avoid charging in FIB environment during SEM inspection. Electron transparent lamellas were prepared using a Ga ion beam focused to about 7 nm and a final thinning at beam voltage of 5kV. TEM analyses have been performed using a Philips CM200 FEG-UT operated at 200kV.

2.3 Results

Annealing of the SiO_x film at an irradiance above $0.35 \times 10^5 \text{ W/cm}^2$ (laser power 10 mW) causes a change in refractive index that can be observed by optical microscopy, e.g. using differential interference contrast as shown in Fig. 2.1(a). The depicted lines with varying laser power have a length of 500 μm and are written from right to left at constant velocity 300 $\mu\text{m/s}$, corresponding to an irradiation time of 20 ms. With increasing laser power, the lines get wider and gain visibility. However, only at an irradiance above $1.4 \times 10^5 \text{ W/cm}^2$ (laser power 40 mW), the annealing lines show an increased roughness and can be observed by dark field imaging (Figure 2.1(b)). Fig. 2.2 depicts photoluminescence (PL) measurements recorded from annealing lines that are irradiated with laser powers ranging from 30 mW ($1.0 \times 10^5 \text{ W/cm}^2$) to 50 mW ($1.75 \times 10^5 \text{ W/cm}^2$). In all cases, the maximum luminescence intensity can be observed at the edge of the lines with a local minimum of moderate intensity in the center. While the maximum intensity is approximately constant, the width of the luminescent area, and especially the width of the central region with moderate intensity increases with laser power. Lines that are annealed using irradiances of $0.7 \times 10^5 \text{ W/cm}^2$ (20 mW) and $0.9 \times 10^5 \text{ W/cm}^2$ (25 mW) reveal strong luminescence, too, but no central minimum. It should be noted, that fluctuations in luminescence intensity along the direction of the lines are caused by fluctuations in the excitation beam. The luminescence of the laser annealed lines covers a wide spectral range with emission



(a)



(b)

Figure 2.1: Optical microscopy images from laser annealed lines in SiO_x written with varying laser power as indicated. (a) Differential interference contrast; (b) dark field imaging.

from 500 to 1000 nm and emphasis in the red spectral region. In the central part of the lines with initially moderate intensity strong bleaching within a time scale of a few seconds can be observed. Minor luminescence can also be recorded from the untreated SiO_x film, predominantly in the green-red spectral region. Raman measurements that are recorded from the center of the laser annealed lines are presented in Fig. 2.3. For the lines annealed at 35 mW ($1.2 \times 10^5 \text{ W/cm}^2$) and above, the luminescence background is strongly reduced and the emergence of a distinct peak at Raman shift 521 cm^{-1} indicates the presence of crystalline silicon

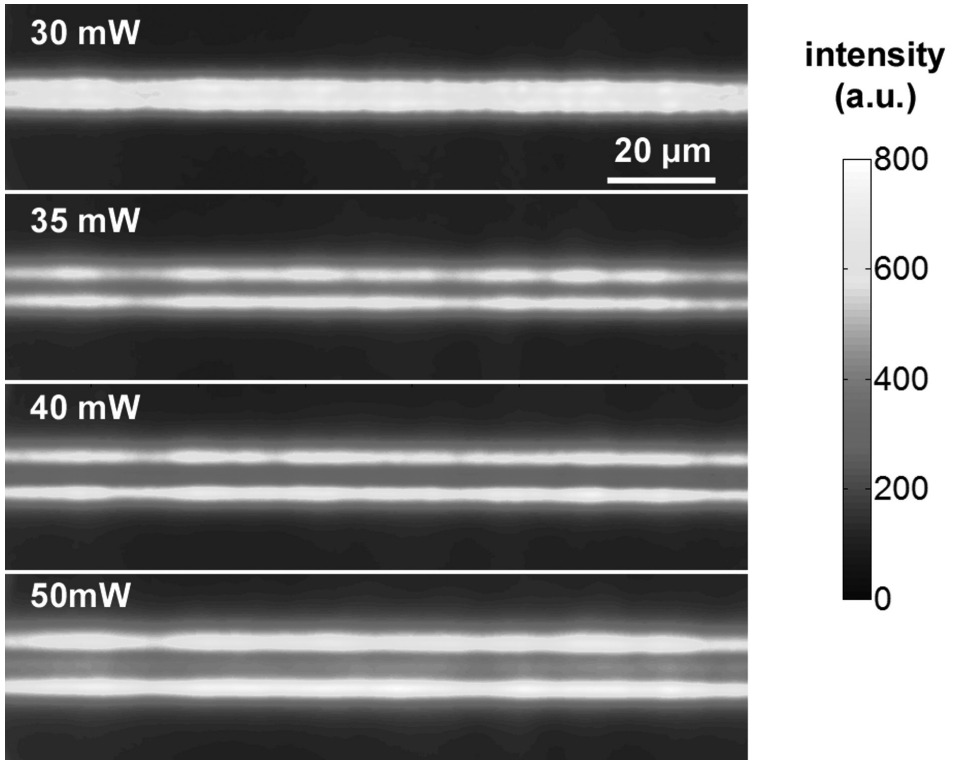


Figure 2.2: Photoluminescence images recorded from laser annealed lines in SiO_x written with varying laser power as indicated.

(c-Si). For the lines irradiated with laser powers in the range 30-35 mW ($1.0\text{-}1.2 \times 10^5 \text{ W/cm}^2$), the emergence of bands at 150 cm^{-1} and 480 cm^{-1} indicate the formation of amorphous silicon (a-Si) [140]. Raman spectra recorded from a single line ($1.4 \times 10^5 \text{ W/cm}^2$) but with increasing distance d_c to the line center are depicted in Fig. 2.4. In the center and at a distance of $1 \mu\text{m}$ the peak corresponding to crystalline silicon at 521 cm^{-1} dominates but shows a slight shoulder towards smaller Raman shift. Together with the band at 150 cm^{-1} , this shoulder might indicate some residual amorphous silicon. With increasing distance ($d_c = 2\text{-}3 \mu\text{m}$) from the line center, the bands corresponding to amorphous silicon at 150 cm^{-1} and 480 cm^{-1} become stronger. For a distance $d_c = 4 \mu\text{m}$ and above, the Raman spectra closely resemble those of the untreated SiO_x film. A similar behavior can be found for annealing lines written at different laser power, where the increasing line width with increasing power can also be observed in the Raman spectra.

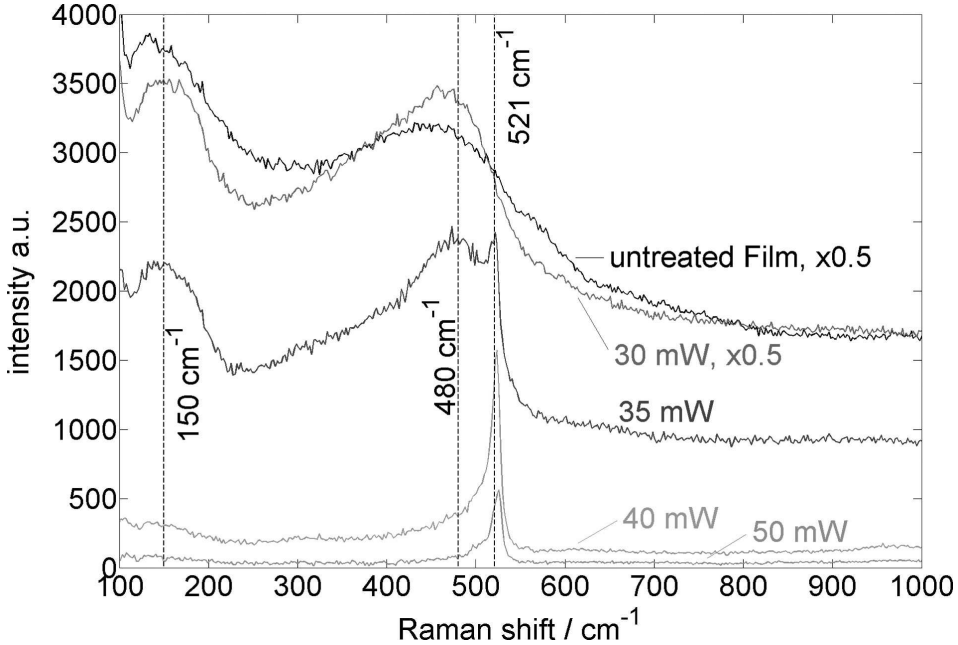


Figure 2.3: Raman spectra of laser annealed lines in SiO_x irradiated with varying laser power. All spectra are recorded from the center of the annealing lines. The black line represents the Raman spectrum of the untreated SiO_x film.

To characterize roughness and topography of the laser annealed lines, SEM and AFM images are recorded from the surface area. Employing SEM on the lines written at $1.4 \times 10^5 \text{ W/cm}^2$ and below shows that an identification of the line area is not feasible and indicates that the surface structure remains completely unchanged. AFM analysis, however, reveals that the material is slightly swelling during irradiation, with, for example, a height of 30 nm for the $1.2 \times 10^5 \text{ W/cm}^2$ line and a height of 40 nm for the $1.4 \times 10^5 \text{ W/cm}^2$ line (Fig. 2.5). The width of the bulge corresponds to the width of the luminescent area (cf. Fig. 2.2). In the topography of the stronger lines, a slight central dip can be observed. For the lines written at an irradiance of $1.4 \times 10^5 \text{ W/cm}^2$ and below, an evaluation of the AFM measurements yields a surface roughness of $R_q \approx 1 \text{ nm}$. This value also holds for the untreated SiO_x film, thus revealing that surface roughness is not increased by the annealing process. TEM inspection of cross-section samples revealed a typical microstructure of the laser irradiated regions. For irradiances at $1.2 \times 10^5 \text{ W/cm}^2$ and above a damaged layer is found in the center of the irradiated lines followed by a region containing silicon nanocrystals (nc-Si). Typical con-

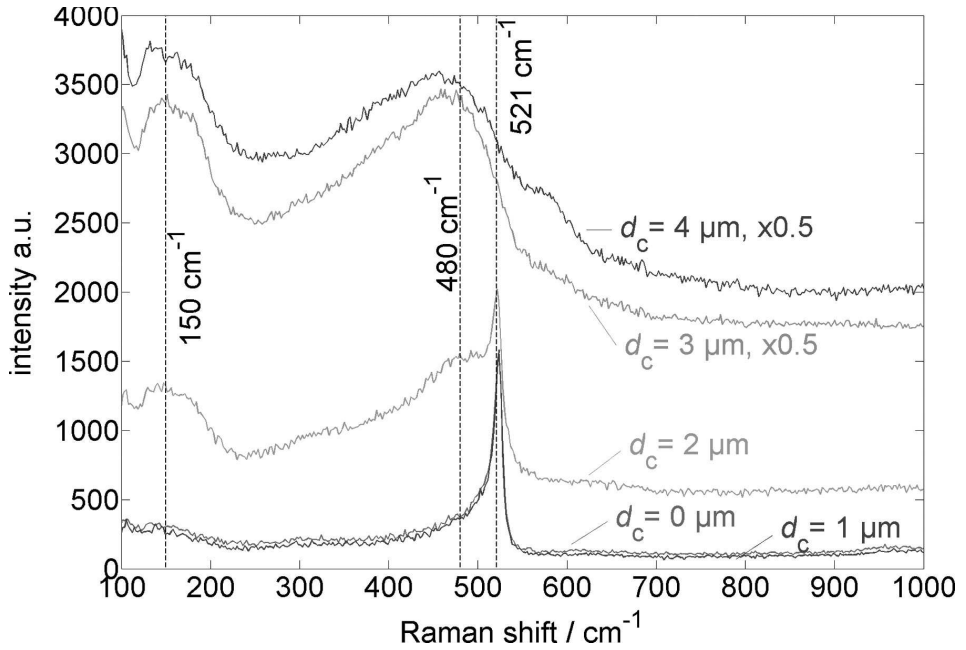


Figure 2.4: Raman spectra recorded at increasing distance d_c to the center of a laser annealed line in SiO_x that has been irradiated with $1.4 \times 10^5 \text{ W/cm}^2$ (40 mW).

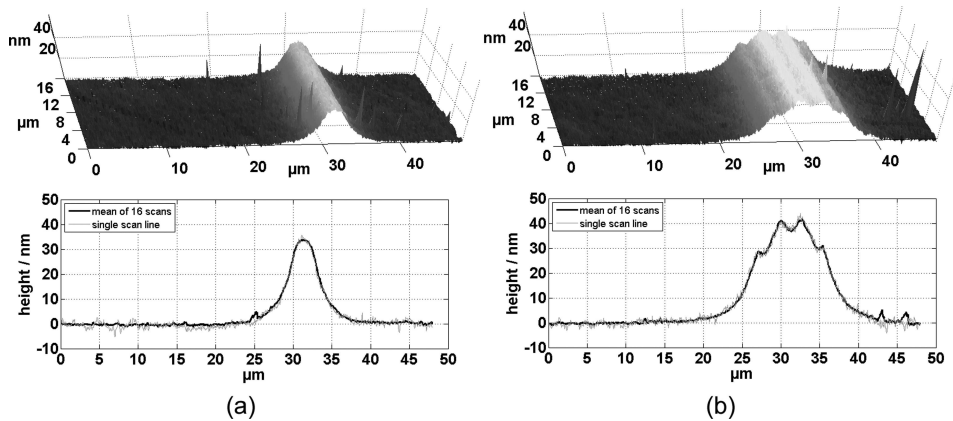


Figure 2.5: Surface topography of laser annealed lines (AFM measurement) in 3D representation (top) and line profile plot (bottom). During annealing, an irradiance of $1.2 \times 10^5 \text{ W/cm}^2$ (35 mW) (a) and $1.4 \times 10^5 \text{ W/cm}^2$ (40 mW) (b) has been used.

cal dark-field images from the sample irradiated at $1.2 \times 10^5 \text{ W/cm}^2$ are displayed in Fig. 2.6(a) which is a low-magnification overview showing the main features. Enlarged details shown in Fig. 2.6(b)-(d) provide evidence that a damaged layer forms just below the surface at this laser power (see double arrow in Fig. 2.6(b)) which contains small cavities as indicated by the dark circular contrast marked by the arrow. The porous nature of this damaged layer is unambiguously revealed by high-angle annular dark-field imaging and even more convincing from energy dispersive x-ray spectrometry (EDX) not shown here. Fig. 2.6(c) and (d) have been

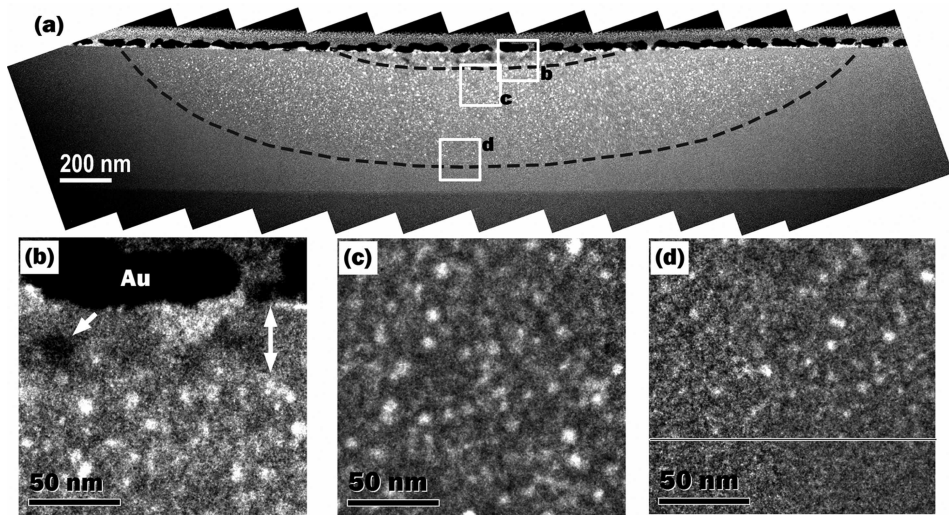


Figure 2.6: Conical dark-field images of a cross-section obtained from the sample irradiated at $1.2 \times 10^5 \text{ W/cm}^2$ (35 mW). (a) is a low-magnification overview, composed from a series of images with a shifted field of view, that allows distinguishing regions, i.e. from bottom to top: SiO_2 substrate, SiO_x without nc-Si, SiO_x containing nc-Si (between the dashed lines) and a damaged region in the center indicated by the upper dashed line. White squares with letters indicate regions shown in more detail in (b)-(d): the central part (b) shows damaged layer (double arrow) and a cavity (arrow). The central region contains larger nc-Si particles (c) compared to the regions at the border (the latter is indicated by the line in (d)).

obtained from the top and bottom part of the nc-Si containing region, respectively. The conical dark-field images show small nanocrystals as bright spots of various sizes. It is easy to see that nanocrystals in the center region tend to be larger compared to those at the border to SiO_x regions (see also Fig. 2.8). It should be noted that no nc-Si particles as well as no damaged surface region have been observed in cross-section TEM samples after laser irradiation at $1.0 \times 10^5 \text{ W/cm}^2$

and $0.9 \times 10^5 \text{ W/cm}^2$.

Fig. 2.7 is a high-resolution TEM image showing crystalline particles (dashed circles) in an amorphous matrix. The particles give rise to bright contrasts in the conical dark-field images and allow identifying their crystal structure as that of diamond-cubic (dc) silicon. The latter is documented by the diffractogram shown as an inset and its indexing according to dc silicon.

Comparison of Fig. 2.6(c) and (d) already indicated that larger nc-Si particles form in the center of the irradiated lines compared to those formed close to the border of nc-Si containing region. Figure 2.8 shows this in a more quantitative way by comparing size distributions obtained in the center (filled bars) and at the edges (open bars). It is clearly seen that the distribution representing the central region contains substantially more particles with sizes above a diameter of 8 nm. Finally, let us focus on the main properties of the damaged layer forming in the center of irradiated lines for laser powers above $1.2 \times 10^5 \text{ W/cm}^2$. As mentioned above, these layers are porous amorphous material with according to EDX a composition close to SiO_2 indicating oxidation to take place during laser treatment. Fig. 2.9 compares the porous layer for different laser powers showing a strong decrease of the layer thickness with decreasing power; we note here that no damage was observed in samples irradiated at $1.0 \times 10^5 \text{ W/cm}^2$ and $0.9 \times 10^5 \text{ W/cm}^2$ indicating that a threshold for porous layer formation can be found between 1.0 and $1.2 \times 10^5 \text{ W/cm}^2$. Fig. 2.9 also shows a substantially reduced density of nc-Si particles in the porous layer compared to the undamaged but decomposed regions.

2.4 Discussion

From the corresponding Raman spectrum with a broad band around 450 cm^{-1} , it can be concluded that elemental silicon is already present in the as-prepared and untreated SiO_x film. Similar spectra can be observed from most silicon-rich silicon oxide films that are prepared by different thin film deposition technologies. The source and mechanism of the slight PL from these films in the green-red spectral region is still subject to debate but generally attributed to oxygen related defects [138][141][142]. When irradiating the SiO_x film by the focused laser beam, local

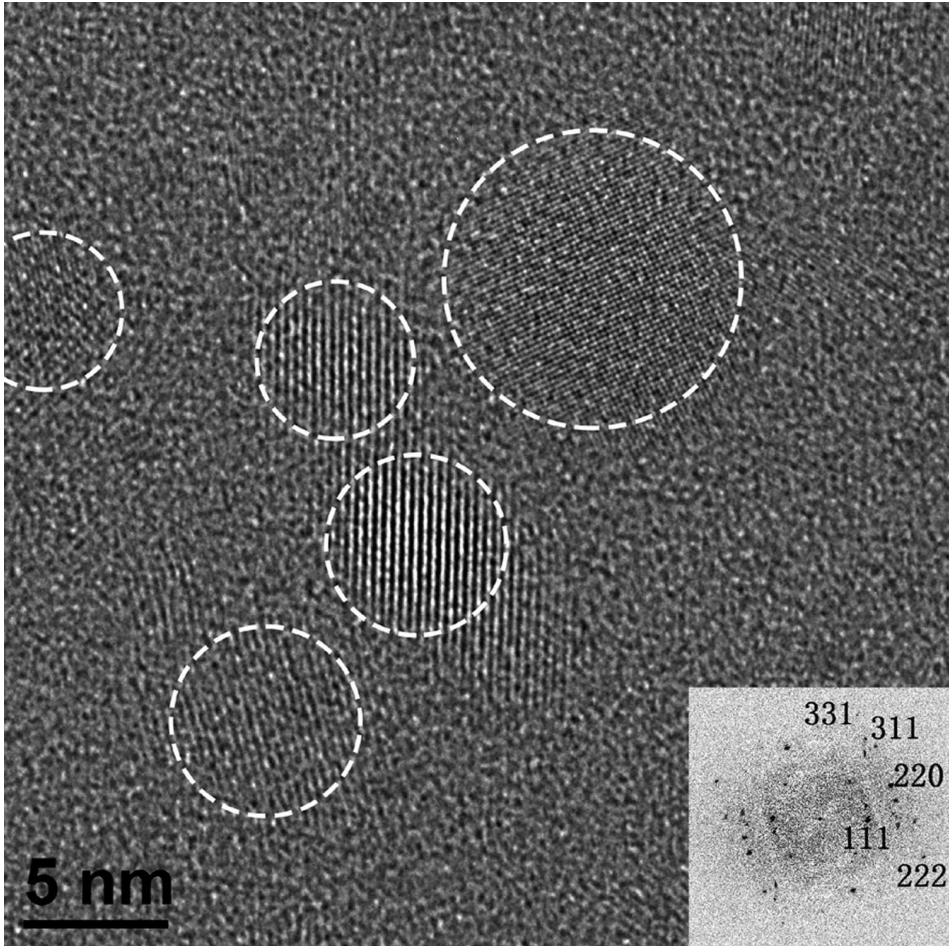


Figure 2.7: High-resolution TEM image showing crystalline particles (dashed circles) embedded in an amorphous matrix obtained for laser irradiation at $1.4 \times 10^5 \text{ W/cm}^2$ (40 mW). The inset shows a diffractogram of the image with spots indexed according to diamond-cubic silicon. Lattice fringe spacings do not significantly differ from values expected for bulk silicon.

annealing starts at an irradiance of $0.5 \times 10^5 \text{ W/cm}^2$. The beginning phase separation can be observed by a change of refractive index and a strongly increased, red-shifted luminescence. However, no significant change in the Raman signal can be observed below an irradiance of $0.9 \times 10^5 \text{ W/cm}^2$. A comparable behavior is found in the literature for furnace annealing of SiO_x when heated to a temperature of 400-600 °C. In this case, the structural changes are identified as the formation of oxide isolated Si rings where the bond rearrangement is accompa-

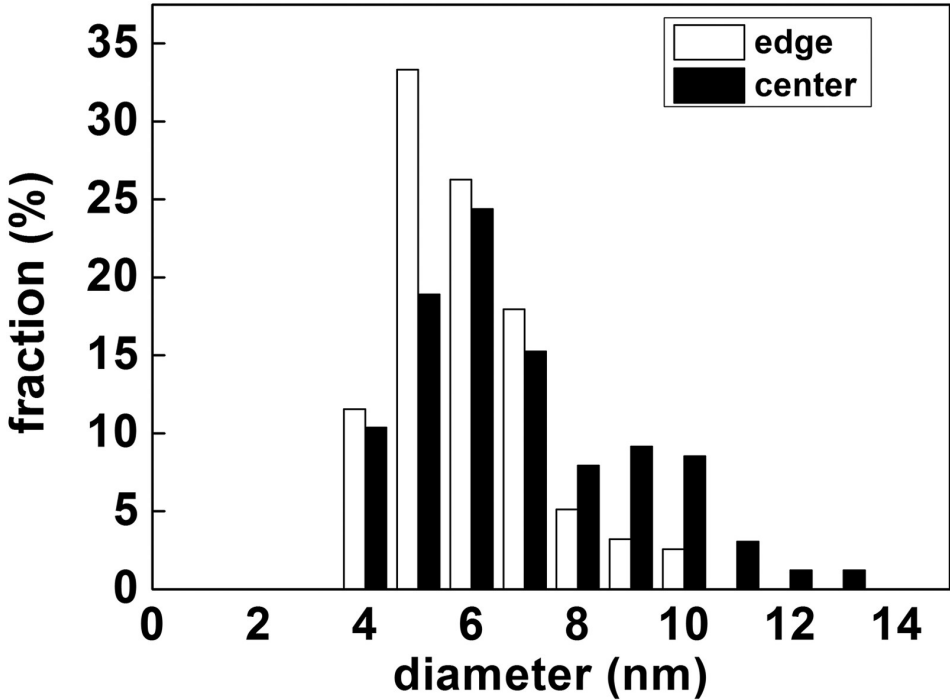


Figure 2.8: Size distribution functions of nc-Si in amorphous silicon oxide after laser irradiation at $1.4 \times 10^5 \text{ W/cm}^2$ (40 mW) obtained from the center (filled bars) and edge (open bars) of the nc-Si particle containing regions. It should be noted that a pronounced shift to higher diameters for the central region is observed.

nied by an increase of defects [131]. In our experiments, the AFM measurements reveal, that this process is also accompanied by a slight swelling of the film material. The formation of amorphous silicon clusters, which is usually obtained in furnace annealing processes at temperatures above $600 \text{ }^\circ\text{C}$, is observed from the Raman spectra of lines irradiated above $1.0 \times 10^5 \text{ W/cm}^2$. Crystallization, usually observed above $900 \text{ }^\circ\text{C}$, starts at a laser power around $1.2 \times 10^5 \text{ W/cm}^2$ but is restricted to the center of the annealing line. The strongly reduced luminescence background and the absence of other features except from the sharp c-Si peak in the Raman spectra suggests, that the phase separation in the center is completed above $1.4 \times 10^5 \text{ W/cm}^2$ irradiance. In contrast to results that were obtained by pulsed laser annealing using UV ps-pulses,16 no significant shift of the c-Si peak compared to bulk c-Si is observed here, thus implying the absence of strong compressive stress on the nc-Si [143].

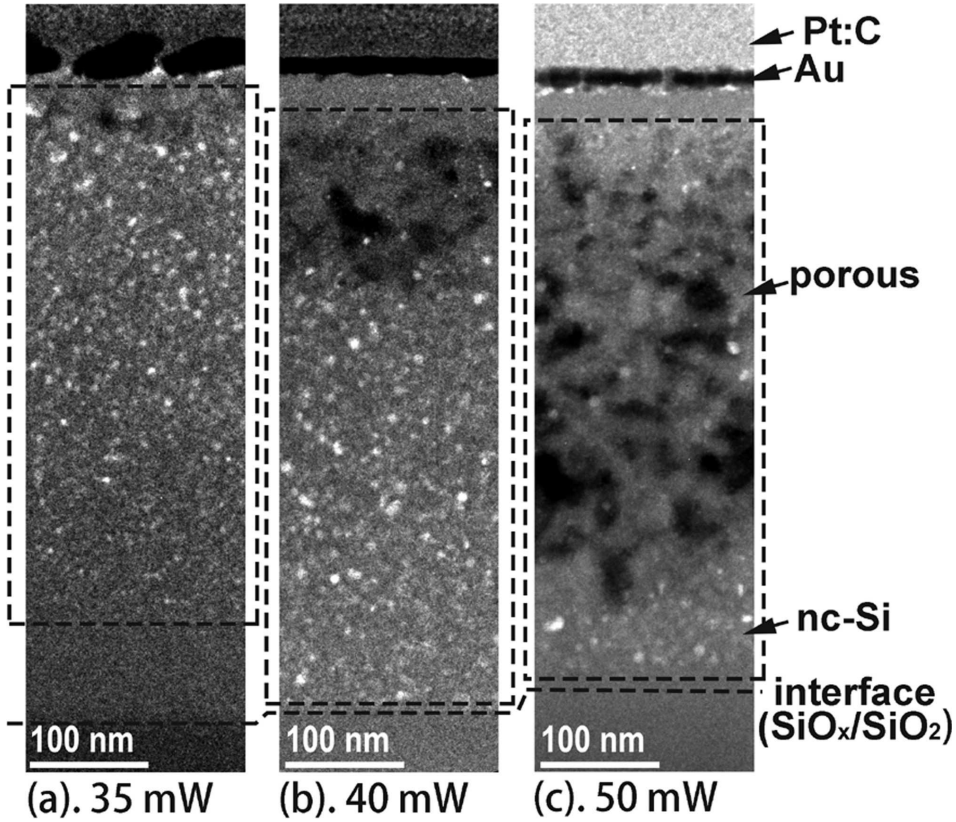


Figure 2.9: Conical dark-field images taken at the center of irradiated lines for (a) $1.2 \times 10^5 \text{ W/cm}^2$ (35 mW), (b) $1.4 \times 10^5 \text{ W/cm}^2$ (40 mW) and (c) $1.75 \times 10^5 \text{ W/cm}^2$ (50 mW). The most prominent feature is the decreasing thickness of the porous layer with decreasing laser power. For $1.75 \times 10^5 \text{ W/cm}^2$ it almost extends down to the SiO_2 substrate whereas a thickness of only 50 nm is obtained for $1.2 \times 10^5 \text{ W/cm}^2$. Please note that no porous layer formation is observed for laser powers of $1.0 \times 10^5 \text{ W/cm}^2$ and $0.9 \times 10^5 \text{ W/cm}^2$.

The size of the nanocrystalline region coincides in the TEM and Raman measurements, showing a width of $4 \mu\text{m}$ in the case of the line irradiated at $1.4 \times 10^5 \text{ W/cm}^2$, for example. Attached at both sides of the center is a zone with a-Si clusters and a width of approximately $1 \mu\text{m}$. The strongest PL signal is obtained from the edges of the amorphous zone. In the example of the $1.4 \times 10^5 \text{ W/cm}^2$ annealing line, the PL maxima are separated by $7 \mu\text{m}$. The good correspondence between furnace annealing with increasing temperature and laser annealing at increasing irradiance leads to the conclusion, that the effect of the irradiation is purely thermal, where the local temperature is determined by the beam intensity profile and the different

stages of the phase separation process can be traced across the line profile. However, the extremely reduced heating time in the case of laser annealing might be compensated by correspondingly higher temperatures.

From the high density of nanocrystals in the center of the annealing lines at laser powers above $1.2 \times 10^5 \text{ W/cm}^2$, a strong PL signal in the NIR spectral range around 900 nm might be expected. However, a decrease in PL associated with an increase of the nc-Si Raman signal can also be observed employing furnace annealing of SiO_x films [144]. Godefroy et. al. have shown that after annealing of the SiO_x films the PL of nc-Si is dominated and partly quenched by defects localized at the Si/ SiO_2 interface rather than by the quantum confinement of the exciton states [145]. As a further process step, hydrogen passivation can be used to remove the defects, resulting in strong luminescence from quantum confined states [146]. The bleaching that is observed in the center of the annealing lines has also been reported from nc-Si samples that had been prepared from etched porous silicon without passivation [147]. To our knowledge, no explanation on the nature of the trap states has been put forward, yet.

In our experiments, the morphological structure of the annealed SiO_x films is preserved up to a laser power of $1.2 \times 10^5 \text{ W/cm}^2$. While a sub-surface porous region is formed at higher laser power, the surface of the annealed lines is still smooth, as can be confirmed from the AFM measurements. The sub-surface porous material can also be observed by scattering in dark-field light microscopy and partly explains the swelling of the SiO_x films. Chemical analysis using energy-dispersive x-ray spectrometry (EDX) shows a reduced total number of Si-K and O-K counts in this region, thus indicating that the overall density is reduced and the structure is indeed porous. For the $1.75 \times 10^5 \text{ W/cm}^2$ line, the calculation of the ratio of background corrected O-K to Si-K intensities reveals a reduced silicon excess with a stoichiometric O/Si-ratio of $x = 1.6$ in the porous region, compared to $x = 1.1$ for the undamaged film. This observation corresponds to a reduced Si Raman signal in the center of the $1.75 \times 10^5 \text{ W/cm}^2$ line. One possible explanation for the reduced Si excess might be an incomplete prevention of oxidation from the ambient atmosphere by the employed nitrogen purging scheme. Another mechanism causing silicon depletion in the center might be a macroscopic phase separation, i.e. a flux of silicon driven by a strong temperature gradient termed thermodiffusion [139]. In this case, Si must be accumulated with a higher concentration at the edge of the porous region. The basis for this effect might be a higher diffusivity

of excess Si atoms in SiO₂ compared to the self-diffusion in stoichiometric oxide [148][149]. A third option might be SiO evaporation, fostered by an overheating of strongly absorbing nc-Si in the region where it first separates. Based on the present data, we cannot decide on the dominant mechanism. Yet, it should be pointed out that a slight dip is observed in the center of the surface profile of the annealing lines irradiated at laser powers of $1.75 \times 10^5 \text{W/cm}^2$ and above.

The varying size distribution of the nc-Si particles from lines irradiated with different laser power and also within a single line suggests that a control of particle size within certain limits is possible. The dependence on heating time, controlled by the scanning speed of the laser beam, and multiple irradiations will be subject of further investigations.

2.5 Conclusion

The use of CW laser irradiation at 405 nm for the locally controlled annealing of SiO_x films on SiO₂ substrates has been demonstrated. Compared to prevalent furnace annealing, the main advantage of the laser process is the possibility to induce amorphous or crystalline Si nanoclusters along with selective refractive index variations with high spatial resolution. Furthermore, laser annealing offers the possibility to generate Si nanoparticles in a fast, high throughput process. Also, the thermal load on the substrate can be significantly reduced.

In this work, we have demonstrated that laser annealing and silicon nanocrystal generation can be accomplished in a substrate bound film without any damage to the film structure. The intact structure of the film matrix surrounding the Si nanoparticles is a prerequisite in many possible applications like modulators and waveguide based applications.

2.6 Acknowledgements

We thank B. Schmidt from the Experimental and Applied Mineralogy department at the University of G"ottingen for making the Raman microscope available.

3 Microstructural analysis of the modifications in substrate-bound silicon-rich silicon oxide induced by continuous wave laser irradiation

Nan Wang,¹⁾ Thomas Fricke-Begemann,²⁾ Patrick Peretzki,¹⁾ Karsten Thiel,³⁾ Jürgen Ihlemann,²⁾ Michael Seibt¹⁾

1) IV. Physikalisches Institut, Universität Göttingen, Friedrich-Hund-Platz 1, 37077 Göttingen, Germany

2) Laser-Laboratorium Göttingen, Hans-Adolf-Krebs-Weg 1, 37077 Göttingen, Germany

3) Fraunhofer Institut für Fertigungstechnik und Angewandte Materialforschung, 28359 Bremen, Germany

<https://doi.org/10.1016/j.jallcom.2016.12.115>

Laser-irradiation of silicon-rich silicon oxides (SRSO) is a promising technique for spatially well-defined production of silicon nanocrystals (nc-Si) showing room temperature photoluminescence. In this work, we use continuous-wave (CW) laser processing to generate nc-Si in SRSO films on fused silica substrates. One main problem is damage introduced by laser processing which results in a porous layer beneath the original film surface as is consistently shown by electron tomography and energy-dispersive X-ray spectrometry. Processing conditions for damage-free nc-Si formation are identified by systematic variation of laser intensity and measuring the depth of the damaged region by transmission electron microscopy (TEM). By combining TEM imaging and analysis it is shown that the damaged region has a composition close to SiO₂ which is due to a predominant loss of silicon rather than an a result of surface oxidation during laser processing.

3.1 Introduction

Low-dimensional silicon system show room-temperature photoluminescence due to quantum confinement [4]. One possible route to Si nanostructures with potential applications for light-emitting devices are silicon nanocrystals (nc-Si) embedded in SiO₂. Such structures can be generated from substoichiometric SiO_x with $x < 2$ which is subsequently referred to as silicon-rich silicon oxide (SRSO). Such oxides exhibit a phase transformation into nanocrystalline silicon (nc-Si) and stable SiO₂ upon high-temperature thermal annealing [128][131]. Laser irradiation instead of thermal annealing potentially allows for spatially well-controlled nc-Si formation [89]. However, local energy deposition by laser irradiation inevitably suffers from heat loss due to substantial temperature gradients especially in the case of substrate-bound SRSO films necessary for technical applications [85]. This will require high laser intensities and allow only a narrow process window for efficient generation of nc-Si without damage or ablation of the film. Phase separation using pulsed excimer lasers seems to be possible, but crystalline Si is only obtained at fluences exceeding the damage threshold [71][150][115]. For the case of substrate bound films and cw laser annealing it has been thought, that the local temperature is not sufficiently high in order to induce the phase separation of SRSO into nc-Si and SiO₂. Hence, focus has been on laser irradiation of free-standing SRSO films in previous studies mainly performed by Khriachtchev and co-workers [85][121][74]. In a recent study [89], we have demonstrated for substrate-bound SRSO films that conditions of CW laser irradiation can be adjusted such that Si structures showing strong photoluminescence (PL) can be formed while avoiding surface damage due to laser irradiation. At higher laser intensity, however, laser-treated SRSO shows pronounced damage reducing the PL yield.

In this paper, we report microstructural investigations of CW laser irradiated SRSO thin films on SiO₂ substrates. Systematic variation of the laser intensity reveals a threshold for damage formation. Using mainly transmission electron microscopy (TEM) techniques such as hollow-cone dark field imaging, energy-dispersive x-ray spectrometry (EDX) and scanning TEM high-angle annular dark field (STEM-HAADF) tomography we put special emphasize on the structure and composition of the damaged region. It is shown that the latter consists of porous material with a composition close to SiO₂ which is related to a loss of (mainly) silicon material in the damaged region rather than due to a possible oxidation as a result of residual oxygen of the nominally inert ambient and possible mechanisms

are discussed. In addition, combining atomic force microscopy (AFM) with TEM cross-section imaging, we can separate apparent deformations of the SRSO film and of the underlying SiO₂ substrate.

3.2 Materials system and Experimental

SRSO films have been ion beam sputtered on 2 mm thick fused silica substrates provided by a commercial coating supplier (Laseroptik, Garbsen, Germany). In this process, silicon is used as a target and oxygen gas is supplied to tune the stoichiometry of SRSO films. SRSO films used here are 545nm thick (confirmed by cross-section TEM) and show a transmission of 15% at 405 nm wavelength. A diode laser with continuous wave emission at 405 nm (Coherent Cube) is focused by a 10x microscope objective onto the SRSO layer for spatially resolved laser irradiation. The laser beam intensity is close to a Gaussian profile and the focus spot is evaluated to be 6 μm . During laser irradiation, samples are enclosed in a small housing that is purged with a steady flow of nitrogen in order to prevent oxidation during annealing. Irradiation is then accomplished through a 1 mm thick fused silica window. The position of the sample is controlled accurately by high precision positioning stages. Line-shaped irradiated areas are obtained by moving the samples at a speed of 300 $\mu\text{m}/\text{s}$. The laser intensity is varied from 1.4×10^5 to 1.75×10^5 W/cm². Focused ion beam (FIB, FEI Nova NanoLab 600) is employed to prepare cross-sectional TEM samples centered on the irradiated lines and oriented perpendicular to the direction of the irradiated lines. Prior to FIB preparation of TEM lamella, a thin Au layer (5 nm) is evaporated on the samples in order to avoid charging in FIB environment during SEM inspection. Electron transparent lamellas were prepared using a Ga ion beam focused to about 7nm and final thinning at beam voltage of 5kV. TEM analyses have been performed at 200 kV in a Philips CM200 FEG-UT. HRTEM and hollow cone dark field imaging is done to explore the microstructure of irradiated samples. In order to study the chemical composition, we use energy-dispersive x-ray spectrometry (EDX). STEM-HAADF imaging is used for tomography which is done in a FEI Tecnai TF20 STWIN at 200kV equipped with an Advanced Tomography Holder Fischione Model 2020) in order to characterize the detailed microstructure of damaged region.

3.3 Results and Discussion

3.3.1 Damage-Free CW Laser Irradiation

In the previous study [89], we have shown that three structurally distinct regions are observed, i.e. a damaged (porous) region, a nc-Si region (region containing nc-Si) and SRSO as indicated in Fig. 1 which compares the central part of irradiated samples after irradiation with different laser powers. It should be noted that no damage is observed in samples irradiated at 1.05×10^5 and $0.88 \times 10^5 \text{ W/cm}^2$. The sample irradiated at $1.22 \times 10^5 \text{ W/cm}^2$ shows a very thin damaged region at the top and also seemingly unreacted SRSO between the nc-Si region and the fused silica substrate (compare Fig. 3.1(a)). It should be noted, that the damaged regions contain a small number of nc-Si (compare white dot-like contrasts in Fig. 3.1(b) and 3.1(c)) indicating that the phase separation of SRSO into nc-Si and SiO_2 occurred in the damaged region to some extent and some nc-Si survived damage formation. In order to explore the existence of a threshold power for laser induced damage formation the central thickness of the damaged region (d_{porous}) is measured by means of cross-section TEM and summarized in Fig. 3.2. It can be seen that from 1.75×10^5 to $1.22 \times 10^5 \text{ W/cm}^2$, d_{porous} decreases linearly. Extrapolating to $d_{\text{porous}}=0$ a threshold is observed at a laser power of about $1.16 \times 10^5 \text{ W/cm}^2$ below which no damage occurs. It implies that a really damage-free CW laser irradiation for SRSO films is possible with careful control of laser power. We note here that samples below the threshold show strong photoluminescence at room temperature as has been reported in detail in [89].

3.3.2 Surface Topography and Layer Thickness

We now address the surface morphology and its relation to the SRSO layer thickness after laser irradiation. As we have already shown in [89], atomic force microscopy (AFM) data reveal a swelling of laser irradiated SRSO as is shown in Fig.3(a) (red curve, left scale) for an irradiance of $1.4 \times 10^5 \text{ W/cm}^2$. Using the untreated area far away from the line as a reference, a typical maximum surface height of 42 nm is obtained. This region is about $1.3 \mu\text{m}$ outside the center of the written line where the surface is at about 38nm. Complementary information is provided by TEM in cross-section geometry taken in the hollow-cone dark-field imaging

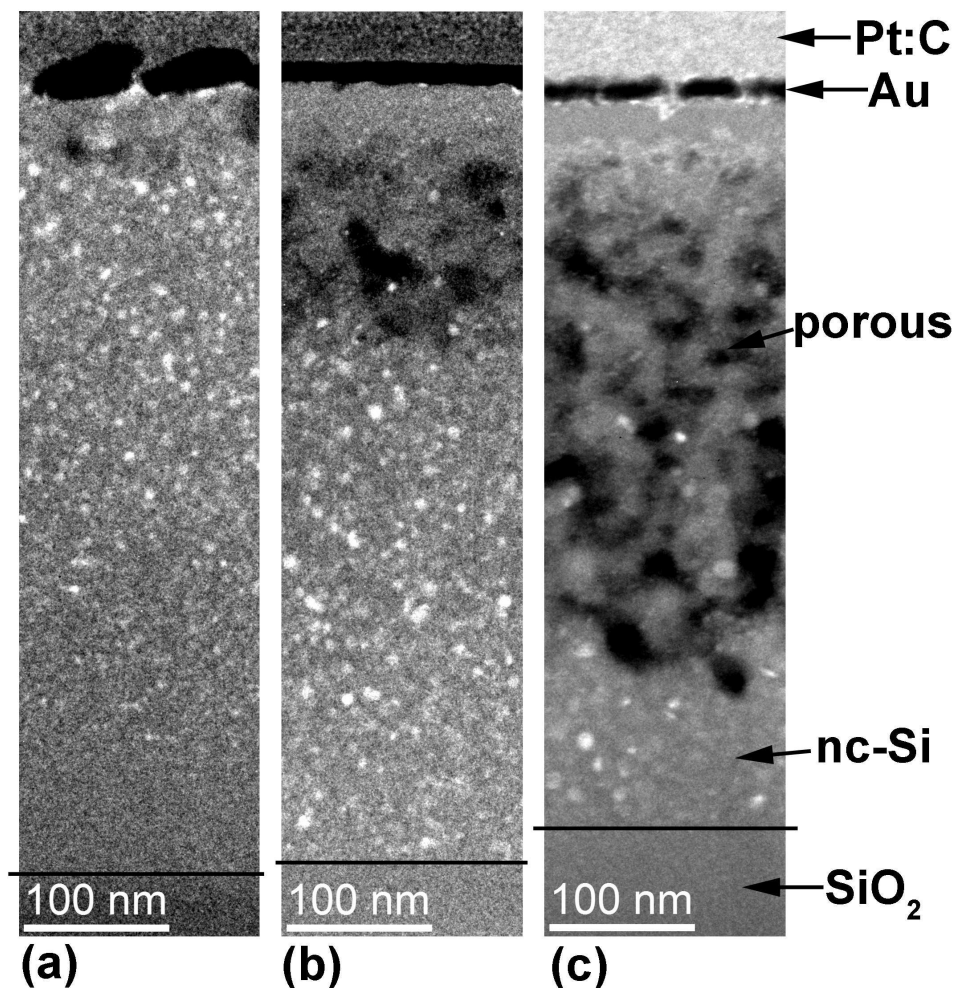


Figure 3.1: Conical dark-field images taken at the center of irradiated lines for (a) $1.22 \times 10^5 \text{ W/cm}^2$, (b) $1.4 \times 10^5 \text{ W/cm}^2$, and (c) $1.75 \times 10^5 \text{ W/cm}^2$. Three different regions can be distinguished, i.e. a damaged region (black dark contrasts indicate pores in the material), the nc-Si region containing nc-Si particles (bright spot-like contrasts), and - for the sample in (a) - a SRSO region between the nc-Si region and the interface to the substrate. No damage is observed in samples irradiated at less than $1.05 \times 10^5 \text{ W/cm}^2$. It is interesting to note that a small number of nc-Si particles are observed in the porous region.

mode (Fig. 3.3(b)). Using the interface position between the SRSO layer and the fused silica substrate as a reference, the local thickness d of the laser treated SRSO film can be measured (see Fig. 3.3(a), black curve and right scale), Fig.

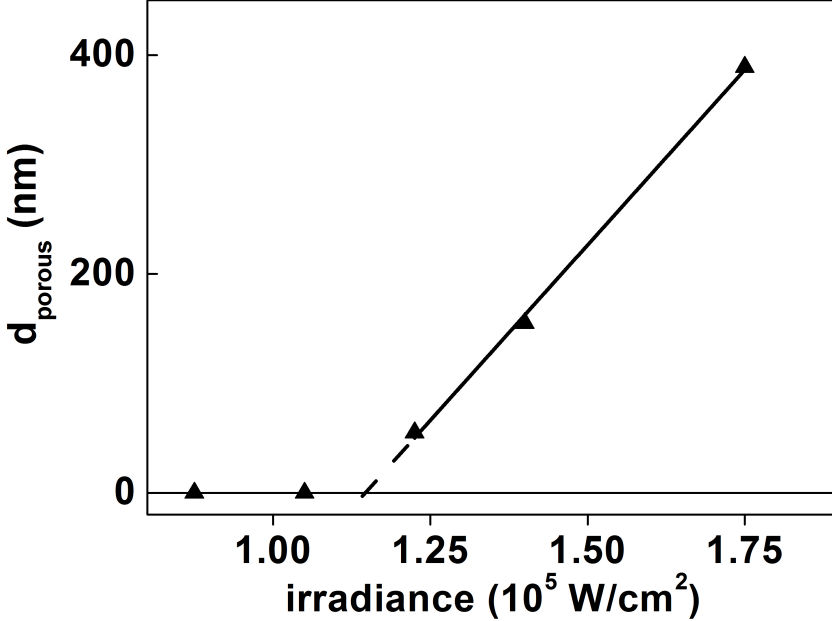


Figure 3.2: Depth d_{porous} of the damaged region vs. laser intensity. The depth was measured in the center of the irradiated lines using cross-section TEM. Experimentally, we find a linear increase of d_{porous} with laser intensity as indicated by the fit (solid line). Extrapolation (dashed line) yields a threshold for damage formation of $1.15 \times 10^5 \text{ W/cm}^2$. In fact, samples irradiated at 1.05×10^5 and $0.88 \times 10^5 \text{ W/cm}^2$ do not show the damaged region but still a strong room temperature PL signal [89].

3.3(c) shows details of magnified stripes taken at the positions indicated in Fig. 3.3(b) by numbers. The stripes have been aligned at the layer-substrate interface and a central 400nm high part has been removed in order to simultaneously view the interface and surface at sufficient magnification. The horizontal lines in Fig. 3.3(c) indicate the position of the interface (bottom line) and the thickness of the untreated SRSO film (top line) as measured from a TEM cross-section prepared in an untreated region. It is clearly seen that the surface is above the reference position in stripes 3 and 4 which qualitatively agrees with AFM data (Fig.3(a)). In stripes 0 and 1, however, the surface is considerably below the reference line. Combining AFM and TEM it has to be concluded that a considerable part of the swelling revealed by AFM is due to the silica substrate. A similar surface swelling has been observed in the case of laser-writing waveguides in the near-surface vol-

ume of fused silica [151]. This process, however, has been performed with a high repetition rate femtosecond laser, but like in our case strong local heating along the written line is assumed. In summary, both techniques (AFM and TEM) consistently show a volume increase of the SRSO due to laser irradiation. Taking into account previous work we may conclude that the elevated rim of the laser treated area is connected to compressive stress caused by nc-Si particles as has been concluded from Raman results on free-standing SRSO films [142][152]. In addition, TEM provides evidence that - as part of damage formation - material has been removed from the central part of the irradiated regions. We note here, the amount of removed material does not account the thicker layer in the outer region. Hence, flow of material from the centre to the edge driven by a temperature gradient as proposed previously [85] is not supported by our data.

3.3.3 Microstructure of Damaged Region

We now address the microstructure and chemical composition of the damaged region. Chemical analysis using EDX for the sample irradiated at 1.75×10^5 W/cm² is summarized in Fig. 3.4. The bright-field STEM image (Fig. 3.4(a)) again shows the three main regions, i.e. (1) the SiO₂ substrate, (2) the nc-Si region, i.e. the SRSO layer containing nc-Si, and (3) the damaged region. The background-corrected total numbers of O-K and Si-K counts measured by EDX are shown in Fig. 3.4(b) and 3.4(d), respectively. It is obvious, that material has been removed from region (3) as is concluded from the simultaneous loss of mainly silicon but also of some oxygen. Furthermore, 50-100nm large regions - bright areas in the STEM image - of reduced O-K and Si-K counts show the cavities constituting the porous microstructure of the damaged region. Further evidence of the porosity is provided by STEM high-angle annular dark field (HAADF) tomography. An animated video of a reconstructed tilt series obtained for the sample irradiated at 1.75×10^5 W/cm² is found as supplemental material of this paper. Fig.5 collects STEM-HAADF images for different viewing angles exemplarily showing two larger cavities in addition to a higher density of small holes indicated by the contrast variations in the damaged region. Hence, the combination of EDX mapping and tomography provides evidence for porous character of the damaged region.

Returning to the chemical maps in Fig. 3.4 we note the following results: (i) the oxygen content in region (2) is about 10% below that in the silica substrate whereas

the silicon content of region (2) exceeds that of region (1) by approximately 40%, and (ii) the oxygen-to-silicon ratio x obtained from background-corrected EDX maps (Fig. 3.4(b)) of the damaged region is quite close to that of the SiO_2 substrate and distinctly larger than in region (2) where $x=1.32$ is measured. Despite the fact that we employ N_2 as ambient atmosphere to avoid oxidation during laser irradiation, one might attribute this result to surface oxidation during laser irradiation due to residual oxygen in the ambient. However, comparing the damaged region and the nc-Si region in Fig. 3.4(d) reveals that Si-K counts in the damaged region are roughly half of that in nc-Si region while the O-K counts are only slightly smaller than that in the nc-Si region. Thus, considering the reduced Si-K counts in the porous region after laser irradiation, we may conclude that the composition of the damaged region of close to SiO_2 is due to a predominant loss of silicon material rather than a true oxidation. Clearly, it is not possible to identify the underlying scenario of this silicon depletion from the presented data alone. We may, however, discuss possible mechanisms, one of which is a macroscopic chemical separation driven by a strong temperature gradient, i.e. thermodiffusion, as has been proposed previously [85]. The required selectivity for silicon might be attributed to higher diffusivity of excess Si atoms in SiO_2 compared to the self-diffusion in stoichiometric oxide [148][149]. We note, that in this case, silicon should accumulate at the edge of the porous region which is not confirmed by our data. Another scenario is the predominant evaporation of SiO and nc-Si in the course of the laser-driven nanoscopic phase separation process. We may speculate that silicon nanocrystals once being formed more strongly absorb the light compared to unreacted SiO and formed SiO_2 leading to local overheating and selective ablation of Si-rich regions leaving a sponge-like network of SiO_2 behind. In this scenario, nanoscopic phase separation of SRSO into nc-Si and SiO_2 are consecutive processes which is consistent with the existence of a critical irradiance for damage formation (see Fig. 3.2).

3.4 Summary and Conclusion

In this work, we have studied the microstructure of amorphous silicon rich silicon oxide films on fused silica substrates produced by CW laser irradiation. A systematic variation of the laser intensity has identified a threshold below which no damage is observed; under such conditions, strong room temperature luminescence

is observed as reported previously [69]. TEM imaging and analysis has shown that the damaged region has a porous character with cavities as large as 100 nm and a network of material whose composition is close to that of fused silica. Furthermore, only a few silicon nanocrystals are observed in damaged regions. Both observations are consistent with a predominant loss of the silicon from the central part of the irradiated area possibly due to ablation. A combination of AFM and TEM furthermore indicates that a substantial fraction of the elevated surface profile seen by AFM is due to deformation of the underlying substrate whereas the material loss mentioned above is reflected by a decrease in the silicon rich silicon oxide film thickness. This interesting phenomenon needs further investigations in order to distinguish between local deformation or swelling of the involved film and substrate.

3.5 Acknowledgment

The authors acknowledge financial support from the Campus Laboratory and User Facility for Electron Microscopy (CLUE) at Georg-August-University Göttingen. NW is grateful for support through a CSC scholarship.

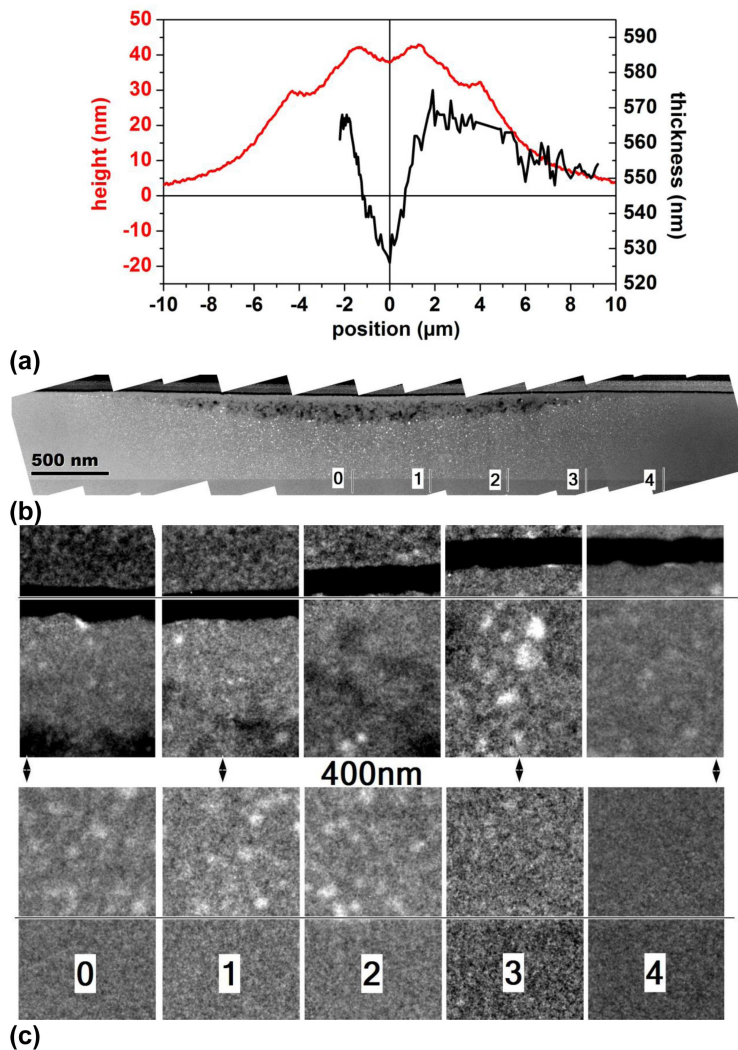


Figure 3.3: Surface topography and layer thickness of a line written with an irradiance of 1.5×10^5 . (a) AFM surface profile (red curve, right scale) and thickness of the SRSO film measured by cross-section TEM (black curve, right scale); the plots have been aligned such that AFM height measured far from the written line ('0' on left scale) coincides with the thickness of an untreated SRSO film (545nm) measured by TEM. (b) Hollow cone dark field image of a cross-section through the irradiated line showing positions 0 to 4 where magnified stripes have been extracted which are shown in (c); please note, that the indicated number multiplied by $0.5 \mu\text{m}$ provides the distance from the center of the line. (c)

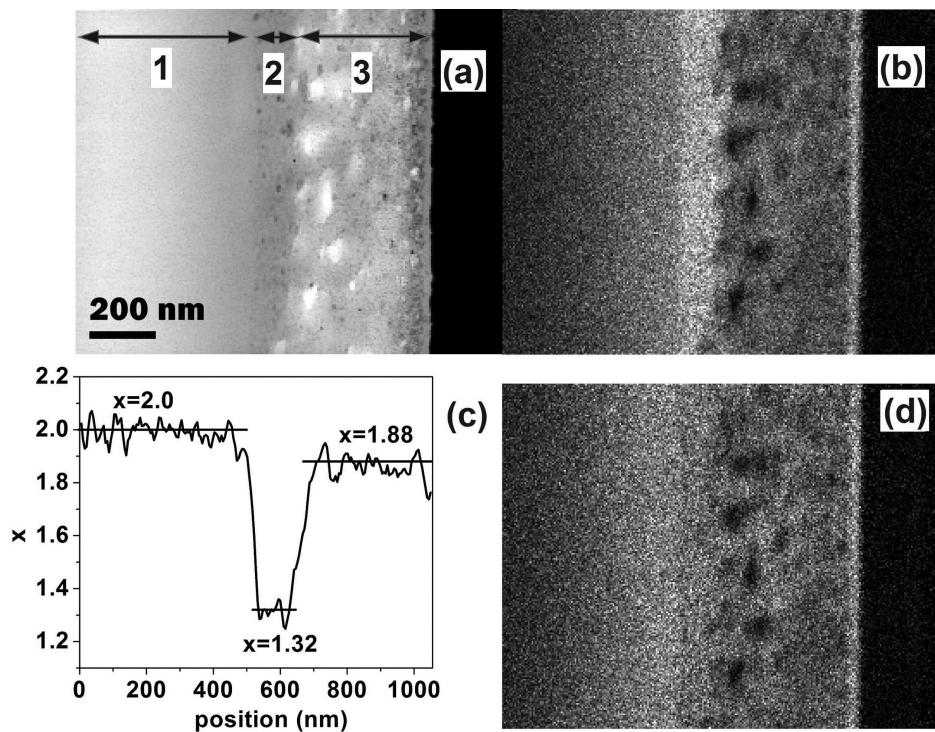


Figure 3.4: Compositional analysis in the center of the annealing line irradiated at 1.75×10^5 W/cm². (a) STEM bright field image showing (1) the SiO₂ substrate, (2) the undamaged nc-Si region, and (3) the porous surface layer. Background-corrected EDX maps of the K-line counts of oxygen (b) and silicon (d) showing the - compared to region (2) - simultaneous loss of oxygen and silicon in region (3) which is consistent with the porous nature of the damaged layer. It is interesting to note that the oxygen content in the SiO₂ substrate (region (1)) exceeds that in region (2) by less than 10% whereas the silicon content in region (2) exceeds that in the substrate by about 40%. (b) Compositional profile measured across regions (1) to (3) expressed as the oxygen-to-silicon ratio x (as in SiO _{x}). Experimental data have been calibrated in region (1) (SiO₂ substrate with $x=2$); region (2) reveals $x=1.32$ whereas $x=1.88$ in region (3) which is close to the stable SiO₂ phase (relative error of x is 15%). Hence, these data show a predominant loss of silicon in region (3).

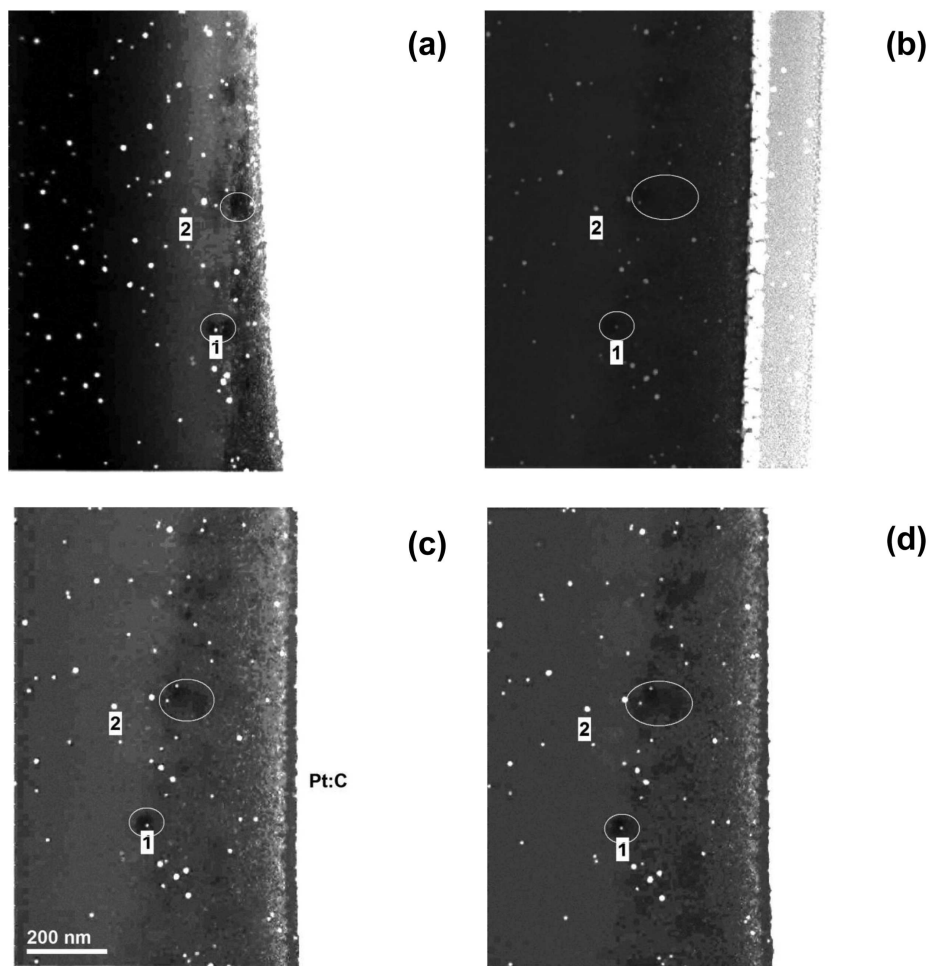


Figure 3.5: STEM-HAADF images along different angles taken from a tomography tilt series (tilt axis approximately vertical); bright spots are due to Au particles used as marker for image alignment (examples '1' and '2' are given in each image). Regions marked by white ellipses indicate larger cavities, while many small pores can be seen in the damaged region. Tilt angles measured from the cross-section orientation shown in (c) are: (a) 68° (b) 18° (c) 0° (d) -9°

4 Formation of porous silicon oxide from substrate-bound silicon rich silicon oxide layers by continuous-wave laser irradiation

Silicon nanocrystals embedded in silicon oxide that show room temperature photoluminescence (PL) have great potential in Si light emission applications. Usually, nc-Si particles can be generated from silicon rich silicon oxide by furnace annealing and laser irradiation. In contrast to furnace annealing, laser irradiation has one unique advantage of spatially controlled heating, which is compatible with modern Si micro-fabrication technology. In this paper, we employ continuous wave laser irradiation to heat substrate-bound SRSO samples and investigate the spatially controlled microstructure by several TEM related techniques like hollow-cone dark field imaging (HCDF), energy-dispersive x-ray spectrometry (EDX) and electron energy loss spectroscopy (EELS). It has been reported that damaged material forms in regions of high laser intensity which quenches room temperature PL. This material exhibits porous character and a composition close to SiO_2 . This work focus on systematical analysis of porous part's microstructure and try to provide a proposed mechanism that describes the formation process. The mechanism is that ripening effect dominates the growth of preformed nc-Si particle and then the escape of the large nc-Si particle goes rise to the formation of sponge-like SiO_2 network. The composition difference in three typical Regions of porous part is also discussed and the extent of nc-Si depletion process is suggested to understand this problem.

4.1 Introduction

Room temperature photoluminescence (PL) was first observed in chemically-etched porous silicon by L. Canham in 1990 [4]. Subsequently, other low-dimensional silicon systems such as silicon nanocrystals (nc-Si), silicon nanowires and silicon nanodots have been shown to produce room temperature PL which has stimulated the development of silicon photonics [153].

In contrast to porous silicon, nc-Si particles embedded in amorphous silica matrix combine room temperature PL [133, 154] with a high thermal stability [84]. They can be produced from the decomposition of silicon-rich silicon oxide (SRSO, also: substoichiometric SiO_x , $x < 2$) by furnace annealing [93, 94, 95], laser annealing [113, 114, 115, 71, 116, 121, 74], or ion bombardment [96]. It has been shown that the precipitation of nc-Si particle from SRSO requires high temperatures (1000-1100°C) [87].

Unlike furnace annealing, laser irradiation can spatially control the formation of nc-Si particles, which provides the advantages of coupling silicon-based light emitting diodes on a single chip [86] and fast processing. It has been shown that sufficiently high temperatures can be obtained by pulsed laser irradiation [113, 114, 115, 71, 116]. However, a typical side-effect of nc-Si particle formation in SRSO films is laser ablation [71]. In other words, the laser intensity used in pulsed laser irradiation typically exceeds the damage threshold.

As an alternative, continuous wave (CW) laser irradiation with intermediate heating effects has shown the potential to generate nc-Si particles without any visible damage at the surface [74] for free-standing SRSO films. In our previous studies, we have succeeded in producing room temperature PL from CW laser irradiated substrate-bound SRSO films under damage-free conditions. In addition, we studied the internal structural modifications occurring at high laser intensity which are responsible for a reduced PL yield [89]. In a further study [72] on such structures we have used transmission electron microscopy (TEM) techniques including electron tomography to show the porous structure of the damaged layers. In contrast to CW laser annealing on silica [79], the treatment of SRSO involves some additional kinetic processes mainly related to the phase separation. Thus, the formation mechanism of the porous structure during laser irradiation needs to be studied in more detail in order approach a more comprehensive understanding of

the phase separation in SRSO.

In this paper, we systematically investigate the microstructure of porous regions formed by CW laser irradiated SRSO films by imaging and analytical TEM techniques. Following the variation of laser intensity in our previous study[72], we focus on the effect of irradiation time on the microstructure in order to get some insight into the temporal evolution of the damage.

Our investigations consistently show that the damaged regions consist of an amorphous matrix with a composition close to SiO_2 containing pores and a low density of crystalline silicon nanoparticles. Increasing the irradiation time increases the depth of the porous regions indicating its evolution from the layer surface. The observation of silicon particles of similar size as the pores has led us to propose the mechanism of 'selective silicon ablation' as a continuation of the phase separation process.

4.2 Experiment

Ion sputtering was employed to deposit SRSO films on 2 mm thick fused silica substrates by a commercial coating supplier (Laseroptik, Garbsen, Germany). The thickness of SRSO was 545 nm as measured by TEM. For irradiation, a continuous wave diode laser with the emission wavelength at 405 nm was focused using a $10\times$ microscope objective to a beam spot of 6 μm . Laser annealing was performed in a chamber with a steady flow of nitrogen to avoid surface oxidation. During laser annealing, high precision positioning stages were used to form line-shaped irradiated regions with the speed of movement varied from 50 to 300 $\mu\text{m/s}$ in order to control the total local irradiation time. The latter is estimated as the beam diameter divided by the velocity of the positioning stage. The laser intensity was tuned from 1.4×10^5 to $1.75\times 10^5 \text{W/cm}^2$. TEM samples in cross-sectional geometry were centered on the irradiated line and prepared by focused ion beam (FIB, FEI Nova NanoLab 600). Please note, that prior to FIB preparation, a thin gold layer (5 nm) was evaporated on samples in order to avoid charging during SEM inspection.

Transmission electron microscopy (TEM) experiments were conducted using a

Philips CM200-UT-FEG microscope operated at 200kV having a point resolution of 0.19nm. We use hollow-cone darkfield (HCDF) imaging based on normal dark field imaging, which employs the incident beam with a fixed tilt angle with respect to the optical axis. The required hollow cone illumination was formed by a beam with a rotation period of 500 ms combined with an exposure time of 5s. Energy-dispersive x-ray spectrometry (EDX) is carried out in scanning transmission electron microscopy (STEM) mode with a probe size of approximately 1 nm using a link ISIS system with a Si-Li detector. Electron energy loss spectroscopy (EELS) measurements were done using a FEI Titan 80-300 G2 ETEM microscope operated at 300 kV and equipped with a Gatan Image Filter (Quantum ER/965 U).

4.3 Results

Fig. 4.1(a) shows the typical situation described in a cross-section HCDF image obtained in the center of the irradiated line-shaped region: starting from the silica substrate at the bottom (labeled 'SiO₂') a layer containing nanocrystalline silicon particles ('nc-Si') has formed followed by a strongly damaged region ('porous') which has been shown to be porous by means of STEM tomography [72].

Here, we focus on the microstructure of the porous layer forming as a result of CW laser irradiation above the critical irradiance which has been determined as $1.15 \times 10^5 \text{W/cm}^2$ in our previous study[72]. Section 4.3.1 deals with structural aspects and shows that the porous layer is amorphous and contains pores as well as a small number of silicon nanoparticles. Comparing the microstructure for different annealing times for the same intensity reveals that the size of pores and silicon nanoparticles is virtually identical in a zone comparing both. Subsequently, Sec. 4.3.2 describes analytical results obtained from energy-dispersive x-ray spectrometry (EDX) and electron energy loss spectroscopy (EELS) which consistently show that the composition of the porous material is close to silicon dioxide, SiO₂. Hence, this layer is depleted of silicon atoms compared to the initial SRSO material.

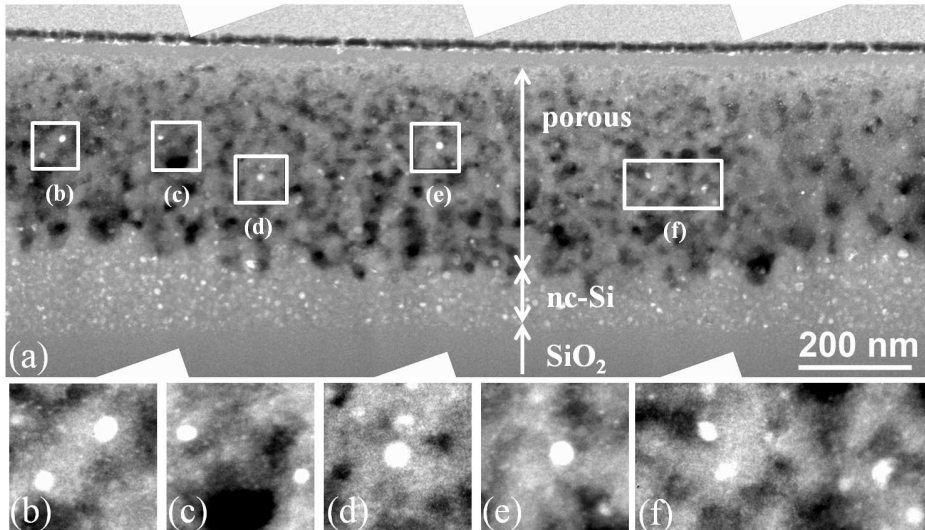


Figure 4.1: (a). HCDF image of the center part of the CW laser irradiated sample with a laser intensity of $1.75 \times 10^5 \text{ W/cm}^2$ and an irradiation time of 20 ms. The porous part shows large dark contrasts on a gray background which stem from pores. In addition, some nc-Si particles appear as bright contrasts which are shown in the magnified images in (b) - (f). In the region between the porous part and the silica substrate smaller nc-Si particles are observed.

4.3.1 Structural properties of the porous silicon oxide

The porous part of the sample displayed in Fig. 4.1 shows predominantly dark contrasts related to pores in the remaining matrix. The latter appears quite homogeneous which is consistent with its amorphous structure. Much smaller bright contrasts in the porous region are due to nc-Si particles which are shown in more detail in Fig. 4.1 (b)-(f). Although the nc-Si region is not in the focus of this paper, we mention that a high density of small nc-Si particles is observed there as bright contrasts.

Such nc-Si particles can be directly imaged as is seen in Fig. 4.2 which is a high-resolution TEM micrograph. Crystalline particles are indicated by white dotted lines and part of a pore by the black dotted line. The inset image represents the Fourier transform of the image showing signals due to the amorphous matrix in addition to isolated spots which can be indexed as (111), (220) and (311) spots of Si.

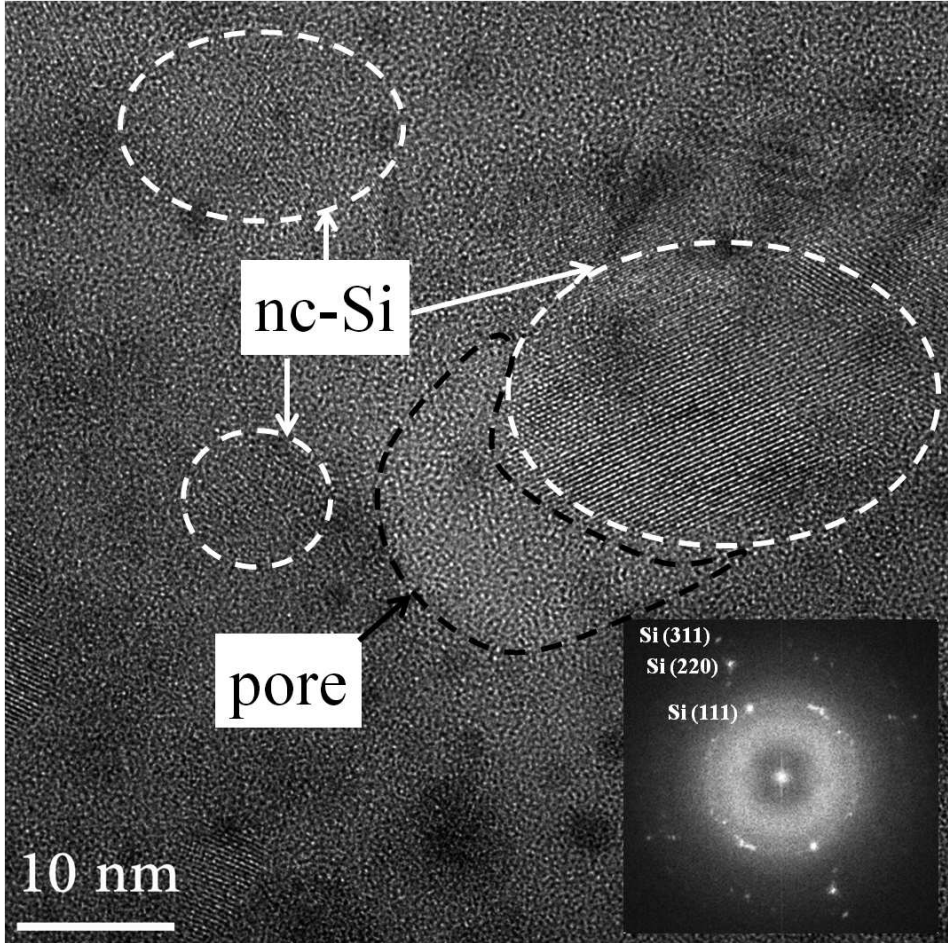
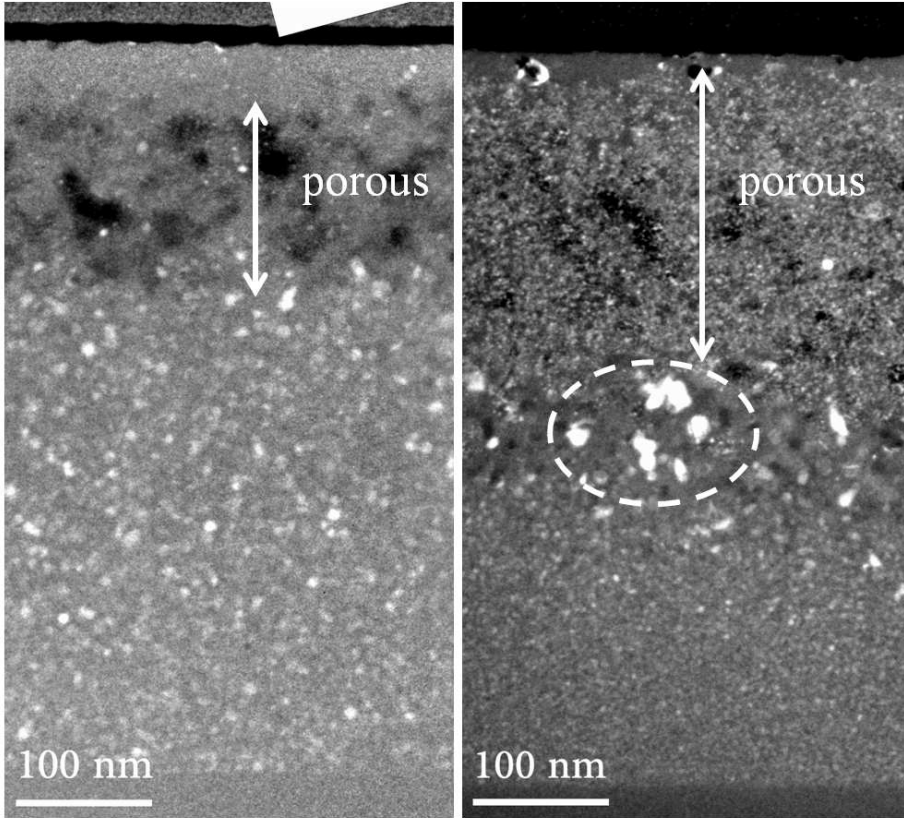


Figure 4.2: High-resolution TEM image from the porous part of the sample presented in Fig. 4.1. The porous material is amorphous and contains a small nc-Si particle indicated by white dashed lines. The brighter part in the center marked by a black dashed line contains part of a pore. The inset is a Fourier transform of the image revealing signals due to the amorphous matrix as well as due to crystalline particles whose spots can be indexed as resulting from (111), (220) and (311) planes of silicon.

In order to get insight into the temporal evolution of the porous region we compare the microstructure of samples treated with the laser intensity fixed at $1.4 \times 10^5 \text{ W/cm}^2$ and irradiation times of 20 ms and 120 ms, respectively. Fig. 4.3 shows corresponding HCDF images for the center part of the illuminated line. Two observations are apparent, i.e. (i) an increasing depth of the porous region with increasing irradi-

ation time and (ii) some much larger nc-Si particles (20 nm) existing almost side by side to pores with virtually the same size (see dashed oval) in Fig. 4.3(b). We note here, that some of the nc-Si particles exhibit an irregular shape with some of them being strongly elongated which is not visible for the smaller processing time.



(a). $1.4 \times 10^5 \text{ W/cm}^2$, 20 ms (b). $1.4 \times 10^5 \text{ W/cm}^2$, 120 ms

Figure 4.3: HCFD images obtained in the center part of the samples irradiated for 20 ms (a) and 120 ms (b) at a fixed laser intensity of $1.4 \times 10^5 \text{ W/cm}^2$. The comparison indicates that the prolonged irradiation time increases the thickness of the porous part and some larger nc-Si particles can be observed in the region adjacent to the porous part labeled by the white dashed oval. Simultaneously, the particle density is decreased there indicating coarsening to be dominant.

4.3.2 Chemical composition of porous silicon oxide

According to the structural investigations in the previous section, the damaged region consists of amorphous material containing pores and a – compared to the nc-Si region – small density of crystalline silicon particles. Figure 4.4(a) is a STEM bright-field image obtained from a sample irradiated with a laser intensity of 1.75×10^5 W/cm² for 20 ms. Again, the silica substrate, the nc-Si, and the porous region are easily recognized (the dark area on the right-hand side corresponds to the preparation-related Au and Pt:C layers). EDX maps measured in the same area as the STEM image are averaged along the vertical direction, i.e. parallel to the surface. The resulting profiles are summarized in Fig. 4.4(b) after calibrating the oxygen-to-silicon ratio x such that $x = 2$ is obtained in the region of the fused silica substrate. As a consequence, the profiles of silicon and oxygen counts coincide in the substrate region, whereas in the nc-Si region the silicon-rich nature of the material is revealed by the higher silicon signal. In the porous region, the two profiles again coincide which provides evidence that the average composition there is close to SiO₂. The lower level of both silicon and oxygen counts reflects the porous nature of this region. In addition, a thin layer at the surface is chemically close to SiO₂ but does not display the porous character as is concluded from the higher level of the silicon and oxygen counts.

4.3.3 Quantitative EDX study on porous part

In order to analyze the composition in the porous region more accurately, we collected EDX spectra in samples irradiated at 1.4×10^5 W/cm² for 60 ms. Figure 4.5 (a) presents a STEM bright-field image of this sample showing regions A, B, and C where EDX spectra were collected. In order to simultaneously visualize composition changes and thickness changes related to the porosity we present the EDX data as plots of calibrated O-K counts vs. Si-K counts (see Fig. 4.5(b)) where the calibration has again been performed such that the oxygen-to-silicon count ratio x measured on a pristine silica reference sample is $x = 2$. Hence, in such a plot, the oxygen-to-silicon ratio x of a material can be determined as the slope of a fitted straight line through the origin whereas thickness variations and fluctuations of the incident electron beam intensity during the EDX experiment will move the data points along the straight line.

Fig. 4.5(b) shows the resulting plots for pristine SiO_2 and SRSO reference samples together with the fitted straight lines through the origin as dashed and dotted lines, respectively¹. In addition, data points from regions A, B and C are included which have been simultaneously fitted (solid line) yielding an average composition of the porous region of $x_p = (1.91 \pm 0.04)$ (see table 4.1) which is slightly below SiO_2 and considerably larger than the corresponding value for the untreated SRSO of $x_{\text{SRSO}} = (1.49 \pm 0.04)$. Taking into account the structural data described in Sec.4.3.1 it can be concluded that the porous region consists of an (amorphous) SiO_2 matrix containing some residual silicon nanoparticles.

Region	x	Δ [%]
pristine SiO_2	2.00 ± 0.02 ²	3.2
pristine SRSO	1.49 ± 0.04	4.5
porous	1.90 ± 0.04	21

Table 4.1: Results of fitting straight lines through the origin to the data in Fig. 4.5(b) providing the oxygen-to-silicon ratio x . For the pristine SRSO sample $x=1.49$ is observed and for the porous region $x=1.90$ which is close to SiO_2 . This implies that most of the silicon surplus has been removed from the porous region. In addition, the relative fluctuations Δ of the silicon counts are given. Using the results from the non-porous reference samples Δ values between 3 and 5% are estimated as being due to thickness changes in a typical FIB prepared sample and due to fluctuations of the incident electron beam intensity. Hence, the much larger value for the porous region mainly stems from the pores in the material.

In order to have a measure for the porosity of the material which manifests itself by fluctuations of the effective sample thickness, we use the quantity

$$\Delta := \frac{r_{IQ}(I_{Si})}{2\langle I_{Si} \rangle} \quad (4.1)$$

where $\langle I_{Si} \rangle$ denotes the median of the silicon counts I_{Si} and $r_{IQ}(I_{Si})$ the interquartile range of I_{Si} , i.e. the width of the interval containing 50% of the data and centered around the median. The respective values are listed in Table 4.1 indicating that Δ values between 3 and 5% represent fluctuations due to thickness changes induced by FIB sample preparation and fluctuations of the incident electron beam intensity which is much below the value of 21% observed for the porous region.

¹ Note, that straight line fits have been carried out taking into account experimental uncertainties in both, the oxygen and the silicon signal.

Finally, we present EELS data obtained in the low-loss regime, i.e. in the energy range between 4 and 40eV, from a spectrum image recorded in the center of a sample irradiated with a laser intensity of $1.4 \times 10^5 \text{W/cm}^2$ for 60 ms. Figure 4.6 shows EEL spectra from the porous region which were averaged avoiding contributions from isolated silicon particles together with spectra measured on pristine silica (SiO_2 reference) and untreated SRSO (SRSO reference). In order to provide better comparison, EEL spectra were normalized by their maximum value. The plasmon peak that represents SRSO is centered at 20.5 eV while the plasmon peak center of SiO_2 is at 22.5 eV, which is also the position of the plasmon peak observed in the porous region. In spite of the slightly broader plasmon peak it can be concluded that plasmon properties in the porous part are virtually identical to those of the silica reference. We note here, that considerable differences are observed in the very low-loss region related to the bandstructure of the material indicating states in the porous material in a range below the bandgap of SiO_2 of about 8eV [38].

4.4 Discussion

Before we discuss our experimental observations, let us briefly summarize the most important points and immediate conclusions:

- The damaged region consists of an amorphous matrix whose composition is close to that of SiO_2 which is consistently concluded from the plasmonic part of EEL spectra and EDX data (Figs.4.4, 4.5 and 4.6). The matrix contains pores and crystalline silicon particles with a density much smaller than that in the nc-Si region (Fig. 4.1). As a consequence we have to conclude that the excess silicon present in SRSO compared to silica has been almost completely removed in the porous part.
- Increasing the irradiation time leads to an increased depth of the porous region which provides evidence that it evolves from the surface into the oxide layer (Fig. 4.3).
- In a transition region from purely porous material to the nc-Si region crystalline silicon particles are observed which are

- much larger than particles in the nc-Si region and are comparable in size to the adjacent pores (Fig. 4.3)
- irregularly shaped and strongly elongated (Fig. 4.3)

Loss of excess silicon as a result of CW laser irradiation has been reported before [85] for free-standing SRSO films which agrees with our observation described above for substrate-bound SRSO. As a possible mechanism, the authors propose thermodiffusion of silicon, i.e. diffusive transport of predominantly silicon as a result of temperature gradients induced by the laser-inherent inhomogeneous heating. Pore formation as a result of diffusion – known as the Kirkendall effect in solids [155] – seems to be unlikely under our conditions since silicon dioxide behaves as a – highly viscous – liquid at temperatures sufficiently high for nc-Si particle formation [156] rather than a solid.

In the following, we will describe a mechanism that accounts for experimental observations described above and in previous work [85, 72] and which can be regarded as preferential ablation of silicon embedded in a transparent and highly viscous liquid. Fig. 4.7 describes the mechanism in terms of sequential steps:

- Step 1 As the initial situation (Fig. 4.7(a)), we assume the typical microstructure observed after completion of the SRSO decomposition into nc-Si particles embedded in a SiO_2 matrix. Hence, light will be selectively absorbed in nc-Si particles similar to the selective absorption observed in multilayers of amorphous silicon and SiO_2 [157]. In such a scenario, nc-Si particles serve as heat sources for the surrounding material. Furthermore, since the decomposition is assumed to be completed, coarsening (or Ostwald ripening) of nc-Si particles will occur in order to reduce the total interfacial energy, i.e. growth of large particles at the expense of small ones.
- Step 2 The crucial assumption for the proposed mechanism is the effect of *quantum confinement* on light absorption by nc-Si particles [158] implying stronger energy deposition in large particles than in small particles. Fig. 4.7(b) schematically shows the resulting coarsening which should be faster close to the surface because of the higher laser intensity there. It should be noted, that the strong absorption of larger particles close to the surface will reduce the laser intensity in deeper parts of the material which amplifies the

difference in the ripening kinetics between top and bottom regions.

Step 3 Further energy deposition will lead to melting of large particles and finally to their ablation which is schematically shown in Fig. 4.7(c) resulting in a microstructure as observed experimentally (see Figs.4.1 and 4.3). As a result, the top layer will consist mainly of SiO_2 with a few nc-Si particles. It is interesting to note that these 'residual' silicon particles basically stop taking part in further coarsening since the surrounding material is depleted of silicon particles. Furthermore, the remaining porous SiO_2 is virtually transparent to the incident laser which basically restores the initial situation.

Step 4 Extension of the porous layer into the nc-Si region by repeating steps 1 to 3 (Fig. 4.7(d) and (e)).

The mechanism described above qualitatively explains our observations, in particular the advancing of the porous layer into the nc-Si layer with increasing time and also the similar size of pores and silicon particles in the transition zone between the porous and the nc-Si region (Fig. 4.3). We should emphasize here that the pore size in the porous material above the transition zone not necessarily coincides with that of nc-Si particles ablated earlier since the surrounding SiO_2 'sponge' might relax during the course of laser irradiation leading to shrinking or even collapsing pores since silicon dioxide behaves as a highly viscous liquid at temperatures above 1200°C [156]. In fact, such a relaxation has been observed as a slight decrease of the layer thickness in the center of the irradiated lines [72].

4.5 Conclusion and Outlook

Using various techniques of TEM imaging and analysis we have studied the microstructure of damaged regions observed in CW laser irradiated substrate bound SRSO samples for irradiation conditions above the threshold intensity [89, 72]. It is consistently shown that such regions can be viewed as porous SiO_2 containing a low density of crystalline silicon particles. On the basis of our observations we propose a model of 'selective silicon ablation' that describes the pore formation starting after completion of the decomposition of SRSO. Basic ingredients are the selective and size-dependent absorption of light by nc-Si particles in a transparent

SiO₂ matrix leading to predominant heating of regions containing large particles, their melting and eventually their ablation leaving behind pores with similar size as the largest silicon particles as experimentally observed. Bearing in mind that at temperatures comparing to the melting point of silicon SiO₂ has to be viewed as a viscous fluid[156], the proposed process has some similarity to laser ablation in liquids previously used for nanoparticle formation[159]. Clearly, for more quantitative modeling details such as heat transfer from particles to the matrix, size-dependent absorption, heat conduction in the decomposed layer and losses at the surface as well as to the substrate have to be included and combined in numerical simulations which is beyond the scope of the present paper. Nevertheless, it provides some guidelines for more controlled laser processing of SRSO for nc-Si production without the introduction of laser damage. Up to here we have discussed the formation of porous SiO₂ as an unwanted side-effect of laser irradiation of SRSO. However, mesoporous silica particles have attractive properties for applications in bio-medical sciences[160] implying that a controlled formation of porous silica on substrates or even devices might be possible by well-controlled laser irradiation of SRSO.

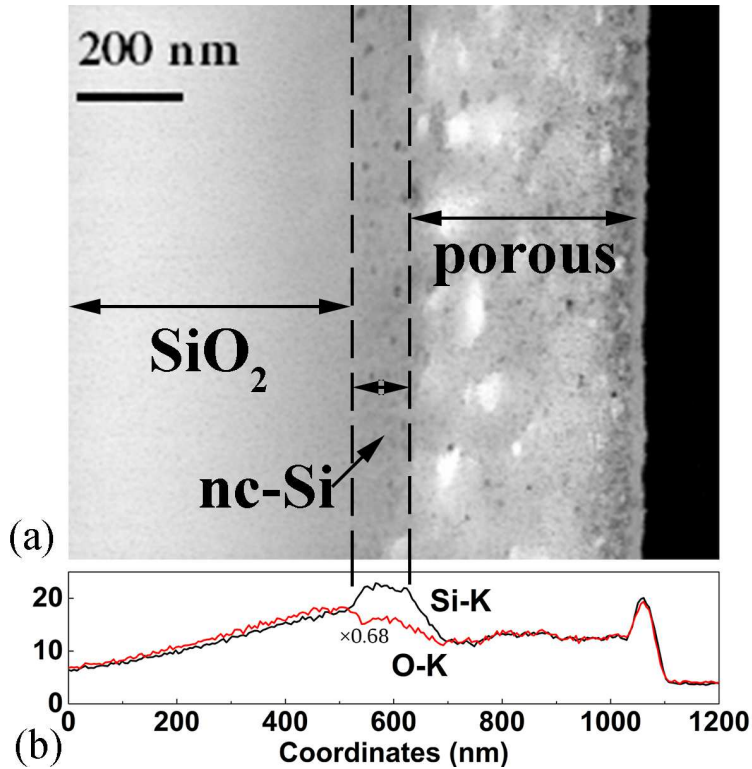


Figure 4.4: (a) STEM bright field TEM image from the center part of a CW laser irradiated sample with a laser intensity of $1.75 \times 10^5 \text{ W/cm}^2$ and an irradiation time of 20 ms. (b) Profiles of oxygen and silicon counts obtained from EDX maps by averaging in vertical direction, i.e. parallel to the surface. Note, that the oxygen signal has been calibrated such that the oxygen-to-silicon ratio x is $x = 2$ in the silica substrate. The coincidence between Si-K and rescaled O-K counts indicates that the porous material is chemically close to SiO₂ qualitatively.

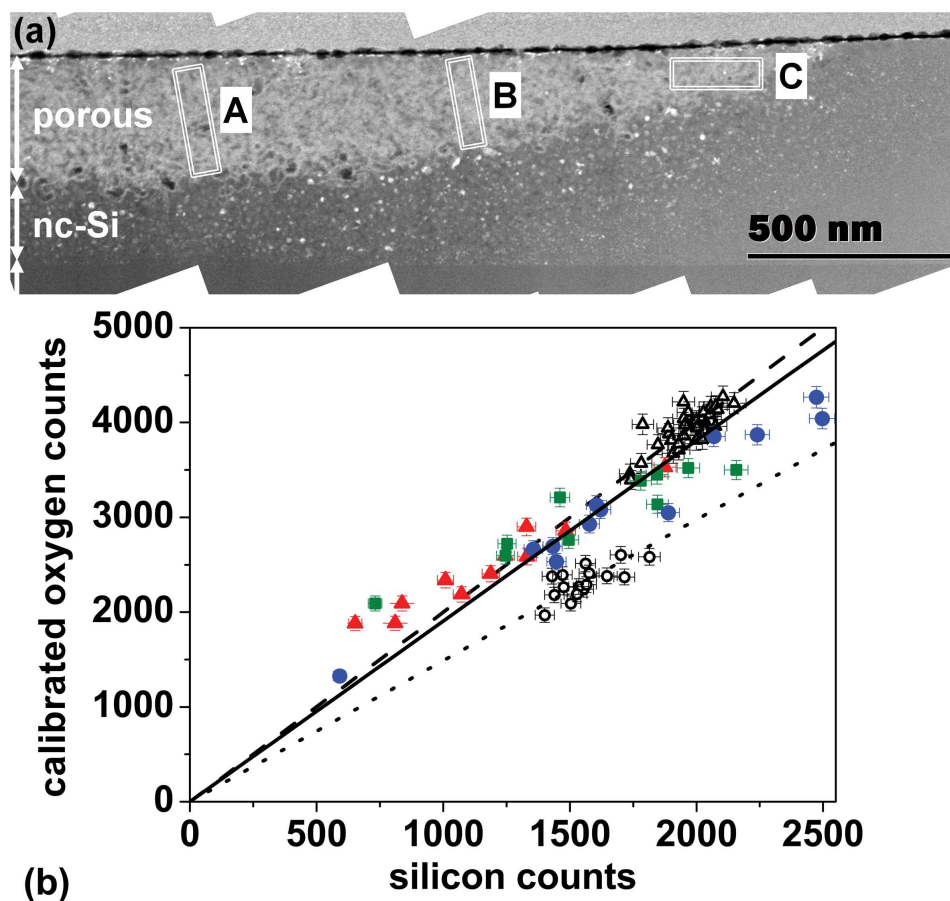


Figure 4.5: (a) STEM bright-field image for a sample irradiated at $1.4 \times 10^5 \text{ W/cm}^2$ for 60 ms showing three regions A, B and C in the porous part where EDX spectra were collected. (b). Plot of calibrated oxygen counts vs. silicon counts for a pristine silica reference (open triangles) used for calibration, pristine SRSO (open circles) serving as starting material for laser irradiation, data from region A (red filled triangles), B (filled green squares) and C (filled blue circles). The fits to a straight line through the origin are shown for the silica reference (dashed line), the SRSO reference (dotted line) and the data from regions A, B and C (solid line) whose slopes represent the oxygen-to-silicon ratio x as summarized in Table 4.1.

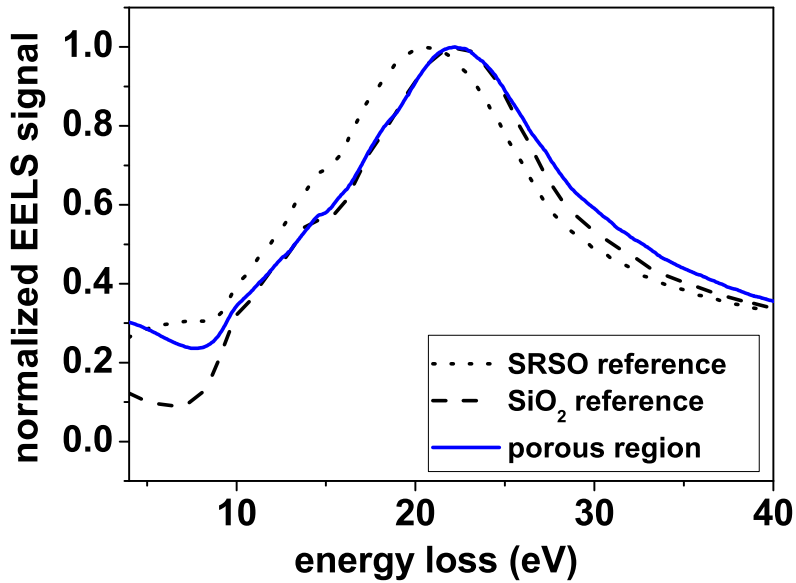


Figure 4.6: Normalized EEL spectra of the porous part in a laser irradiated sample compared to those measured on SRSO and SiO₂ pristine samples. The plasmon peak of the porous material has its maximum position at the same energy loss as that of SiO₂ (22.5eV) but is slightly broader at higher energy losses. In addition, the higher energy loss below about 10eV indicates the existence of electron states below the bandgap energy of SiO₂ of about 8eV.

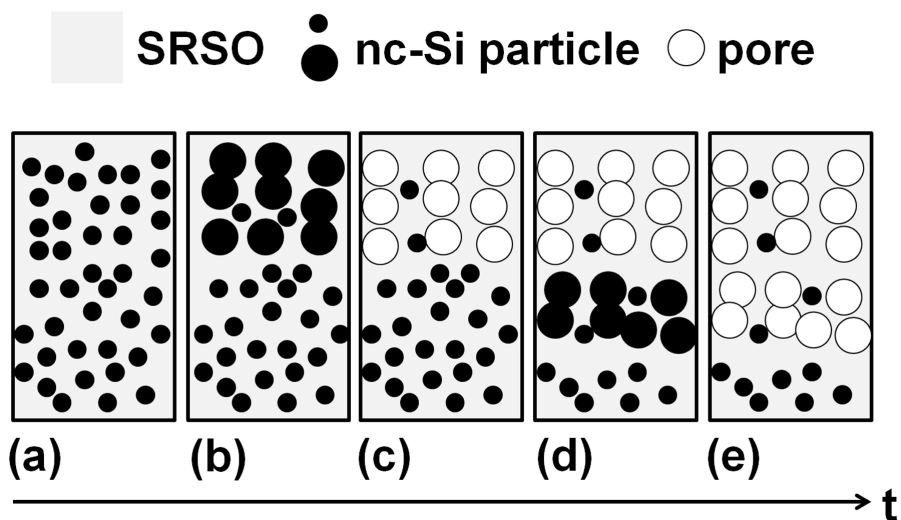


Figure 4.7: Description of the temporal evolution of the microstructure CW laser irradiated SRSO samples as the mechanism of 'selective silicon ablation' (for details, see text).

5 The nanoscopic Si–SiO₂ phase separation in silicon rich silicon oxide by continuous wave laser annealing: a quantitative approach

Laser annealing with micrometer beam spot have a great potential to integrate silicon light emitting diode (LED) on a single silicon chip. Silicon rich silicon oxide (SRSO or SiO_x, $x < 2$), one of the most important precursors to obtain silicon-based light-emitting materials, is treated by continuous wave laser irradiation to generate nc-Si particles in this work. Usually the decomposition of silicon rich silicon oxide (SRSO) induced by heating is regarded as the Si-SiO₂ phase separation. However, the measurement of related microstructure is still missing. In this paper, we investigate the micro-structure of nc-Si particle and its surrounding materials by hollow cone dark-field TEM imaging (HCDF), high resolution transmission electron microscopy (HRTEM), energy dispersive spectroscopy (EDX) and electron energy loss spectroscopy (EELS). In contrast to bright field TEM imaging and normal dark field imaging, the characterization of nc-Si by HCDF performs the dominated advantage like the visibility of more nc-Si particles and it provides a proper way of particle analysis. HRTEM shows the lattice fringes of nc-Si particle in an homogeneous amorphous matrix. EELS spectrum imaging, which is independent of lattice fringes, qualitatively confirms that this matrix is SiO₂. The EDX results in three typical areas of sample from the center to the edge presents the fluctuation of composition. The comparison between EDX simulation and the following simulation based two different models indicates that the Si core SiO₂ shell model is proposed to reflect the related chemistry information. In addition, the difference in fluctuation range in three areas is discussed and the combination of EELS with EDX analysis supports that nanoscopic phase separation occurs after laser irradiation in our materials system.

5.1 Introduction

Silicon is the most important material in electronics. The fabrication/processing technology of silicon electronics, in particular downscaling devices to single chips, has been well developed in the last 60 years. During last 30 years, the discovery of visible room-temperature (RT) photoluminescence (PL) in low-dimensional silicon material system (LDS) like porous silicon [4, 5] has drawn researchers' attentions on silicon photonics. The combination of silicon light-emitting diode with the silicon processing technology shows both potential in application and challenge in coupling electronics and optical functions on a single chip [86]. For such a device, normal heating treatments like furnace annealing technology can affect the neighboring materials and the substrate, which may deteriorate their performance. Thus, local heating is required in this case. In practice, instead of furnace annealing, the laser annealing with micrometer beam spot, which has been widely used to produce smaller features in Si-based materials [161], is expected to overcome the challenge.

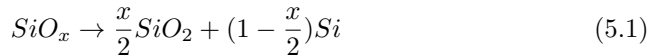
Although the advance of RT PL in LDS intensively stimulates the development of silicon photonics, several fundamental questions in this field are still not clear. As an example, the light emission center of RT PL is controversial. The size-dependent PL can be well explained by quantum confinement [5, 26, 162, 27, 163, 4]. While the size-independent PL is an open question although a lot of significant efforts have been tried out. For instance, the defect-related PL [30, 31, 32, 33, 164] and the PL emitted from the surface or interface states [35, 36, 37, 34] in LDS have been announced by several groups. As these PL mechanism usually involves in the detailed nanostructures in LDS, the characterization of the correlated microstructures is very necessary.

In contrast to bulk silicon, porous silicon (PS) has performed very high quantum efficiency in PL. However, the instability of PS, ie. the rapid ageing effect [11], limits its application. Except for PS, another LDS with good stability called Si nanocrystals (nc-Si) embedded in silica, which also performs RT PL [133, 154], has a great potential in Si based LED application. The nc-Si particles usually can be generated from the decomposition of silicon rich silicon oxide (SRSO or SiO_x , $x < 2$) by heating treatments like thermal annealing [93, 94, 95], ion bombardment [96] and laser irradiation [113, 114, 115, 71, 116, 121, 74]. It has been evidenced that the formation of nc-Si particles in SRSO requires high local temperature

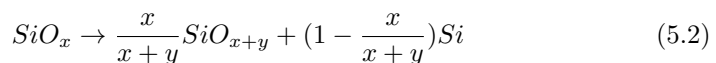
and pulsed laser irradiation can induce strong heat effects [113, 114, 115, 71, 116] due to high energy density in short pulsed length. But the laser ablation [71] in SRSO induced by pulsed laser heating has been observed, which can cause some performance penalty of the devices. The continuous wave (CW) laser annealing with intermediate heating effect has been confirmed to lead to the generation of nc-Si particles without any laser ablation in the literature [74]. In this report, to avoid the thermal load on the substrate [122], free-standing SRSO films are used. In our recent study [89], we have shown that nc-Si particles can be formed even in substrate-bound SRSO films by CW laser irradiation and the spatially resolved correlated microstructure is initially presented. Inspired by a recent work on macroscopic Si-SiO₂ phase separation driven by temperature gradient in CW laser irradiated SRSO [85], the structural evolution in our spatially controlled sample is investigated.

In the previous work [72], adjacent to nc-Si region, we observed a silicon oxide porous region with the chemical composition close to SiO₂, however, the macroscopic phase separation can not be supported by our experiment. Thus, it is interesting to explore the scale of Si-SiO₂ phase separation.

The decomposition of SRSO into Si and SiO₂ in chemical reaction can be written:



The formation of nc-Si after annealing have been confirmed by transmission electron microscopy and micro-Raman spectra in a lot of studies [85, 118, 20, 70], while the evidence of SiO₂ has been provided by Fourier-transform infrared spectroscopy (FTIR) [84, 103] and X-ray photoelectron spectroscopy (XPS) [108, 83]. A kinetic study on the SRSO decomposition [84] by B. J. Hinds et al. states that a SiO₂ shell attached at the nc-Si surface is formed which acts as the diffusion barrier. In other words, it may imply that the nanoscopic Si-SiO₂ phase separation occurs. However, the direct observation of such a SiO₂ shell is still missing. Because the nc-Si particle and SiO₂ shell still exist in the SRSO background and the contrast of which is weak. Actually the existence of this SiO₂ shell is still controversial. For example, the decomposition of SRSO can be also regarded as the formation of nc-Si and a more oxygen rich SRSO, which can be written:



Both Eq. (5.1) and Eq. (5.2) imply that a homogeneous shell is formed and the gradient of concentration in such a shell is not considered here. Thus, a quantitative study on the nanoscopic phase separation is required.

In this paper, we investigate the micro-structure of Si nanocrystals embedded in amorphous matrix by a number of TEM related techniques like hollow cone dark-field TEM imaging (HCDF), high resolution transmission electron microscopy (HRTEM), electron energy loss spectroscopy (EELS) and energy dispersive spectroscopy (EDX). EDX simulation based two defined models is performed for good comparison. Our investigations show that this amorphous matrix is SiO_2 and nanoscopic phase separation occurs in our materials system after CW laser irradiation.

5.2 Experimental details

The sub-stoichiometry SiO_x ($x < 2$) films with a thickness of 530 nm are deposited on 2 mm thick fused silica substrates by ion beam sputtering (IBS), conducted by a commercial coating supplier (Laseroptik, Garbsen, Germany). Locally resolved annealing on SiO_x (the diameter of laser beam is estimated to be $6 \mu\text{m}$) is done by a diode laser with continuous wave emission at 405 nm (Coherent Cube). The average irradiance is $1.5 \times 10^5 \text{ W/cm}^2$. A steady flow of nitrogen is purged into the housing enclosed SiO_x samples in order to prevent oxidation during annealing. The sample position is controlled by high precision positioning stages and the irradiation of lines is accomplished by moving the samples at a specified velocity. Focused ion beam (FIB, FEI Nova NanoLab 600) is employed to prepare cross-sectional TEM samples centered on the irradiated lines and oriented perpendicular to them. Prior to FIB preparation of TEM lamella, a thin Au layer (5 nm) is evaporated on the samples to avoid charging in FIB environment during SEM inspection.

The HCDF, HRTEM and EDX were conducted with a Philips CM200 TEM/STEM microscope with a field emission gun operating at 200KV. The HCDF mode is that the incident electron beam is tilted at a fixed angle with respect to the optical axis of the objective lens, after that the rotation of the tilted beam forms a hollow-cone illumination. To obtain the high contrast HCDF images, several factors for HCDF

should be considered to maximize the average intensity of the annular region during scanning. Although in some literatures, a slightly-convergent beam is discussed to be beneficial to increase the intensity, in this paper we still use the general parallel illumination for HCDF. Other factors like the rotation period and the integration CCD time is also necessary to be adjusted. We tested a lot of parameters for this, and in our best experience the period of rotation is 500 ms and the integration time is 5s. The HRTEM is employed to image the lattice fringe of nc-Si particle and its surrounding amorphous matrix with a spatial resolution of 0.19 nm.

The electron energy loss spectroscopy (EELS) measurement were done by using a Titan 80-300 Environmental atomic-resolution Scanning/Transmission Electron Microscope microscope equipped with a Gatan Image Filter operating at 300 KV. The convergence semi-angle of incident electron beam is 10 mrad and the collection semi-angle for the EELS spectrometer is about 27.8 mrad. Usually, the low loss region from 5 to 50 ev is employed to analyze the structure of Si and SiO₂ correlated materials because there are two plasmon peaks represent Si and SiO₂ respectively.

The EDX is worked at the scanning transmission electron microscopy (STEM) mode with a probe size of approximately 1 nm. The EDX detector in our Philips CM 200 microscope is a windowless detector and this provide the possibility of exploring the characteristic X-rays from light elements like Carbon and Oxygen. The typical EDX spectra of SRSO and SiO₂ from pristine sample (as deposited, without any further treatment) is presented in Fig. 5.1. The spectrometer can measure the characteristic X-rays from 0 to 20 Kev and a selected range from 0 to 9 Kev is shown here. The O-K X-rays sharp peak is clearly observed in both SRSO and SiO₂ with a center energy of 0.52 Kev while the Si-K X-rays peak is centered at 1.74 Kev. The difference in these two spectra is apparent. In contrast to SiO₂, in SRSO the Si-K cross-section (counts) is higher and the O-K counts is lower due to the excess Si component. The Cu-K X-rays peak at 8.04 Kev may stem from the copper grid that supports the TEM sample. Quantitative EDX analysis usually employs the Cliff-Lorimer equation [165] written below:

$$\frac{P_A}{P_B} = k_{AB} \frac{I_A}{I_B} \quad (5.3)$$

where P_A is percent of element A and P_B is percent of element B in such binary AB materials system; I_A and I_B are the cross section of the A and B characteristic X-rays; k_{AB} is termed as the Cliff-Lorimer factor, which is the calibrated factor

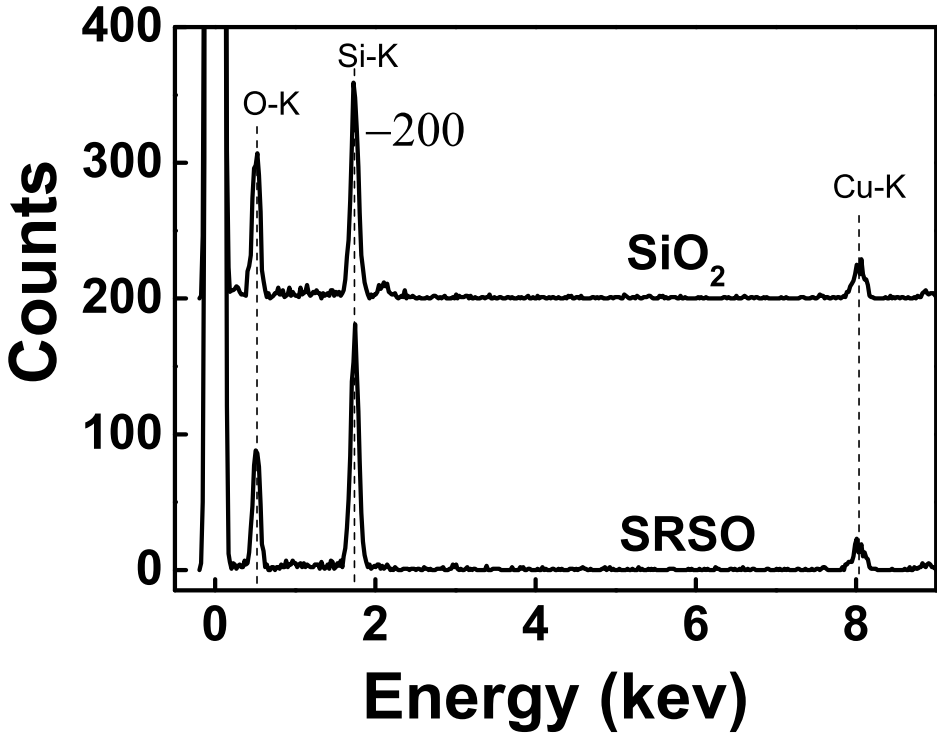


Figure 5.1: Typical EDX spectrum of SiO_2 and SRSO from the pristine sample without any subsequent treatment in a selected range from 0 to 9 KeV. Both O-K and Si-K X-rays peaks can be observed with a center energy of 0.52 KeV and 1.74 KeV respectively. In contrast to SiO_2 , in SRSO the Si-K counts is higher and the O-K counts is lower due to the excess Si component. The broad Cu-K peak at 8.04 KeV may be due to the copper TEM sample supporters.

that connects the composition with the X-rays counts. I_A and I_B equal to the total background-corrected characteristic X-ray counts of element A and B in the defined energy window. Thus, in our materials system, the Eq. (5.3) is rewritten:

$$\frac{P_O}{P_{Si}} = k \frac{I_O}{I_{Si}} \quad (5.4)$$

As the composition of pristine SiO_2 substrate is fixed and known, we can use this standard EDX spectra to calculate k factor in Eq. (5.4). To get the absolute characteristic X-rays counts, the continuous bremsstrahlung background which follows the Kramers' Law should be considered. For the Si-K peak, we compare original counts with background-corrected one in a number of SiO_2 EDX spectra and re-

gard that it is reasonable to ignore this background since only a error of less than 2% is generated. However, the case in O-K background correction is a little complicated. The background based on Kramers' Law should have a steep continuous increase at low energy scale (less than 1 or 1.5 Kev) when the energy towards zero. Actually, in experiment this tendency can not be observed and instead the background drop down to zero very fast due to low collection/processing efficiency of the detector at low energy scale. Although the O-K background evaluation is difficult, we believe that it is still rational to ignore this background since it should be smaller than the Si-K background we neglected above. 30 EDX spectra from SiO₂ substrate is employed to calculate the k factor and it is 2.95 with a deviation of 0.10. As these spectra is obtained in different local area in sample, only the thickness effect (the Si-K counts is in direct proportion to the O-K counts) can be observed. Based on this k factor, the x value in pristine SRSO (SiO_x) sample is calculated to be 1.5. Similarly, thickness effect can be observed in a number of SRSO EDX spectra.

5.3 The description of model and simulation

Stimulated by the evidence of SiO₂ from FTIR and XPS mentioned before, the decomposition of SRSO is regarded as the formation of Si and SiO₂ that follows the Eq. (5.1). This is the complete phase separation. Although the shape of nc-Si particle in real system is not perfectly spherical, the simplification of geometry factor is considered and the model used here assumes the Si core is a sphere and the SiO₂ works as a shell with homogeneous thickness attached at the nc-Si surface. In other words, Eq. (5.1) indicates a certain volume SiO_x transforms into a Si core surrounded by a SiO₂ shell. This equation reflects the stoichiometry in its simplest way completely ignoring, however, any volume changes that might be involved in the reaction. The molar density of these three components is considered. And the correlated symbols and values are listed in table 5.1.

The basic assumption then is that no material is lost during the reaction, i.e. that the number of Si-atoms and O-atoms is unchanged. Based on the conservation of Si and O atoms in Eq. (5.1), we have

$$R_x^3 \rho_x = R_{Si}^3 \rho_{Si} + (R_2^3 - R_{Si}^3) \rho_2 \quad (5.5)$$

Table 5.1: A list of symbols for derivation in core shell model structure and their meaning

Symbol	meaning	values
ρ_x	mol. density of SiO_x	$2.9 \cdot 10^{22} cm^{-3}$
ρ_{Si}	mol. density of Si	$5 \cdot 10^{22} cm^{-3}$
ρ_2	mol. density of SiO_2	$2.65 \cdot 10^{22} cm^{-3}$
R_x	radius of transformed SiO_x sphere	-
R_{Si}	radius of Si core	-
R_2	radius of SiO_2 shell around Si core	-

$$x \cdot R_x^3 \rho_x = 2 \cdot (R_2^3 - R_{Si}^3) \rho_2 \quad (5.6)$$

yielding

$$R_{Si} = \left(\frac{2-x}{2} \frac{\rho_x}{\rho_{Si}} \right)^{1/3} R_x \quad (5.7)$$

$$R_2 = \left(1 + \frac{\rho_{Si}}{\rho_2} \frac{1}{2/x-1} \right)^{1/3} R_{Si} = \left(\frac{x}{2} + \frac{2-x}{2} \frac{\rho_2}{\rho_{Si}} \right)^{1/3} R_x \quad (5.8)$$

The simulation is running under the environment of Software Digital Micrograph with an encoded script. Random number is employed to define the position of each particle in 3D samples. The generation of nc-Si core and SiO_2 follows the histogram concerning of the particle number as a function of diameter in experiment. At the beginning, the molecular density, the composition of SiO_x , sample size and sample thickness can be set. In the end, the 2D projections of Si and O 3D samples are obtained and a 2D histogram that describes the dependence of the number of O atoms on the number of Si atoms will be displayed.

It should be noted that after this core shell model simulation, some rest unreacted SRSO volume is still left. Because we would like to know if all the SRSO volume are consumed or not, we make the further simulation in which the experimental histograms indicating nc-Si particles are upscaled such that the entire SRSO is decomposed into nc-Si and SiO_2 and the stoichiometry is preserved for good comparison.

5.4 Results

5.4.1 HRTEM investigation for nc-Si particle and its surrounding materials

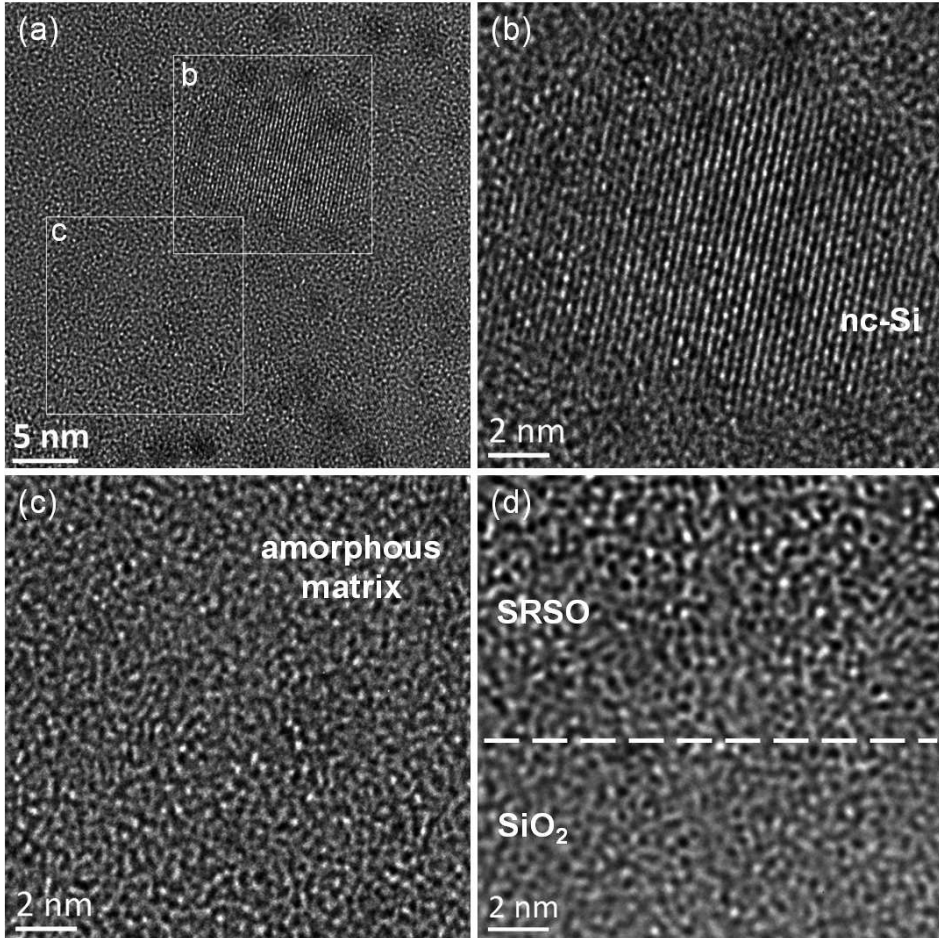


Figure 5.2: (a). Typical HRTEM image for nc-Si particle embedded in amorphous silicon oxide matrix: the magnified images for nc-Si particle (b) and matrix (c); (d) HRTEM image of SRSO/SiO₂ interface (white dashed line) from pristine samples.

The HRTEM image for one typical nc-Si particle and its surrounding environment is presented in Fig. 5.2(a). The Si nanocrystal with the typical (111) indices

of crystal face can be clearly observed in the magnified one in Fig. 5.2(b) and the interface between it and its surrounding amorphous matrix magnified in Fig. 5.2(c) can be distinguished. It can be observed that only from HRTEM results the amorphous matrix surrounds nc-Si is homogeneous and does not show a second phase. In contrast, we also show the HRTEM image of SRSO/SiO₂ interface (white dashed line) from pristine samples in Fig. 5.2(d). Here the structural difference between SRSO and SiO₂ is quite weak but still can be observed. This may also support that the amorphous matrix in Fig. 5.2(c) is a single phase and it should be SiO₂ or SiO_{x+y} described in Eq. (5.1) and Eq. (5.2). However, the chemistry of matrix can not be determined here.

It should be noted that the reaction involved in Eq. (5.1) and Eq. (5.2) implies the complete SRSO consumption. However, unreacted SRSO, which can be the second phase mentioned above, may still exist in laser irradiated samples after reaction. And the reason that HRTEM can not detect the second phase may stem from two aspects: 1. The weak heterogeneity between SRSO and SiO₂/SiO_{x+y} can not provide good contrast; 2. The SiO₂/SiO_{x+y} immersed in the SRSO matrix and its thickness is too small in comparison with that of the sample, which can not provide the significant signal for imaging. Preparing a much thinner TEM sample may be expected to be good solution for the contrast improvement and while the internal nano-structures damage during deep thinning process is still a challenge.

5.4.2 EELS spectrum imaging of nc-Si particles and their amorphous matrix

In contrast to HRTEM imaging, EELS spectrum imaging has an advantage of lattice fringe independence. It means that no matter nc-Si or a-Si particle is formed in SRSO sample, it can be detected with the Si plasmon peak. On the other hand, EELS spectrum imaging can image those nc-Si particles which can not be detected by HCDF due to out of diffraction. The energy loss spectrum can be divided into three regions with different ranges of energy loss: zero loss, low loss and high loss. The zero loss stems from electrons that are scattered elastically by sample or transmitted electrons without any energy loss; The low loss, which we are interested in this paper, is dominated by the absorption concerning of band gap (0-10 eV) and the energy loss in the plasmon peak (10-50 eV) that describes the excitation of collective vibrations of valence electrons in sample; the high loss

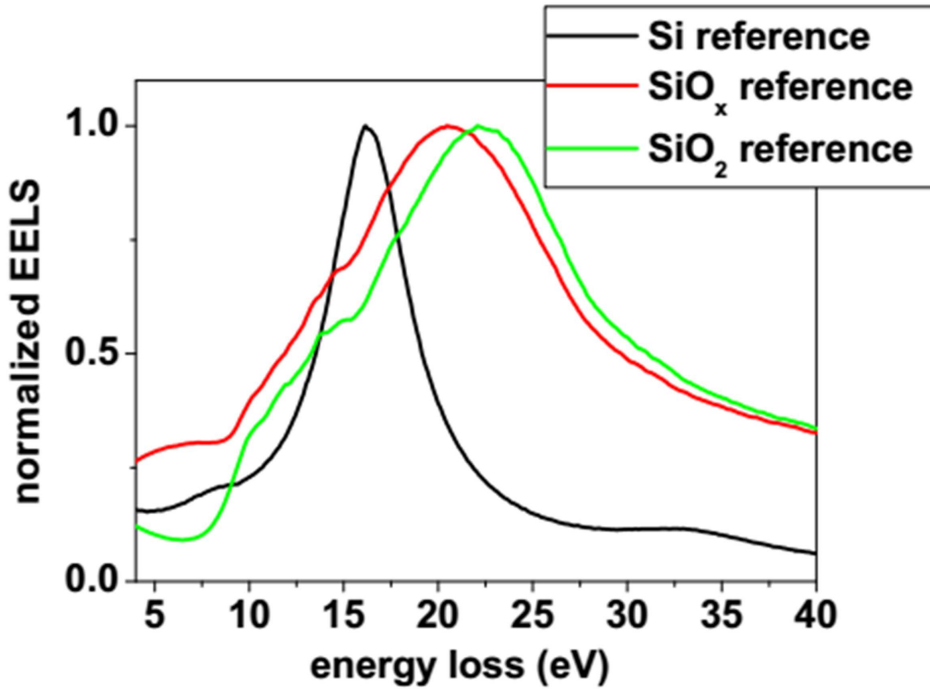


Figure 5.3: Reference EEL spectra obtained from pristine SiO_x on a SiO_2 substrate and crystalline silicon. Sample thickness was similar to the case of cw laser irradiated materials. For silicon, the pronounced plasmon peak at 16.8 eV is observed whereas SiO_x and SiO_2 both show a broad plasmon signal with maxima at about 20.6 eV and 22.4 eV, respectively. Note the considerably different spectra in the low energy range (4-10 eV)

with weak signal is due to inner shell ionization of atom (ie. the Si K-edge at 99 eV and O K-edge at 521 eV). To characterize the Si based materials, the low loss part in EELS is usually employed and reported in literatures [92], because they are two distinguishable plasmon peaks that represent the Si and SiO_2 components respectively. Here we present the EELS spectra of Si from crystalline Si sample, SiO_x and SiO_2 from pristine sample in Fig. 5.3. The pronounced Si plasmon loss peak is centered at 16.8 eV while SiO_x and SiO_2 both show a broad plasmon signal centered at about 20.6 eV and 22.4 eV, which is comparable to the other literatures [166, 167, 92].

EELS spectrum image is collected to reflect the chemical distribution of the nc-Si particle and its surrounding. As presented in Fig. 5.4, STEM-ADF image

is firstly obtained to display different regions (porous, nc-Si and SiO₂) in CW laser irradiated SRSO sample. The green box indicates the region of the spectrum image (nc-Si region in the center of sample) and the region used for drift correction is marked by the yellow box. We tried to use the spectra in Fig. 5.3 to fit with the EELS spectrum and the fitting results with the combination of Si and SiO_x is not good. However, the combination of Si and SiO₂ fits quite well with the spectrum imaging results. The deconvolution result from Si plasmon peak presented in Fig. 5.4(b) shows that Si nanoparticles are embedded in a background. The SiO₂ deconvolution result in Fig. 5.4(c) displays that the black particles are corresponding to Si and the SiO₂ works as the background. Thus, it is concluded this surrounding matrix of Si nanoparticles is SiO₂ qualitatively.

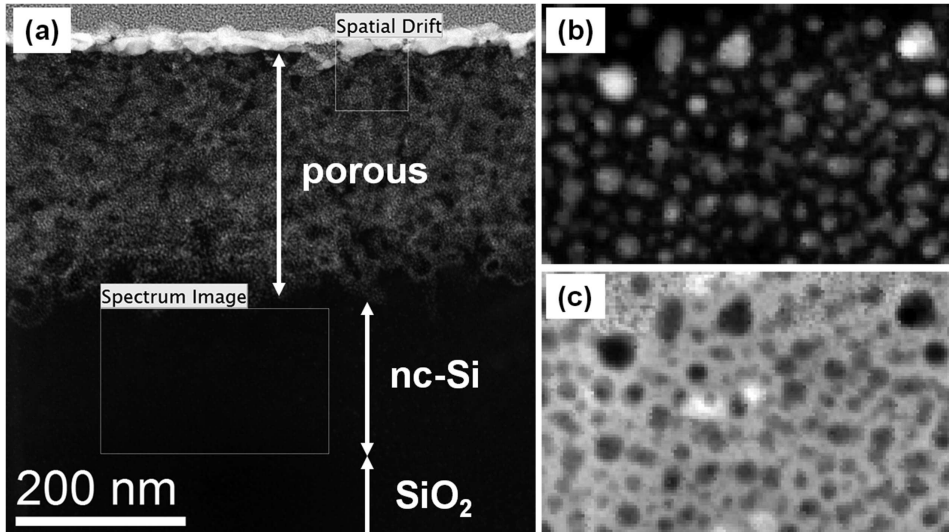


Figure 5.4: (a). ADF image showing the region of the spectrum image (green box) and the region used for drift correction (yellow box); Results of deconvolution: (b) Spatial distribution of the fraction a of Si plasmons and (c) fraction of SiO₂.

5.4.3 HCDF and particle analysis

The HCDF mode is employed to image the nc-Si particles in an amorphous background with a point spatial resolution of about 1 nm. We compare the application of bright field TEM imaging (BF), normal dark field imaging (DF) and HCDF for

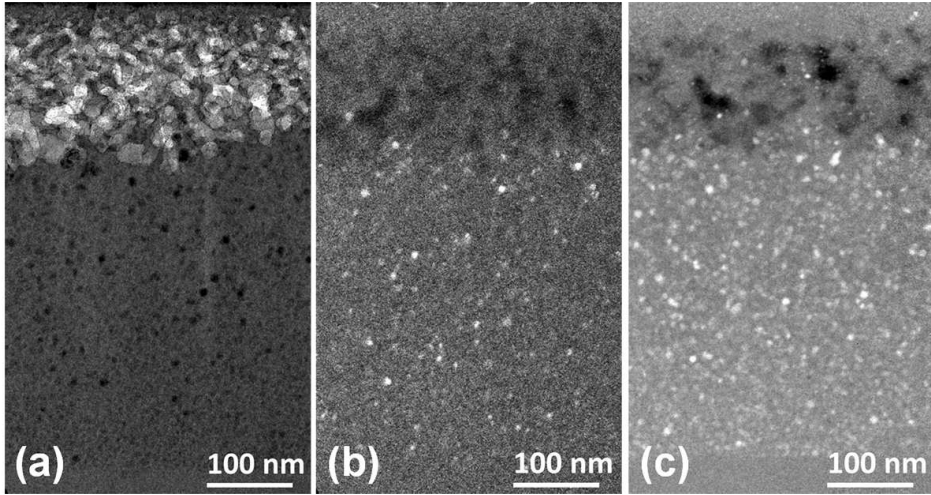


Figure 5.5: The comparison of the images for the center part of the same irradiated SRSO films by different techniques: (a) Bright field imaging (BF); (b) Dark field imaging (DF) and (c) Hollow cone dark field TEM imaging (HCDF). Three inhomogeneous regions called porous, nc-Si and substrate is presented from top to bottom. In contrast to BF and DF, the advantages of HCDF are clearly seen here that more nc-Si particles with high contrast in an amorphous background are visible and the SRSO/substrate interface is clearly distinguished.

the center part of the same irradiated SRSO sample as presented in Fig. 5.5. In consist with the previous study, three visible regions namely porous, nc-Si and substrate region can be distinguished from top to bottom in samples. The BF image in Fig. 5.5(a) displays high contrast of porous region while the contrast of nc-Si particle (dark spot) is quite low because of its less scattering, and the nc-Si region/substrate interface is clearly observed. The DF image in Fig. 5.5(b) shows weak contrast for porous region and the high contrast of a few nc-Si particles in amorphous background can be obtained. In contrast to DF image, the HCDF image preform a number of advantages especially in nc-Si region: 1). more nc-Si particles with high contrast are visible which is very meaningful to the size distribution of particles in statistics; 2). the nc-Si region/substrate interface is apparently distinguished, as a consequence, the BF image is not required to calibrate the interface position which can not be determined accurately in DF image. The HCDF image of cross sectional CW laser irradiated sample is presented in Fig. 5.5(c). Similar to the previous study [89], the sample has three well-distinguished parts from top to bottom (porous, nc-Si and SiO_2 substrate) and the nc-Si part is focused on. Here we select three areas labelled with A, B and C in Fig. 5.6(a)

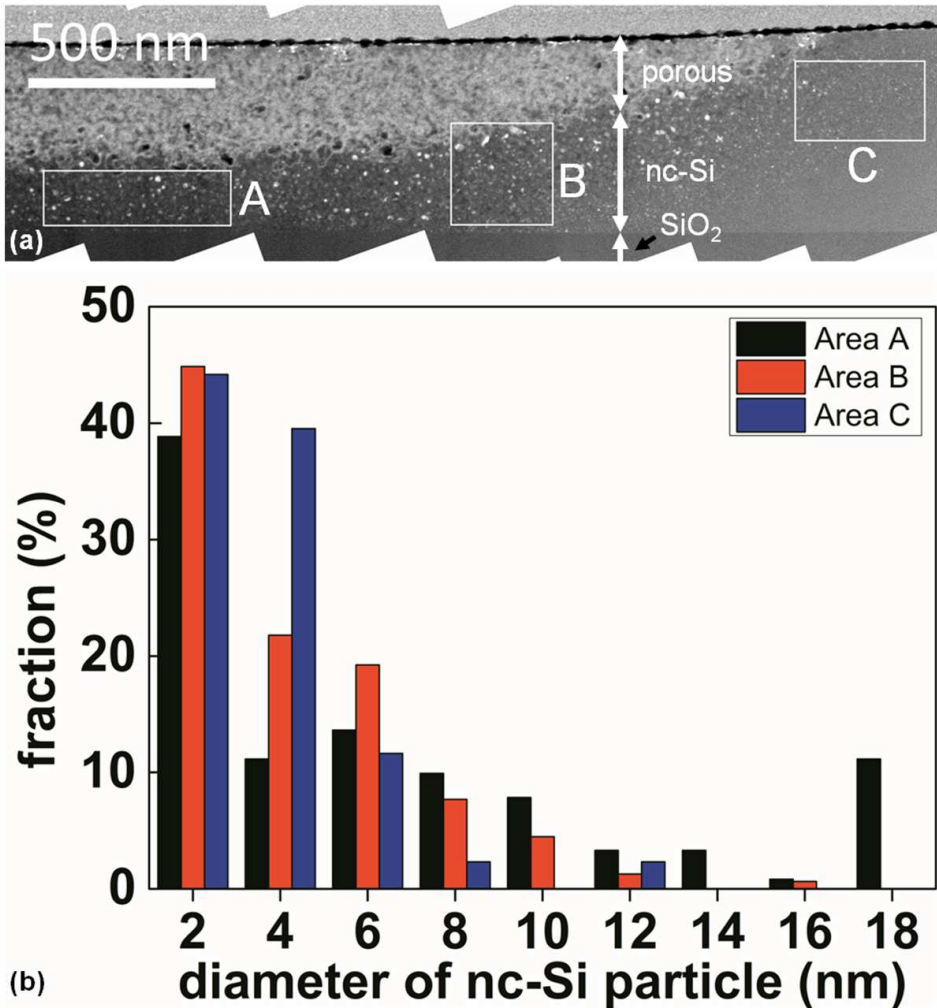


Figure 5.6: (a). HCDF image for the cross sectional TEM sample and three parts (porous, nc-Si, SiO₂) are observed: Three selected areas (A, B and C) are employed for particle analysis and the corresponding histogram is presented in (b).

with the equal space to guarantee the homogeneity of sampling for statistics and the SiO₂ images are used for background correction of A, B and C.

The software ImageJ with an automation procedure for particle analysis is used. Because the spatial resolution of HCDF is 1 nm and the size of the minimum nano particle in SiO₂ matrix mentioned in literatures is about 1.2 nm [88, 90], the

detectable size of particle is set as 2 nm in software ImageJ. The particles with the circularity from 0.1 to 1.0 are included and the ones at the edge of the selected region are excluded for analysis. The fraction histogram of nc-Si particle with size in area A, B and C is presented in Fig. 5.6(b). It can be seen that the fraction of particles in area A is apparently higher than that in area B and C. In particular, area A have almost 10% of particles with a diameter of 18 nm which area B and C do not have. For smaller particles, the fraction of ones with a diameter of 2 nm is quite close (40-45%) in these three areas while the fraction of ones with size of 4 nm increase from area A to C.

5.4.4 The comparison between EDX experiment and simulation

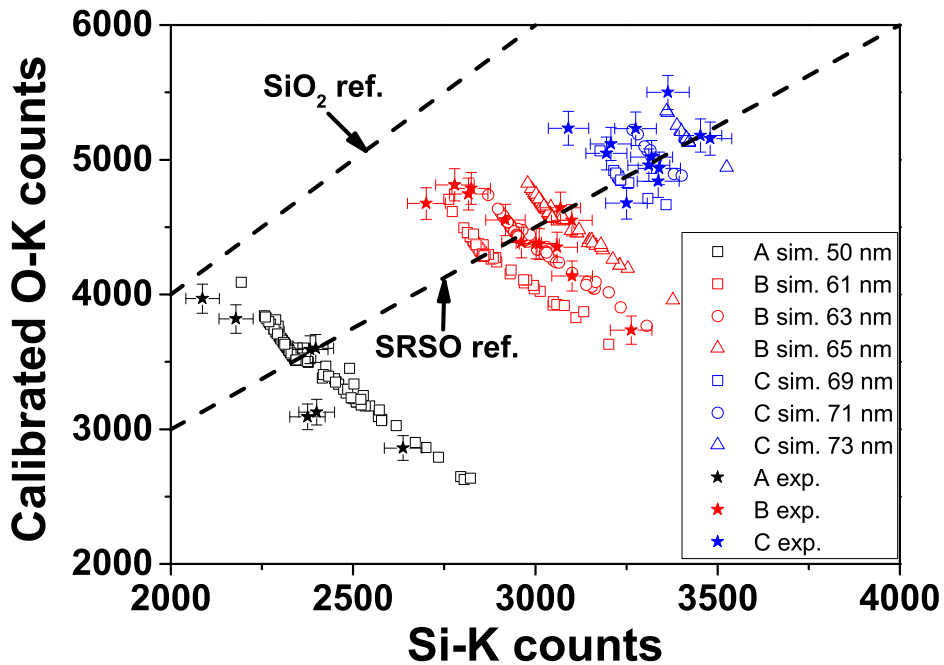


Figure 5.7: The comparison between EDX experimental data and EDX simulation based on core shell model. In contrast to area B and C, the compositional fluctuation range of area A is higher than that of area B and C. The simulation results agree well with experimental ones.

The EDX spectra is also collected in area A, B and C. The energy window for O-K

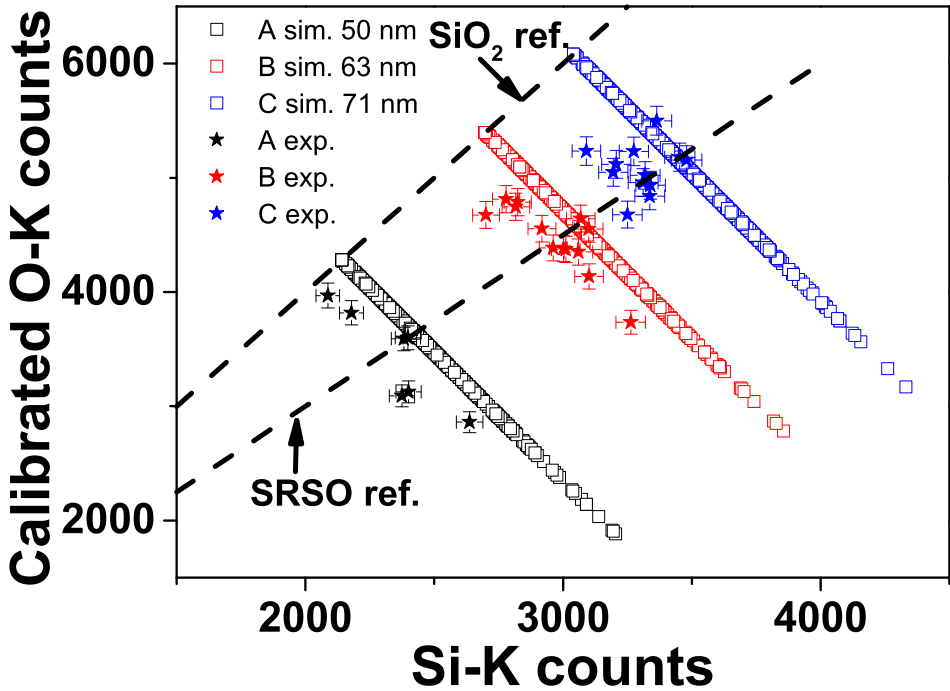


Figure 5.8: The comparison between EDX experimental data and EDX simulation that all SRSO is decomposed into nc-Si particle and SiO₂. The fluctuation range of simulation results is much higher than that of experimental ones.

characteristic X-rays is from 0.42 to 0.62 Kev and the one for Si-K is from 1.62 to 1.84 Kev. The superposition of X-rays counts in these energy windows is used for quantitative EDX analysis. In order to reflect the local composition directly, the O-K counts should be calibrated with the multiplication by k factor. The error bar of X-ray counts is its square root. The correlated results that describes the calibrated O-K counts as a function of Si-K counts are displayed in Fig. 5.7. As mentioned in the experimental section, two dashed lines that represent the SiO₂ and SRSO from the pristine sample are also drawn for comparison. It is clearly observed that the data points locate at three different ranges, which is corresponding to three areas A, B and C. The most interesting stuff is the fluctuation of data points around the SRSO dashed line. In contrast to area A, another interesting phenomenon is that the amplitude of fluctuation in area C is low.

In order to understand this fluctuation, core shell simulation is firstly made. It should be noted that the sample thickness set in simulation is calibrated from

the average Si-K counts in three areas of sample. The corresponding simulation results are also presented in Fig. 5.7. It can be seen that the simulation result agrees well with the experimental one. Another simulation in which all SRSO is consumed to form nc-Si particle and SiO₂ is also made and the corresponding results are presented in Fig. 5.8. The fluctuation range is much larger than that of experimental, in special the range below SRSO ref. dashed line. It can be concluded that only from EDX results Si core SiO₂ shell model is proposed to illustrate the microstructure of nc-Si particle and its surrounding amorphous matrix.

5.5 Discussion

Before we start the section, the most important points and conclusions are firstly summarized.

1. HRTEM results indicates that matrix around nc-Si particle is homogeneous and any second amorphous phase can not be detected here. And this observation consists with the phase separation reaction in Eq. (5.1) and Eq. (5.2).
2. EELS analysis qualitatively reflects that Si nanoparticles are embedded in amorphous SiO₂ matrix.
3. HCDF imaging performs the dominated advantage in particle analysis. The comparison among area A, B and C in Fig. illustrates that the fraction of larger particles in area A is much higher than that in area B and C.
4. The comparison between EDX experiment and simulation states that Si core SiO₂ shell model is proposed to reflect the corresponding microstructure.

Due to the weak heterogeneity between SRSO and SiO₂, it is difficult for HRTEM to provide the chemistry of amorphous matrix. EELS analysis reports that this matrix is SiO₂ qualitatively, which confirms that the Si-SiO₂ nanoscopic phase separation occurs in our materials system. However, the limitation of EELS should be noted. As presented in Fig. 5.3, there is a small energy dirft about 2 ev between SRSO and SRSO, but this difference is quite weak. We can not find any literatures

concerning of EELS that describe the plasmonic peak position as a function of x value of SiO_x , in special some intermediate states between $\text{SiO}_{1.5}$ and SiO_2 . Although SRSO can be decomposed into Si and SiO_2 , the low loss region in EELS of SRSO can not be regarded as the superposition of that of Si and SiO_2 , which has been also confirmed by the state of art sub-nanometer electron diffraction [53]. Thus, the plasmonic peak in EELS may not accurately reflect the chemistry information of amorphous matrix while the qualitative conclusion concerning of matrix composition is still available.

Instead, EDX, which directly measures the local composition, can supply quantitative chemistry information. The agreement between experiments and core shell simulation also supports the nanoscopic phase separation. The fluctuation range in area A is higher than that in area B and C, the main reason stems from bigger fraction of larger particles in area A. As EDX measures the average composition along Z direction of sample and the fluctuation range is more sensitive to the larger particles.

The connection between EELS and EDX results is discussed as follows. It should be noted that there is some unreacted SRSO parts left after core shell model simulation. However, these parts can not be observed in EELS results. The possible reason is that they are also decomposed into Si and SiO_2 and the nc-Si generated is quite small which can not give apparent contribution to fluctuation range in EDX. In other words, EDX may not distinguish small particle embedded in sample from SRSO sample. Another evidence that supports this is that HCDF imaging underestimates the number of particles in contrast to EELS spectrum imaging. Because some of particles in special small ones, which are out of diffraction in HCDF, can not be displayed and instead they can be imaged by EELS.

5.6 Conclusion and Outlook

In this paper, we employ a series of TEM correlated techniques like HCDF, HRTEM, EELS and EDX to investigate the phase separation in CW laser irradiated substrate bound SRSO samples. The macroscopic phase separation in CW laser irradiated SRSO films can not be evidenced by our previous study, which switches our focus to the Si-SiO₂ at nanoscale. The HRTEM technique

with a spatial resolution of 0.19 nm indicates the amorphous matrix around nc-Si particles is homogeneous. EELS and EDX analysis conclude that the Si-SiO₂ nanoscopic phase separation occurs in our materials system. Future work can be expected in the model refinement for EDX simulation.

6 General discussion and Summary

In this thesis, silicon rich silicon oxide (SRSO) is irradiated by continuous wave laser and its related optical and structural properties are systematically studied by a series of characterization methods: AFM, micro-Raman, micro-PL, HCDF, HRTEM, EDX and EELS. The thesis intends to give one comprehensive understanding of the microstructures in CW laser irradiated SRSO samples and related kinetics of materials. The content of chapter 1 to 5 will be summarized as follows.

Chapter 1, as the introduction of this thesis, firstly describes some basic knowledge in this field. For instance, difficult situations of silicon photonics concerning of light emission efficiency and they potential reasons are indicated. After that, the initial experimental results on room-temperature photoluminescence (RT PL) based on porous silicon is shortly presented and the concept of quantum confinement (QC) effect is introduced to understand the RT PL. And the reasons we select silicon nanocrystals embedded in SiO_2 not porous silicon or other low dimensional silicon systems are explained. Except for QC, other PL mechanisms proposed by researchers are also mentioned. As SRSO is the main precursor to obtain nc-Si particles in this thesis, the structures and properties of SRSO are shortly reviewed. Since CW laser irradiation is the dominated fabrication method, some knowledge of light solid interactions is presented. An overview of different characterization methods in both literature and this thesis is shown. Secondly, selected typical investigations on micro-structural evolution in SRSO samples by annealing is reviewed. Thermal annealing is the usual way to induce Si-SiO₂ phase separation in SRSO, however, its limitation in coupling Si photonics with Si electronics is apparent. Instead, laser annealing performs great advantages for this. The time scale of nc-Si particles generation for these two methods is different (1h for thermal annealing, 20 ms for laser annealing), which draw our focus on the microstructural evolution of irradiated SRSO samples. Especially, a recent study on macroscopic Si-SiO₂ phase separation by CW laser annealing stimulated us to give a comprehensive study on related microstructures by advanced TEM methods. At the

end of this chapter, main contributions of our work are stated and their related physical meanings are discussed, which also provides a guide to the content of main chapters in the thesis.

Chapter 2, as a preliminary study of optical and structural properties, intends to provide the overall information of samples. The association of micro-PL with micro-Raman basically indicates the potential components (a-Si, nc-Si particle) that are responsible to the luminescence. And spatially resolved microstructure by HCDF imaging is initially presented. In addition, we have shown that a damage-free laser irradiation can be obtained in substrate-bound SRSO samples by optimized parameters.

Chapter 3 and 4 mainly focus on the formation of porous silicon oxide mentioned in chapter 2. The kinetics process of porous are studied from several evidences in variation of parameters like laser intensity, irradiation time. TEM tomography and EDX mapping indicates that these structures have the porous character. Further EDX and EELS investigations show that porous structure is chemically close to SiO_2 in a qualitative way. The systematical analysis of TEM evidence in formation of porous indicates the related kinetics as follows: (a). silicon nanocrystals is preformed; (b) ripening effect dominates the following nc-Si growth; (c) intensive light absorption in nc-Si leads to the depletion of nc-Si and after that the sponge-like SiO_2 network is formed.

Chapter 5 mainly investigates the phase separation process in SRSO concerning of the formation of nc-Si particles. Our results can not provide the evidence of macroscopic phase separation in previous study. The EELS results, quantitative EDX study combined with simulation indicate that nanoscopic Si-SiO₂ mainly occurs in our materials system. This study expand EDX to a new way to investigate the phase separation in irradiated SRSO samples.

This thesis has explored almost all the microstructures formed in CW laser irradiated SRSO samples mainly based on the advanced characterization methods like TEM and the related techniques. Future work can be expected in several aspects as follows: 1) the internal relationship between different microstructures (ie. porous and nc-Si) is worth to be studied and some unknown kinetics process may be probed by in-situ TEM investigation during laser irradiation; 2) the potential properties of porous silicon oxide should be interesting (ie. application in wave-

guides) and laser induced porous may provide a accurate way of structure control in contrast to normal chemically etching methods; 3) structure models for EDX simulation can be refined based on experimental data and a model that approaches the real system is supposed.

Bibliography

- [1] J. R. Chelikowsky and M. L. Cohen. Nonlocal pseudopotential calculations for the electronic structure of eleven diamond and zinc-blende semiconductors. *Physical Review B*, 14:556–582, 1976.
- [2] L. C. Kimerling, K. D. Kolenbrander, J. Michel, and J. Palm. *Solid state physics; volume 50*. Academic Press, Boston, 1997.
- [3] J. I. Pankove. *Optical processes in semiconductors*. Dover, New York, 1971.
- [4] L. T. Canham. Silicon quantum wire array fabrication by electrochemical and chemical dissolution of wafers. *Applied Physics Letters*, 57(10):1046–1048, 1990.
- [5] A. G. Cullis and L. T. Canham. Visible light emission due to quantum size effects in highly porous crystalline silicon. *Nature*, 353(6342):335–338, 1991.
- [6] S. Gardelis, J. S. Rimmer, P. Dawson, B. Hamilton, R. A. Kubiak, T. E. Whall, and E. H. C. Parker. Evidence for quantum confinement in the photoluminescence of porous Si and SiGe. *Applied Physics Letters*, 59(17):2118–2120, 1991.
- [7] A. Bsiesy, J. C. Vial, F. Gaspard, R. Herino, M. Ligeon, F. Muller, R. Romestain, A. Wasieła, A. Halimaoui, and G. Bomchil. Photoluminescence of high porosity and of electrochemically oxidized porous silicon layers. *Surface Science*, 254(1-3):195–200, 1991.
- [8] A. D. Yoffe. Low-dimensional systems: quantum size effects and electronic properties of semiconductor microcrystallites (zero-dimensional systems) and some quasi-two-dimensional systems. *Advances in Physics*, 42(2):173–

262, 1993.

- [9] C Delerue, G Allan, and M Lannoo. Theoretical aspects of the luminescence of porous silicon. *Physical Review B*, 48(15):11024, 1993.
- [10] S. Ögüt, J. R. Chelikowsky, and S. G. Louie. Quantum confinement and optical gaps in Si nanocrystals. *Physical Review Letters*, 79(9):1770, 1997.
- [11] O. Bisi, S. Ossicini, and L. Pavesi. Porous silicon: a quantum sponge structure for silicon based optoelectronics. *Surface Science Reports*, 38(1):1 – 126, 2000.
- [12] G. G. Qin and Y. Q. Jia. Mechanism of the visible luminescence in porous silicon. *Solid State Communications*, 86(9):559 – 563, 1993.
- [13] S. M. Prokes. Light emission in thermally oxidized porous silicon: evidence for oxide-related luminescence. *Applied Physics Letters*, 62(25):3244–3246, 1993.
- [14] Z. Y. Xu, M. Gal, and M. Gross. Photoluminescence studies on porous silicon. *Applied Physics Letters*, 60(11):1375–1377, 1992.
- [15] F. Koch, V. Petrova-Koch, T. Muschik, A. Nikolov, and V. Gavrilenko. Some perspectives on the luminescence mechanism via surface-confined states of porous Si. *MRS Proceedings*, 283:–, 1992.
- [16] Z. H. Lu, D. J. Lockwood, and J. M. Baribeau. Quantum confinement and light emission in SiO₂/Si superlattices. *Nature*, 378(6554):258, 1995.
- [17] Y. Takahashi, T. Furuta, Y. Ono, T. Ishiyama, and M. Tabe. Photoluminescence from a silicon quantum well formed on separation by implanted oxygen substrate. *Japanese Journal of Applied Physics*, 34(2S):950, 1995.
- [18] Y. Kanemitsu and S. Okamoto. Photoluminescence from Si/SiO₂ single quantum wells by selective excitation. *Physical Review B*, 56:R15561–R15564, Dec 1997.

-
- [19] L. Khriachtchev, M. Räsänen, S. Novikov, O. Kilpelä, and J. Sinkkonen. Raman scattering from very thin Si layers of Si/SiO₂ superlattices: experimental evidence of structural modification in the 0.8–3.5 nm thickness region. *Journal of Applied Physics*, 86(10):5601–5608, 1999.
- [20] Y. Kanzawa, T. Kageyama, S. Takeoka, M. Fujii, S. Hayashi, and K. Yamamoto. Size-dependent near-infrared photoluminescence spectra of Si nanocrystals embedded in SiO₂ matrices. *Solid State Communications*, 102(7):533–537, 1997.
- [21] S. Schuppler, S. L. Friedman, M. A. Marcus, D. L. Adler, Y. H. Xie, F. M. Ross, Y. J. Chabal, T. D. Harris, L. E. Brus, and W. L. Brown. Size, shape, and composition of luminescent species in oxidized Si nanocrystals and H-passivated porous Si. *Physical Review B*, 52(7):4910, 1995.
- [22] H. Takagi, H. Ogawa, Y. Yamazaki, A. Ishizaki, and T. Nakagiri. Quantum size effects on photoluminescence in ultrafine Si particles. *Applied Physics Letters*, 56(24):2379–2380, 1990.
- [23] S. Guha, S. B. Qadri, R. G. Musket, M. A. Wall, and T. Shimizu-Iwayama. Characterization of si nanocrystals grown by annealing SiO₂ films with uniform concentrations of implanted Si. *Journal of Applied Physics*, 88(7):3954–3961, 2000.
- [24] T. Takagahara and K. Takeda. Theory of the quantum confinement effect on excitons in quantum dots of indirect-gap materials. *Physical Review B*, 46(23):15578, 1992.
- [25] L. W. Wang and A. Zunger. Electronic structure pseudopotential calculations of large (. appr. 1000 atoms) Si quantum dots. *The Journal of Physical Chemistry*, 98(8):2158–2165, 1994.
- [26] C. Garcia, B. Garrido, P. Pellegrino, R. Ferre, J. A. Moreno, J. R. Morante, L. Pavesi, and M. Cazzanelli. Size dependence of lifetime and absorption cross section of Si nanocrystals embedded in SiO₂. *Applied Physics Letters*, 82(10):1595–1597, 2003.

- [27] D. Nesheva, C. Raptis, A. Perakis, I. Bineva, Z. Aneva, Z. Levi, S. Alexandrova, and H. Hofmeister. Raman scattering and photoluminescence from Si nanoparticles in annealed SiO_x thin films. *Journal of Applied Physics*, 92(8):4678–4683, 2002.
- [28] R. B. Wehrspohn, J. N. Chazalviel, F. Ozanam, and I. Solomon. Conditions of elaboration of luminescent porous silicon from hydrogenated amorphous silicon. *Physical Review Letters*, 77(9):1885, 1996.
- [29] S. A. Koehler. Search for quantum confinement effects in ultrathin layers of hydrogenated amorphous silicon. *Philosophical Magazine B*, 77(1):27–48, 1998.
- [30] B. Averboukh, R. Huber, K. W. Cheah, Y. R. Shen, G. G. Qin, Z. C. Ma, and W. H. Zong. Luminescence studies of a Si/SiO₂ superlattice. *Journal of applied physics*, 92(7):3564–3568, 2002.
- [31] C. S. Garoufalis and A. D. Zdetsis. High accuracy calculations of the optical gap and absorption spectrum of oxygen contaminated Si nanocrystals. *Physical Chemistry Chemical Physics*, 8(7):808–813, 2006.
- [32] S. Godefroo, M. Hayne, M. Jivanescu, A. Stesmans, M. Zacharias, O. I. Lebedev, G. Van Tendeloo, and V. V. Moshchalkov. Classification and control of the origin of photoluminescence from Si nanocrystals. *Nature Nanotechnology*, 3(3):174–178, 2008.
- [33] K. S. Zhuravlev, A. M. Gilinsky, and A. Y. Kobitsky. Mechanism of photoluminescence of Si nanocrystals fabricated in a SiO₂ matrix. *Applied Physics Letters*, 73(20):2962–2964, 1998.
- [34] B. Garrido Fernandez, M. Lopez, C. Garcia, A. Pérez-Rodríguez, J. R. Morante, C. Bonafos, M. Carrada, and A. Claverie. Influence of average size and interface passivation on the spectral emission of Si nanocrystals embedded in SiO₂. *Journal of Applied Physics*, 91(2):798–807, 2002.
- [35] Y. Kanemitsu, T. Ogawa, K. Shiraishi, and K. Takeda. Visible photoluminescence from oxidized Si nanometer-sized spheres: exciton confinement on

-
- a spherical shell. *Physical Review B*, 48(7):4883, 1993.
- [36] Y. Kanemitsu, H. Uto, Y. Masumoto, T. Matsumoto, T. Futagi, and H. Mimura. Microstructure and optical properties of free-standing porous silicon films: size dependence of absorption spectra in Si nanometer-sized crystallites. *Physical Review B*, 48(4):2827, 1993.
- [37] C. TERNON, C. DUFOUR, F. GOURBILLEAU, and R. RIZK. Roles of interfaces in nanostructured silicon luminescence. *The European Physical Journal B-Condensed Matter and Complex Systems*, 41(3):325–332, 2004.
- [38] N. TOMOZEIU. *Silicon oxide (SiO_x , $0 < x < 2$): a challenging material for optoelectronics, optoelectronics - materials and techniques*. InTech, 2011.
- [39] W. H. ZACHARIASEN. The atomic arrangement in glass. *Journal of the American Chemical Society*, 54(10):3841–3851, 1932.
- [40] S. KOHARA and K. SUZUYA. Intermediate-range order in vitreous SiO_2 and GeO_2 . *Journal of Physics: Condensed Matter*, 17(5):S77, 2005.
- [41] P. VASHISHTA, R. K. KALIA, J. P. RINO, and I. EBBJSJÖ. Interaction potential for SiO_2 : a molecular-dynamics study of structural correlations. *Physical Review B*, 41:12197–12209, 1990.
- [42] R. L. MOZZI and B. E. WARREN. The structure of vitreous silica. *Journal of Applied Crystallography*, 2(4):164–172, Oct 1969.
- [43] M. ISHIMARU. Molecular-dynamics study on atomistic structures of amorphous silicon. *Journal of Physics: Condensed Matter*, 13(19):4181, 2001.
- [44] K. LAAZIRI, S. KYCIA, S. ROORDA, M. CHICOINE, J. L. ROBERTSON, J. WANG, and S. C. MOSS. High resolution radial distribution function of pure amorphous silicon. *Physical Review Letters*, 82:3460–3463, 1999.
- [45] R. CAR and M. PARRINELLO. Structural, dynamical, and electronic properties of amorphous silicon: an ab initio molecular-dynamics study. *Physical Review Letters*, 60:204–207, 1988.

- [46] G. N. Greaves. EXAFS and the structure of glass. *Journal of Non-Crystalline Solids*, 71(1):203 – 217, 1985.
- [47] A. Hohl, T. Wieder, P. A. van Aken, T. E. Weirich, G. Denninger, M. Vidal, S. Oswald, C. Deneke, J. Mayer, and H. Fuess. An interface clusters mixture model for the structure of amorphous silicon monoxide (SiO). *Journal of Non-Crystalline Solids*, 320(1):255 – 280, 2003.
- [48] H. Sepehri-Amin, T. Ohkubo, M. Kodzuka, H. Yamamura, T. Saito, H. Iba, and K. Hono. Evidence for nano-si clusters in amorphous sio anode materials for rechargeable Li-ion batteries. *Scripta Materialia*, 69(1):92–95, 2013.
- [49] K. Schulmeister and W. Mader. TEM investigation on the structure of amorphous silicon monoxide. *Journal of Non-Crystalline Solids*, 320(1–3):143–150, 2003.
- [50] A. Hirata, P. F. Guan, T. Fujita, Y. Hirotsu, A. Inoue, A. R. Yavari, T. Sakurai, and M. W. Chen. Direct observation of local atomic order in a metallic glass. *Nature Materials*, 10(1):28–33, 2011.
- [51] A. Hirata and M. W. Chen. Angstrom-beam electron diffraction of amorphous materials. *Journal of Non-Crystalline Solids*, 383:52 – 58, 2014. The {XIII} International Conference on the Physics of Non-Crystalline Solids.
- [52] A. Hirata, L. J. Kang, T. Fujita, B. Klumov, K. Matsue, M. Kotani, A. R. Yavari, and M. W. Chen. Geometric frustration of icosahedron in metallic glasses. *Science*, 341(6144):376–379, 2013.
- [53] A. Hirata, S. Kohara, T. Asada, M. Arao, C. Yogi, H. Imai, Y. W Tan, T. Fujita, and M. W. Chen. Atomic-scale disproportionation in amorphous silicon monoxide. *Nature Communications*, 7:11591–, 2016.
- [54] N. M. Ravindra, S. Auluck, and V. K. Srivastava. On the penn gap in semiconductors. *Physica Status Solidi (b)*, 93(2):K155–K160, 1979.
- [55] J. Tauc, R. Grigorovici, and A. Vancu. Optical properties and electronic structure of amorphous germanium. *Physica Status Solidi (b)*, 15(2):627–

637, January 1966.

- [56] G. D. Cody, T. Tiedje, B. Abeles, B. Brooks, and Y. Goldstein. Disorder and the optical-absorption edge of hydrogenated amorphous silicon. *Physical Review Letters*, 47:1480–1483, Nov 1981.
- [57] S. K. O' Leary, S. R. Johnson, and P. K. Lim. The relationship between the distribution of electronic states and the optical absorption spectrum of an amorphous semiconductor: an empirical analysis. *Journal of Applied Physics*, 82(7):3334–3340, 1997.
- [58] N. F. Mott. Conduction in non-crystalline materials. *Philosophical Magazine*, 19(160):835–852, 1969.
- [59] N. Apsley and H. P. Hughes. Temperature- and field-dependence of hopping conduction in disordered systems, ii. *Philosophical Magazine*, 31(6):1327–1339, 1975.
- [60] J. J. van Hapert. *Hopping conduction and chemical structure: a study on silicon suboxides*. PhD thesis, 2002.
- [61] J. Yang, Y. Takeda, N. Imanishi, C. Capiglia, J. Y. Xie, and O. Yamamoto. SiO_x-based anodes for secondary lithium batteries. *Solid State Ionics*, 152:125–129, 2002.
- [62] Y. Nagao, H. Sakaguchi, H. Honda, T. Fukunaga, and T. Esaka. Structural analysis of pure and electrochemically lithiated SiO using neutron elastic scattering. *Journal of The Electrochemical Society*, 151(10):A1572–A1575, 2004.
- [63] C. M. Park, W. Choi, Y. Hwa, J. H. Kim, G. Jeong, and H. J. Sohn. Characterizations and electrochemical behaviors of disproportionated SiO and its composite for rechargeable Li-ion batteries. *Journal of Materials Chemistry*, 20(23):4854–4860, 2010.
- [64] M. Yamada, A. Inaba, A. Ueda, K. Matsumoto, T. Iwasaki, and T. Ohzuku. Reaction mechanism of α -SiO₂-carbon composite-negative electrode for high-

- capacity lithium-ion batteries. *Journal of The Electrochemical Society*, 159(10):A1630–A1635, 2012.
- [65] N. F. Mott and E. A. Davis. Conduction in non-crystalline systems. Part V. *Philosophical Magazine*, 22:903, 1970.
- [66] D. L. Staebler and C. R. Wronski. Reversible conductivity changes in discharge-produced amorphous si. *Applied physics letters*, 31(4):292–294, 1977.
- [67] D. L. Staebler and C. R. Wronski. Optically induced conductivity changes in discharge-produced hydrogenated amorphous silicon. *Journal of Applied Physics*, 51(6):3262–3268, 1980.
- [68] A. Janotta, Y. Dikce, M. Schmidt, C. Eisele, M. Stutzmann, M. Luysberg, and L. Houben. Light-induced modification of a-SiO_x II: laser crystallization. *Journal of Applied Physics*, 95(8):4060–4068, 2004.
- [69] J. X. Yu, X. Xiang, S. B. He, X. D. Yuan, W. G. Zheng, H. B. Lü, and X. T. Zu. Laser-induced damage initiation and growth of optical materials. *Advances in Condensed Matter Physics*, 2014, 2014.
- [70] C. J. Lin, G. R. Lin, Y. L. Chueh, L. J. Chou, et al. Analysis of silicon nanocrystals in silicon-rich SiO₂ synthesized by CO₂ laser annealing-art. no. 602020. In *Optoelectronic Materials and Devices for Optical Communications*, volume 6020, pages 2020–2020, 2005.
- [71] B. Gallas, C. C. Kao, S. Fisson, G. Vuye, J. Rivory, Y. Bernard, and C. Belouet. Laser annealing of SiO_x thin films. *Applied Surface Science*, 185(3):317–320, 2002.
- [72] N. Wang, T. Fricke-Begemann, P. Peretzki, K. Thiel, J. Ihlemann, and M. Seibt. Microstructural analysis of the modifications in substrate-bound silicon-rich silicon oxide induced by continuous wave laser irradiation. *Journal of Alloys and Compounds*, 707:227–232, 2017.
- [73] M. Balkanski, R. F. Wallis, and E. Haro. Anharmonic effects in light scat-

-
- tering due to optical phonons in silicon. *Physical Review B*, 28(4):1928, 1983.
- [74] L. Khriachtchev, M. Räsänen, and S. Novikov. Continuous-wave laser annealing of free-standing Si/SiO₂ superlattice: modification of optical, structural, and light-emitting properties. *Journal of Applied Physics*, 100(5):053502, 2006.
- [75] E. Teng, W. Goh, and A. Eltouhky. Laser zone texture on alternative substrate disks. *IEEE Transactions on Magnetics*, 32(5):3759–3761, 1996.
- [76] A. C. Tam, J. Brannon, P. Baumgart, and I. K. Pour. Laser texturing of glass disk substrates. *IEEE Transactions on Magnetics*, 33(5):3181–3183, 1997.
- [77] D. Kuo, S. D. Vierk, O. Rauch, and D. Polensky. Laser zone texturing on glass and glass-ceramic substrates. *IEEE Transactions on Magnetics*, 33(1):944–949, 1997.
- [78] G. C. Rauch, J. J. Liu, S. Y. Lee, I. Boszormenyi, C. Gao, J. Gui, D. Kuo, B. Marchon, S. Vierk, and R. Malmhall. Glass-ceramic substrates for 1 Gb/in² and beyond. *IEEE Transactions on Magnetics*, 32(5):3642–3647, 1996.
- [79] T. R. Shiu, C. P. Grigoropoulos, and R. Greif. Measurement of the transient glass surface deformation during laser heating. *Journal of Heat Transfer*, 121(4):1042–1048, 1999.
- [80] T. R. Shiu, C. P. Grigoropoulos, D. G. Cahill, and R. Greif. Mechanism of bump formation on glass substrates during laser texturing. *Journal of Applied Physics*, 86(3):1311–1316, 1999.
- [81] H. Koyama and P. M. Fauchet. Very large continuous-wave-laser-induced optical absorption in porous silicon films: evidence for thermal effects. *Applied Physics Letters*, 73(22):3259–3261, 1998.
- [82] D. J. H. Cockayne. The study of nanovolumes of amorphous materials using

- electron scattering. *Annual Review of Materials Research*, 37:159–187, 2007.
- [83] L. Khriachtchev, T. Nikitin, C. J. Oton, R. Velagapudi, J. Sainio, J. Lahtinen, and S. Novikov. Optical properties of silicon nanocrystals in silica: results from spectral filtering effect, m-line technique, and x-ray photoelectron spectroscopy. *Journal of Applied Physics*, 104(10):104316, 2008.
- [84] B. J. Hinds, F. Wang, D. M. Wolfe, C. L. Hinkle, and G. Lucovsky. Investigation of postoxidation thermal treatments of Si/SiO₂ interface in relationship to the kinetics of amorphous Si suboxide decomposition. *Journal of Vacuum Science & Technology B: Microelectronics and Nanometer Structures Processing, Measurement, and Phenomena*, 16(4):2171–2176, 1998.
- [85] L. Khriachtchev, T. Nikitin, M. Räsänen, A. Domanskaya, S. Boninelli, F. Iacona, A. Engdahl, J. Juhanaja, and S. Novikov. Continuous-wave laser annealing of Si-rich oxide: a microscopic picture of macroscopic Si–SiO₂ phase separation. *Journal of Applied Physics*, 108(12):124301, 2010.
- [86] L. Khriachtchev, S. Ossicini, F. Iacona, and F. Gourbilleau. Silicon nanoscale materials: from theoretical simulations to photonic applications. *International Journal of Photoenergy*, page Article ID 872576, 2012.
- [87] F. Iacona, G. Franzò, and C. Spinella. Correlation between luminescence and structural properties of Si nanocrystals. *Journal of Applied Physics*, 87(3):1295–1303, 2000.
- [88] C. Bonafos, B. Colombeau, A. Altibelli, M. Carrada, G. B. Assayag, B. Garrido, M. López, A. Pérez-Rodríguez, J. R. Morante, and A. Claverie. Kinetic study of group iv nanoparticles ion beam synthesized in SiO₂. *Nuclear Instruments and Methods in Physics Research Section B: Beam Interactions with Materials and Atoms*, 178(1):17–24, 2001.
- [89] T. Fricke-Begemann, N. Wang, P. Peretzki, M. Seibt, and J. Ihlemann. Generation of silicon nanocrystals by damage free continuous wave laser annealing of substrate-bound SiO_x films. *Journal of Applied Physics*, 118(12):124308, 2015.

-
- [90] C. Bonafos, B. Garrido, M. Lopez, A. Perez-Rodriguez, J. R. Morante, Y. Kihn, G. B. Assayag, and A. Claverie. An electron microscopy study of the growth of Ge nanoparticles in SiO₂. *Applied Physics Letters*, 76(26):3962–3964, 2000.
- [91] J. O. Malm and M. A. O’keefe. Deceptive lattice spacings in high-resolution micrographs of metal nanoparticles. *Ultramicroscopy*, 68(1):13–23, 1997.
- [92] F. Iacona, C. Bongiorno, C. Spinella, S. Boninelli, and F. Priolo. Formation and evolution of luminescent Si nanoclusters produced by thermal annealing of SiO_x films. *Journal of Applied Physics*, 95(7):3723–3732, 2004.
- [93] H. S. Nalwa. *Encyclopedia of nanoscience and nanotechnology; Volume 7*. American Scientific Publishers, 2004.
- [94] S. Gardelis, A. G. Nassiopoulou, P. Manousiadis, S. Milita, A. Gkanatsiou, N. Frangis, and C. B. Lioutas. Structural and optical characterization of two-dimensional arrays of si nanocrystals embedded in SiO₂ for photovoltaic applications. *Journal of Applied Physics*, 111(8):083536, 2012.
- [95] S. Gardelis, A. G. Nassiopoulou, N. Vouroutzis, and N. Frangis. Effect of exciton migration on the light emission properties in silicon nanocrystal ensembles. *Journal of Applied Physics*, 105(11):113509, 2009.
- [96] W. M. Arnoldbik, N. Tomozeiu, E. D. Van Hattum, R. W. Lof, A. M. Vredenberg, and F. H. P. M. Habraken. High-energy ion-beam-induced phase separation in SiO_x films. *Physical Review B*, 71(12):125329, 2005.
- [97] G. Lucovsky and W. B. Pollard. Local bonding of oxygen and hydrogen in a-Si: H: O thin films. *Journal of Vacuum Science & Technology A: Vacuum, Surfaces, and Films*, 1(2):313–316, 1983.
- [98] J. C. Knights, R. A. Street, and G. Lucovsky. Electronic and structural properties of plasma-deposited a-Si: O: H-The story of O₂. *Journal of Non-Crystalline Solids*, 35:279–284, 1980.

- [99] P. G. Pai, S. S. Chao, Y. Takagi, and G. Lucovsky. Infrared spectroscopic study of SiO_x films produced by plasma enhanced chemical vapor deposition. *Journal of Vacuum Science & Technology A: Vacuum, Surfaces, and Films*, 4(3):689–694, 1986.
- [100] R. J. Bell and P. Dean. Atomic vibrations in vitreous silica. *Discussions of the Faraday society*, 50:55–61, 1970.
- [101] F. L. Galeener and G. Lucovsky. Longitudinal optical vibrations in glasses: GeO_2 and SiO_2 . *Physical Review Letters*, 37(22):1474, 1976.
- [102] G. Lucovsky, C. K. Wong, and W. B. Pollard. Vibrational properties of glasses: intermediate range order. *Journal of Non-Crystalline Solids*, 59:839–846, 1983.
- [103] J. A. Luna-López, J. Carrillo-López, M. Aceves-Mijares, A. Morales-Sánchez, and C. Falcony. FTIR and photoluminescence of annealed silicon rich oxide films. *Superficies y vacío*, 22(1):11–14, 2009.
- [104] D. V. Tsu, G. Lucovsky, and B. N. Davidson. Effects of the nearest neighbors and the alloy matrix on SiH stretching vibrations in the amorphous SiO_r : H ($0 < r < 2$) alloy system. *Physical Review B*, 40(3):1795, 1989.
- [105] M. Avrami. Kinetics of phase change. i general theory. *The Journal of Chemical Physics*, 7(12):1103–1112, 1939.
- [106] M. Avrami. Kinetics of phase change. ii transformation-time relations for random distribution of nuclei. *The Journal of Chemical Physics*, 8(2):212–224, 1940.
- [107] M. Avrami. Granulation, phase change, and microstructure kinetics of phase change. iii. *The Journal of chemical physics*, 9(2):177–184, 1941.
- [108] J. F. Moulder, W. F. Stickle, P. E. Sobol, and K. D. Bomben. Handbook of X-ray photoelectron spectroscopy. *Perkin-Elmer, Eden Prairie, MN*, 52, 1992.

-
- [109] P. M. Fauchet. The Raman microprobe: a quantitative analytical tool to characterize laser-processed semiconductors. *IEEE Circuits and Devices Magazine*, 2(1):37–43, 1986.
- [110] L. A. Nesbit. Annealing characteristics of Si-rich SiO₂ films. *Applied Physics Letters*, 46(1):38–40, 1985.
- [111] T. Shimizu-Iwayama, Y. Terao, A. Kamiya, M. Takeda, S. Nakao, and K. Saitoh. Novel approach for synthesizing of nanometer-sized si crystals in SiO₂ by ion implantation and their optical characterization. *Nuclear Instruments and Methods in Physics Research Section B: Beam Interactions with Materials and Atoms*, 112(1-4):214–218, 1996.
- [112] T. Shimizu-Iwayama, N. Kurumado, D. E. Hole, and P. D. Townsend. Optical properties of silicon nanoclusters fabricated by ion implantation. *Journal of Applied Physics*, 83(11):6018–6022, 1998.
- [113] F. Rochet, G. Dufour, H. Roulet, B. Pelloie, J. Perriere, E. Fogarassy, A. Slaoui, and M. Froment. Modification of SiO through room-temperature plasma treatments, rapid thermal annealings, and laser irradiation in a nonoxidizing atmosphere. *Physical Review B*, 37(11):6468, 1988.
- [114] D. Cha, J. H. Shin, I. H. Song, and M. K. Han. Enhanced formation of luminescent nanocrystal Si embedded in si/SiO₂ superlattice by excimer laser irradiation. *Applied physics letters*, 84(8):1287–1289, 2004.
- [115] N. Tomozeiu. Effects of UV photon irradiation on SiO_x (0<x<2) structural properties. *Applied Surface Science*, 253(1):376–380, 2006.
- [116] W. Mustafeez, D. Lee, C. Grigoropoulos, and A. Salleo. Precipitation of silicon nanoclusters by laser direct-write. *Optics Express*, 19(16):15452–15458, 2011.
- [117] M. O. Thompson, G. J. Galvin, J. W. Mayer, P. S. Peercy, J. M. Poate, D. C. Jacobson, A. G. Cullis, and N. G. Chew. Melting temperature and explosive crystallization of amorphous silicon during pulsed laser irradiation. *Physical Review Letters*, 52(26):2360, 1984.

- [118] M. C. Rossi, S. Salvatori, M. Burchielli, and G. Conte. Optical and electrical properties of silicon nanocrystals formed by CW laser irradiation of amorphous silicon oxides. *Thin Solid Films*, 383(1):267–270, 2001.
- [119] M. C. Rossi, S. Salvatori, F. Galluzzi, and G. Conte. Laser-induced nanocrystalline silicon formation in a-SiO matrices. *Materials Science and Engineering: B*, 69:299–302, 2000.
- [120] Z. Iqbal, S. Vepřek, A. P. Webb, and P. Capezzuto. Raman scattering from small particle size polycrystalline silicon. *Solid State Communications*, 37(12):993–996, 1981.
- [121] L. Khriachtchev, M. Räsänen, and S. Novikov. Free-standing silica film containing Si nanocrystals: photoluminescence, raman scattering, optical waveguiding, and laser-induced thermal effects. *Applied Physics Letters*, 86(14):141911, 2005.
- [122] H. Koyama and P. M. Fauchet. Laser-induced thermal effects on the optical properties of free-standing porous silicon films. *Journal of Applied Physics*, 87(4):1788–1794, 2000.
- [123] L. Khriachtchev, M. Räsänen, S. Novikov, and J. Lahtinen. Tunable wavelength-selective waveguiding of photoluminescence in Si-rich silica optical wedges. *Journal of Applied Physics*, 95(12):7592–7601, 2004.
- [124] K. Wada, A. Suzuki, H. Sato, and R. Kikuchi. Soret effect in solids. *Journal of Physics and Chemistry of Solids*, 46(10):1195–1205, 1985.
- [125] K. J. Zhang, M. E. Briggs, R. W. Gammon, and J. V. Sengers. Optical measurement of the Soret coefficient and the diffusion coefficient of liquid mixtures. *The Journal of Chemical Physics*, 104(17):6881–6892, 1996.
- [126] L. Khriachtchev. *Silicon nanophotonics: basic principles, current status and perspectives*. Pan Stanford Publishing, 2009.
- [127] L. Pavesi and R. Turan. *Silicon nanocrystals: fundamentals, synthesis and applications*. John Wiley & Sons, 2010.

-
- [128] U. Kahler and H. Hofmeister. Visible light emission from Si nanocrystalline composites via reactive evaporation of SiO. *Optical Materials*, 17(1):83–86, 2001.
- [129] J. M. Lackner, W. Waldhauser, R. Ebner, W. Lenz, C. Suess, G. Jakopic, G. Leising, and H. Hutter. Pulsed laser deposition: a new technique for deposition of amorphous SiO_x thin films. *Surface and Coatings Technology*, 163:300–305, 2003.
- [130] T. Nikitin, K. Aitola, S. Novikov, M. Räsänen, R. Velagapudi, J. Sainio, J. Lahtinen, K. Mizohata, T. Ahlgren, and L. Khriachtchev. Optical and structural properties of silicon-rich silicon oxide films: comparison of ion implantation and molecular beam deposition methods. *Physica Status Solidi (a)*, 208(9):2176–2181, 2011.
- [131] L. X. Yi, J. Heitmann, R. Scholz, and M. Zacharias. Si rings, Si clusters, and Si nanocrystals—different states of ultrathin SiO_x layers. *Applied Physics Letters*, 81(22):4248–4250, 2002.
- [132] L. X. Yi, R. Scholz, and M. Zacharias. Size and density control of Si-nanocrystals realized by SiO_x/SiO₂ superlattice. *Journal of Luminescence*, 122:750–752, 2007.
- [133] L. Pavesi, L. Dal Negro, C. Mazzoleni, G. Franzo, and F. Priolo. Optical gain in silicon nanocrystals. *Nature*, 408(6811):440, 2000.
- [134] Leonid Khriachtchev, Timur Nikitin, Rama Velagapudi, Jouko Lahtinen, and Sergei Novikov. Light-emission mechanism of thermally annealed silicon-rich silicon oxide revisited: What is the role of silicon nanocrystals? *Applied Physics Letters*, 94(4):043115, 2009.
- [135] R. A. B. Devine and G. Auvert. Photoassisted oxidation of amorphous SiO_x. *Applied physics letters*, 49(23):1605–1607, 1986.
- [136] G-R Lin, C-J Lin, L-J Chou, and Y-L Chueh. Microphotoluminescence and microphotorefectance analyses of *hboxco_2* laser rapid-thermal-annealed *hboxsio_x* surface with buried si nanocrystals. *IEEE transactions on nan-*

- otechnology*, 5(5):511–516, 2006.
- [137] S. E. Blum, K. H. Brown, and R. Srinivasan. Photo-oxidation of silicon monoxide to silicon dioxide with pulsed far-ultraviolet (193 nm) laser radiation. *Applied physics letters*, 43(11):1026–1027, 1983.
- [138] T. Nikitin, M. Kemell, E. Puukilainen, S. Boninelli, F.o Iacona, M. Räsänen, M. Ritala, S. Novikov, and L. Khriachtchev. Surface fingerprints of individual silicon nanocrystals in laser-annealed Si/SiO₂ superlattice: evidence of nanoeruptions of laser-pressurized silicon. *Journal of Applied Physics*, 111(12):124302, 2012.
- [139] L. Khriachtchev. Optical and structural properties of silicon nanocrystals and laser-induced thermal effects. *Journal of The Electrochemical Society*, 159(1):K21–K26, 2011.
- [140] T. Nikitin, M. Kemell, E. Puukilainen, M. Räsänen, M. Ritala, S. Novikov, and L. Khriachtchev. Continuous-wave laser annealing of a Si/SiO₂ superlattice: effect of the ambient atmosphere and exposure period. *Science of Advanced Materials*, 6(5):1000–1010, 2014.
- [141] I. D. Wolf. Stress measurements in si microelectronics devices using Raman spectroscopy. *Journal of Raman spectroscopy*, 30(10):877–883, 1999.
- [142] L. Khriachtchev, M. Räsänen, and S. Novikov. Laser-controlled stress of Si nanocrystals in a free-standing Si/SiO₂ superlattice. *Applied Physics Letters*, 88(1):013102, 2006.
- [143] A. T. Voutsas, M. K. Hatalis, J. Boyce, and A. Chiang. Raman spectroscopy of amorphous and microcrystalline silicon films deposited by low-pressure chemical vapor deposition. *Journal of Applied Physics*, 78(12):6999–7006, 1995.
- [144] I. H. Campbell and P. M. Fauchet. The effects of microcrystal size and shape on the one phonon Raman spectra of crystalline semiconductors. *Solid State Communications*, 58(10):739–741, 1986.

-
- [145] J. Gan, Q. Li, Z. G. Hu, W. L. Yu, K. Gao, J. Sun, N. Xu, and J. D. Wu. Study on phase separation in a-SiO_x for Si nanocrystal formation through the correlation of photoluminescence with structural and optical properties. *Applied Surface Science*, 257(14):6145–6151, 2011.
- [146] D. Nesheva. Photoluminescence from SiO_x layers containing amorphous silicon nanoparticles. *physica Status Solidi (a)*, 209(4):746–751, 2012.
- [147] A. R. Wilkinson and R. G. Elliman. Passivation of si nanocrystals in SiO₂: atomic versus molecular hydrogen. *Applied Physics Letters*, 83(26):5512–5514, 2003.
- [148] G. A. Kachurin, S. G. Cherkova, D. V. Marin, R. A. Yankov, and M. Deutschmann. Formation of light-emitting Si nanostructures in SiO₂ by pulsed anneals. *Nanotechnology*, 19(35):355305, 2008.
- [149] R. Q. Zhang, M. W. Zhao, and S. T. Lee. Silicon monoxide clusters: the favorable precursors for forming silicon nanostructures. *Physical Review Letters*, 93(9):095503, 2004.
- [150] X. Y. Chen, Y. F. Lu, Y. H. Wu, B. J. Cho, B. J. Yang, and T. Y. F. Liew. Laser annealing of silicon nanocrystal films prepared by pulsed-laser deposition. *Journal of Vacuum Science & Technology B: Microelectronics and Nanometer Structures Processing, Measurement, and Phenomena*, 22(4):1731–1737, 2004.
- [151] V. R. Bhardwaj, P. B. Corkum, D. M. Rayner, C. Hnatovsky, E. Simova, and R. S. Taylor. Stress in femtosecond-laser-written waveguides in fused silica. *Optics letters*, 29(12):1312–1314, 2004.
- [152] L. Khriachtchev and S. Novikov. Laser-induced thermal effects on Si/SiO₂ free-standing superlattices. *Applied Physics A*, 87(4):761–766, 2007.
- [153] S. Ossicini, L. Pavesi, and F. Priolo. *Light Emitting Silicon for Microphotonics*. Springer, 2003.
- [154] L. Khriachtchev, M. Räsänen, S. Novikov, and J. Sinkkonen. Optical gain

- in Si/SiO₂ lattice: experimental evidence with nanosecond pulses. *Applied Physics Letters*, 79(9):1249–1251, 2001.
- [155] A.D. Smigelkas and E.O. Kirkendall. Zinc diffusion in alpha brass. *Trans. AIME*, 171:130, 1947.
- [156] Robert H. Doremus. Viscosity of silica. *Journal of Applied Physics*, 92(12):7619–7629, 2002.
- [157] T. Mchedlidze, T. Arguirov, S. Kouteva-Arguirova, M. Kittler, R. Rölver, B. Berghoff, D. L. Bätzner, and B. Spangenberg. Light-induced solid-to-solid phase transformation in si nanolayers of Si–sio₂ multiple quantum wells. *Phys. Rev. B*, 77:161304, Apr 2008.
- [158] R. Koole, E. Groeneveld, D. Vanmaekelbergh, A. Meijerink, and C. de Mello Donega. *Nanoparticles*, chapter 2, page 13. Springer, Berlin, Heidelberg, 2014.
- [159] Haibo Zeng, Xi-Wen Du, Subhash C. Singh, Sergei A. Kulinich, Shikuan Yang, Jianping He, and Weiping Cai. Nanomaterials via laser ablation/irradiation in liquid: A review. *Adv. Funct. Mater.*, 22:1333, 2012.
- [160] Fangqiong Tang, Linlin Li, and Dong Chen. Mesoporous silica nanoparticles: Synthesis, biocompatibility and drug delivery. *Advanced Materials*, 24(12):1504, 2012.
- [161] A. S. Holmes. Laser fabrication and assembly processes for MEMS. In *Proc. SPIE*, volume 4274, pages 297–306, 2001.
- [162] E. Lioudakis, A. Othonos, G. C. Hadjisavvas, P. C. Kelires, and A. G. Nasiopoulou. Quantum confinement and interface structure of Si nanocrystals of sizes 3–5nm embedded in a-SiO₂. *Physica E: Low-dimensional Systems and Nanostructures*, 38(1):128–134, 2007.
- [163] S. Takeoka, M. Fujii, and S. Hayashi. Size-dependent photoluminescence from surface-oxidized Si nanocrystals in a weak confinement regime. *Physical Review B*, 62(24):16820, 2000.

- [164] L. Khriachtchev, S. Novikov, and J. Lahtinen. Thermal annealing of Si/SiO₂ materials: Modification of structural and photoluminescence emission properties. *Journal of Applied Physics*, 92(10):5856–5862, 2002.
- [165] G. Cliff and G. Lorimer. The quantitative analysis of thin specimens. *Journal of Microscopy*, 103(2):203–207, 1975.
- [166] J. Wong, D. A. Jefferson, T. G. Sparrow, J. M. Thomas, R. H. Milne, A. Howie, and E. F. Koch. High resolution electron microscopic and spectroscopic characterization of semi-insulating polycrystalline silicon and its interface with single-crystal silicon. *Applied Physics Letters*, 48(1):65–67, 1986.
- [167] M. Catalano, M. J. Kim, R. W. Carpenter, D. K. Chowdhury, and J. Wong. The composition and structure of SIPOS: a high spatial resolution electron microscopy study. *Journal of materials research*, 8(11):2893–2901, 1993.

Curriculum Vitae

Personal data

Name Nan Wang
Date of birth 08.01.1988
Place of birth Tianjin, China
Nationality Chinese
Email wangnan210@mails.ucas.ac.cn

Education

Since 10.2013 PhD candidate,
4th Institute of Physics,
Georg-August-University of Göttingen, Germany
China Scholarship Council scholar

09.2010 - 07.2013 Master of Philosophy
College of Materials Science and Opto-Electronic Technology,
University of Chinese Academy of Sciences, Beijing, China
With the thesis "Investigation of the methods for crystalline silicon
surface passivation and the related passivation mechanism"

09.2006 - 07.2010 Bachelor of Science
School of Science,
Northwestern Polytechnical University, Xian, China
With the thesis "The electric-magnetic transport of doped
manganese oxides films with a perovskite structure and heterojunctions"

School

09.2003 - 07.2006 No. 2 Middle school of Tianjin, Tianjin, China

Own publications

1. Fricke-Begemann T, Wang N, Peretzki P, et al. Generation of silicon nanocrystals by damage free continuous wave laser annealing of substrate-bound SiO_x films. *Journal of Applied Physics*, 2015, 118(12): 124308.
2. Stolzenburg H, Peretzki P, Wang N, et al. Implantation of plasmonic nanoparticles in SiO_2 by pulsed laser irradiation of gold films on SiO_x -coated fused silica and subsequent thermal annealing. *Applied Surface Science*, 2016, 374: 138-142.
3. Wang N, Fricke-Begemann T, Peretzki P, et al. Microstructural analysis of the modifications in substrate-bound silicon-rich silicon oxide induced by continuous wave laser irradiation. *Journal of Alloys and Compounds*, 2017, 707: 227-232.
4. N. Wang, T. Fricke-Begemann, P. Peretzki, J. Ihlemann, M. Seibt, Formation of porous silicon oxide from substrate-bound silicon rich silicon oxide layers by continuous-wave laser irradiation. *Journal of Applied Physics*, under review.
5. N. Wang, T. Meyer, T. Fricke-Begemann, P. Peretzki, J. Ihlemann, M. Seibt, The nanoscopic Si-SiO₂ phase separation in silicon rich silicon oxide by continuous wave laser annealing: a quantitative approach. In preparation.

Author Contributions

This thesis contains four articles:

1. Generation of silicon nanocrystals by damage free continuous wave laser annealing of substrate-bound SiO_x films, published in Journal of Applied Physics, 2015, 118(12): 124308 - Chapter 2
2. Microstructural analysis of the modifications in substrate-bound silicon-rich silicon oxide induced by continuous wave laser irradiation, published in Journal of Alloys and Compounds, 2017, 707: 227-232 - Chapter 3
3. Formation of porous silicon oxide from substrate-bound silicon rich silicon oxide layers by continuous-wave laser irradiation, under review in Journal of Applied Physics - Chapter 4
4. The nanoscopic Si-SiO₂ phase separation in silicon rich silicon oxide by continuous wave laser annealing: a quantitative approach, will be submitted to Applied Physics Letters - Chapter 5

The first two articles are published in the peer-reviewed journals Journal of Applied Physics (chapter 2) and Journal of Alloys and Compounds (chapter 3).

The third article in the chapter 4 has been submitted to the peer-reviewed journal Journal of Applied Physics. The Fourth article in the chapter 5 will also be submitted to Applied Physics Letters. All articles present original research by the author.

In all articles, the original samples induced by laser irradiation were provided by Dr. Thomas Fricke-Begemann and Dr. Jürgen Ihlemann from Laser Lab Göttingen. All TEM samples preparation were conducted by the author.

In article 1 (chapter 2), AFM, micro-Raman and micro-PL measurement were conducted by Dr. Thomas Fricke-Begemann. TEM sample characterization and analysis were conducted by the author under the guidance of Prof. Michael Seibt.

In article 2 (chapter 3), the major part of TEM investigation was conducted by the author under the guidance of Prof. Michael Seibt. Dr. Karsten Thiel from Fraunhofer Institute for Manufacturing Technology and Advanced Materials provides TEM tomography analysis of samples.

In article 3 (Chapter 4), TEM characterization and analysis was conducted by the author under the guidance of Prof. Michael Seibt. Patrick Peretzki assisted on EELS data collection and Arne Ahrens assisted on EELS analysis.

In article 4 (Chapter 5), TEM experimental data and analysis was conducted by the author under the guidance of Prof. Michael Seibt. The code for EDX simulation was written by Tobias Meyer.

I pronounce all co-authors listed in articles have contributions to the work.

Acknowledgements

I would first like to thank my thesis supervisor Prof. Michael Seibt in university of Göttingen. During the last four years, I have been a freshman in a new environment and Prof. Seibt is very patient to me. The door to his office is always open whenever I ran into a trouble spot or had a question about my research or writing.

I would like to thank my collaborators from Laser Lab Göttingen. They are Dr. Thomas Fricke-Begemann and Dr. Jürgen Ihlemann. They provide us nice original samples for TEM investigation. Our cooperation is very good and we discussed together about my thesis many times and they give a lot of meaningful feedback.

I am also grateful to Dr. Karsten Thiel from Fraunhofer Institute for Manufacturing Technology and Advanced Materials. He provides TEM tomography study of samples and give us some useful advice.

I would like to thank all my colleagues in research group of Prof. Seibt. In particular, Patrick Peretzki helps me to be familiar with almost all facilities related to my thesis; Arne Ahrens assists me to work on ETEM and gives me good advice in EELS analysis; Tobias Meyer makes EDX simulation to help me have better understanding on related data.

I would like to thank to my parents and my wife Yang Yue for supporting my life and study in Germany. The accompany of my wife in Göttingen makes my life rich and colorful during the last two years. And our baby Wilde is a nice gift for us and thanks to his birth. I would also like to thank all my friends for supporting and understanding.

I am also grateful for the support from CSC scholarship, the International Center for Advanced Studies of Energy Conversion, and the User Facility for Electron Microscopy (CLUE) at Georg-August-University Göttingen.

I would like to say goodbye to my student career during the past 23 years. I will enter a new stage of life and I hope everything is fine in future.

Nan Wang

Göttingen, November 20, 2017.